DISSERTATION

REEXAMINING THE DYNAMICS OF SHORT-SCALE, DIABATIC ROSSBY WAVES AND THEIR ROLE IN MIDLATITUDE MOIST CYCLOGENESIS

Submitted by
Richard W. Moore
Department of Atmospheric Science

In partial fulfillment of the requirements
for the Degree of Doctor of Philosophy
Colorado State University
Fort Collins, Colorado
Summer 2004

COLORADO STATE UNIVERSITY

May 17, 2004

WE HEREBY RECOMMEND THAT THE DISSERTATION PREPARED UNDER OUR SUPERVISION BY RICHARD W. MOORE ENTITLED REEXAMINING THE DYNAMICS OF SHORT-SCALE, DIABATIC ROSSBY VORTICIES AND THEIR ROLE IN MIDLATITUDE MOIST CYCLOGENESIS BE ACCEPTED AS FULFILLING IN PART REQUIREMENTS FOR THE DEGREE OF DOCTOR OF PHILOSOPHY

Committee on Graduate Work

Adviser

Department Head

ABSTRACT OF DISSERTATION

REEXAMINING THE DYNAMICS OF SHORT-SCALE, DIABATIC ROSSBY WAVES AND THEIR ROLE IN MIDLATITUDE MOIST CYCLOGENESIS

Raymond and Jiang (1990) and Synder and Lindzen (1991) independently introduced the notion of a diabatic Rossby wave [due to their anticipated vortical structure in three-dimensions, Moore and Montgomery (2004) referred to these features as a diabatic Rossby vortex (DRV); terminology that will be used hereafter]. For this type of disturbance growth, the diabatic generation of PV plays the role of the meridional advection of PV in the classical Rossby wave.

The goal of this work is to conduct an in-depth examination of the intrinsic characteristics of the DRV. To investigate the dynamics of these short-scale, diabatic disturbances we incorporate both a two-demensional (2D), semigeostrophic (SG) model and the PSU/NCAR mesoscale modeling system (MM5).

Results from the 2D, SG model clearly illustrate that both diabatic and baroclinic processes are integral to the DRV growth mechanism. In stark contrast to dry, long baroclinic waves, no upper boundary disturbance is necessary for DRV growth. Instead, it is the constant production of diabatically-generated PV (through the process of warm air advection, rising motion and latent heat release) that allows for amplification.

A number of idealized numerical simulations using MM5 confirm the basic results attained with the 2D, SG model: the three-dimensional structure of a DRV is found to be qualitatively very similar to that seen in the two-dimensional model simulations.

A subsequent sensitivity study illustrates that the intensity of a DRV is most sensitive to the magnitude of environmental baroclinicity and moisture content, while the vertical profile of moisture is the most dominant factor in determining the characteristic depth of the DRV. It is also found that the 'size' and 'strength' of a precursor perturbation vortex are important factors in determining the ultimate intensity and location of a DRV.

Due to the significant sensitivity to the initial condition, DRV formation and evolution pose a difficult challenge for the operational forecast community. This inherent problem is exacerbated by the remoteness of the preferred regions of DRV genesis: due to their reliance on environmental moisture, DRV's often form and grow over the ocean in regions where there is a distinct lack of observational data.

Richard W. Moore
Department of Atmospheric Science
Colorado State University
Fort Collins, Colorado 80523
Summer 2004

ACKNOWLEDGMENTS

This work was supported by in part by Funds for the Cooperative Institute for Research in the Atmosphere / NOAA grant # NA17RJ1228, the Research and Scholarly Programs fund at Colorado State University, and by National Science Foundation Grants ATM-0101781 and ATM-0132006.

Table of Contents

1. Introduction

1.1 Background

In his pioneering paper on baroclinic instability, Eady (1949) used the terminology of long waves and cyclone waves to differentiate between the characteristic scales of observed disturbances in the middle to high latitudes. It is clear from this work that he believed the latter to be, at least in part, related to moisture effects. To emulate disturbances of the scale typical of cyclone waves, Eady used the same set of equations as that for long waves, only with smaller values for the static stability and smaller vertical extents in an effort to mimic moisture effects (Eady 1949; Section # II). An underlying assumption of this approach is that the same basic physical processes are at work for both scales. The resulting disturbance structure is essentially identical, with the exception of a significantly reduced scale (both in the horizontal and vertical) for the case of cyclone waves.

As we will see, herein lies a common misconception. It is often thought that moisture effects merely serve to modify the structure and growth characteristics of the essentially dry dynamics. In many cases, this does appear to be the case: the most apparent effects of diabatic processes are often a reduction in horizontal scale and a further intensification of the system. However, this general statement is more typically true of the long wave regime.

As this work will show, there exists dynamical processes in a moist, baroclinic atmosphere that have no dry counterpart. It is therefore necessary to look beyond the

commonly-held assumption that diabatic processes simply act to modify dry disturbance growth.

1.1.1 Moist Baroclinic Instability Studies

In the early 1980's, measurements taken within the ascent regions of midlatitude cyclones revealed that the atmospheric temperature lapse rate along constant momentum surfaces is nearly moist adiabatic, likely in response to slantwise moist convection (Emanuel, 1985). This observation sparked the study of frontal circulations and surface frontogenesis in environments nearly neutral to slantwise moist convection (Emanuel, 1985; Thorpe and Emanuel, 1985). The main effect of this condition is to cause a scale contraction of the ascent region and enhanced surface frontogenesis.

In 1987, Emanuel et al. (hereafter EFT) utilized a two-level, two-dimensional semigeostrophic model to investigate the more basic issue of the effects of latent heat release on the development and structure of baroclinic waves, taking near-zero moist potential vorticity (PV) as the relevant constraint on the rate of release of latent heat. An analytical solution to the above system was derived in EFT. Their findings confirmed the earlier results of Emanuel (1985) and Thorpe and Emanuel (1985), namely that the moist development exhibits considerable scale contraction in the region of ascent and larger growth rates than observed in the dry system. In the limit of zero moist PV, they found that the growth rate of the fastest growing wave is about 2.5 times the dry value with a horizontal reduction in scale of approximately 0.6 compared to the dry modes.

To examine the semigeostrophic system with more than two vertical levels, it is necessary to use numerical analyses, as an analytic solution to the problem is not tractable. EFT ran a number of numerical simulations using a multi-level (~ 250 m vertical resolution) semigeostrophic model to determine the temporal development of PV. They found the deepening of the cyclone, as measured by surface pressure minimum, to

be much accelerated in the moist system (approximately 2.5 times that of the dry value); however, they did theorize that the inclusion of even modest amounts of surface dissipation would substantially reduce the deepening rate. They concluded that it is unlikely that condensation effects on normal mode growth can by themselves explain extreme cases of cyclogenesis, noting that condensation processes are not peculiar to oceanic storms.

Joly and Thorpe (1989; hereafter JT) examined the initial growth of small amplitude disturbances near the limit of neutral moist ascent in an attempt to ascertain the moist normal modes of the Eady problem. They used a multi-level semigeostrophic model, incorporating the EFT parameterization of latent heat release. Their results confirmed EFT's main findings: a shift towards smaller scales of the maximum growth rate and an increased growth rate of the most unstable wave. Specifically, they found that the increased vertical resolution used in their model resulted in a reduced maximum growth rate of 1.9 times that of the dry system.

The results of these and other studies clearly show that moist processes can significantly alter wave growth and structure. In general, the effect of moisture is to: i) increase the range of unstable wavelengths, ii) increase growth rates, and iii) shift the maximum growth rate towards smaller scales (EFT; JT).

The emphasis of these studies, however, was to determine the growth and evolution of the long baroclinic waves that result from the interaction of an upper and lower level boundary PV anomaly in a moist environment. Both EFT and JT assumed a constant vertical profile of latent heat release. If latent heat release is allowed to vary with height, either by the assumption of a variable static stability or moisture content in the vertical, a second class of unstable baroclinic modes is found to exist (Fantini and Buzzi 1993, 1994 and 1997; Fantini 1995; Mak 1994 and 1998; Montgomery and Farrell 1991 and 1992; Whitaker and Davis 1994).

When the vertical profile of latent heat release is consistent with thermodynamic considerations, the shortwave cutoff present in the moist, inviscid system vanishes and a constant growth rate is predicted for zonal wavelengths shorter than a specific value [(Montgomery and Farrell 1991; hereafter MF91); Whitaker and Davis 1994]. For zonal wavelengths shorter than this value, a wholly different growth mechanism is at work. The resulting disturbance, termed a diabatic Rossby wave by Parker and Thorpe (1995), grows as a result of both diabatic and baroclinic effects.

1.1.2 The Diabatic Rossby Vortex

The notion of a diabatic Rossby wave was introduced independently by Raymond and Jiang (1990) and Snyder and Lindzen (1991). For these waves, the diabatic generation of PV plays the role of the meridional advection of PV in the classical Rossby wave.

The growth mechanism, as described by Parker and Thorpe (1995; see Figure 1.1; their Fig. 6), is as follows: warm thermal advection to the east of a low-level positive PV anomaly results in forced ascent and the generation of positive low-level PV due to diabatic heating. In a balanced or quasi-balanced system, a positive PV anomaly is associated with a cyclonic relative circulation. Therefore, warm thermal advection occurs farther to the east, continuing the process and resulting in wave propagation in the direction of the thermal wind.

The use of the 'Rossby wave' terminology is appropriate in that the dynamics of both a classical Rossby wave and a diabatic Rossby wave can be shown to result in a PV tendency (see Fig. 1.1c). In the former it is the process of the meridional advection of the background PV that is responsible. In contrast, it is the diabatic production of PV in a moist, baroclinic environment for a diabatic Rossby wave. Parker and Thorpe illustrated

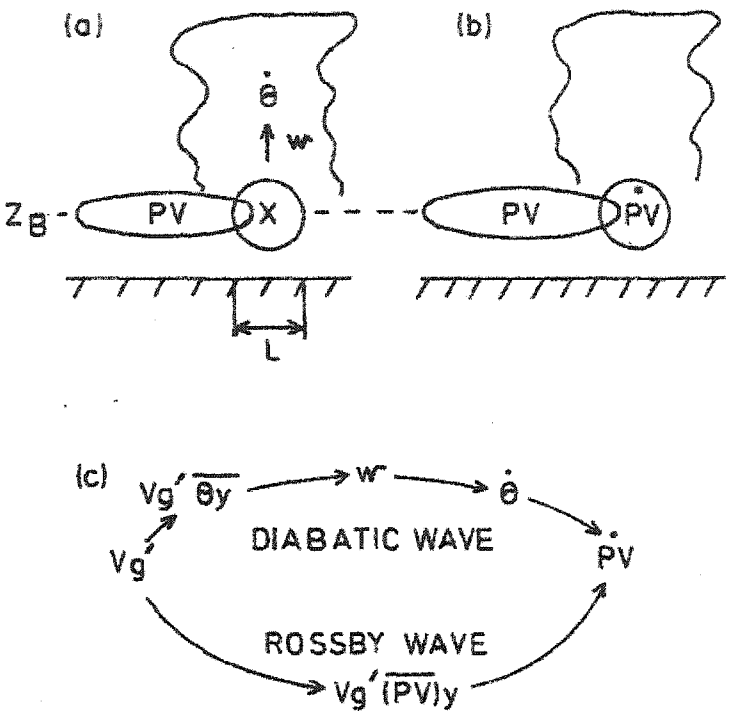

FIG. 6. Schematic representations of the dynamics of the diabatic Rossby wave. Here L is the horizontal scale of the jet on the eastern side of the pv anomaly. (a) The poleward jet (marked ×) associated with the low-level pv anomaly gives positive thermal advection, leading to upward motion and diabatic heating. (b) This diabatic heating leads to a pv tendency to the east of the low-level pv anomaly. (c) A comparison between the dynamical processes involved in the diabatic wave and the classical Rossby wave, linking meridional advection with the pv tendency.

Figure 1.1 – Figure 6 from Parker and Thorpe (1995).

that one can diagnose an equivalent 'diabatic PV gradient' for a diabatic Rossby wave (equivalent to that of the meridional PV gradient of a classical Rossby wave). Since the diabatic equivalent to the meridional PV gradient is of opposite sign to that for a classical Rossby wave, diabatic Rossby waves propagate in an eastward direction (in contrast to a westward direction for classical Rossby waves).

The practical importance of this growth mechanism is highlighted by the variety of atmospheric phenomenon they have been related to. Previous studies have connected

DRW dynamics to explosive cyclones (Gyakum et al. 1992; Wernli et al. 2002), mesoscale convective systems (Raymond and Jiang 1990), squall lines (Parker and Thorpe 1995), and polar lows (Montgomery and Farrell 1992; Fantini and Buzzi 1993; Mak 1994).

In a realistic three-dimensional framework, these features appear as coherent vortices [see Raymond and Jiang 1990 (their Figure 6) and Montgomery and Farrell 1992 (their Figure 2)]. They are characterized by a closed circulation and the absence of the alternating high / low structure that is associated with wave-like disturbances. For this reason, we suggest that a more appropriate term for these disturbances is a diabatic Rossby vortex (DRV; we will hereafter use this designation).

1.2 Observational Motivation

Beyond the detailed analysis of the role a DRV played in the case of extreme, winter storm 'Lothar' (Wernli et al. 2002), there is a distinct lack of observational work on the DRV. One need not look far, however, for anecdotal evidence of the importance of the DRV growth mechanism in the atmosphere. Two intriguing cases are the east coast snow storm of February 6-7, 2003 and the extratropical transition of Hurricane Gabrielle in September 2001. These cases are summarized here.

1.2.1 East Coast Snow Storm: February 6-7, 2003

A significant snow event occurred on the east coast of the United States (US) on February 6-7, 2003. The observed snow cover before and after this event are presented in Fig. 1.2. Measurable precipitation was observed throughout the central east coast states, with a

local maximum of approximately 7 inches of snow recorded in the Washington DC/ Baltimore area.

1.2a) 1.2b)

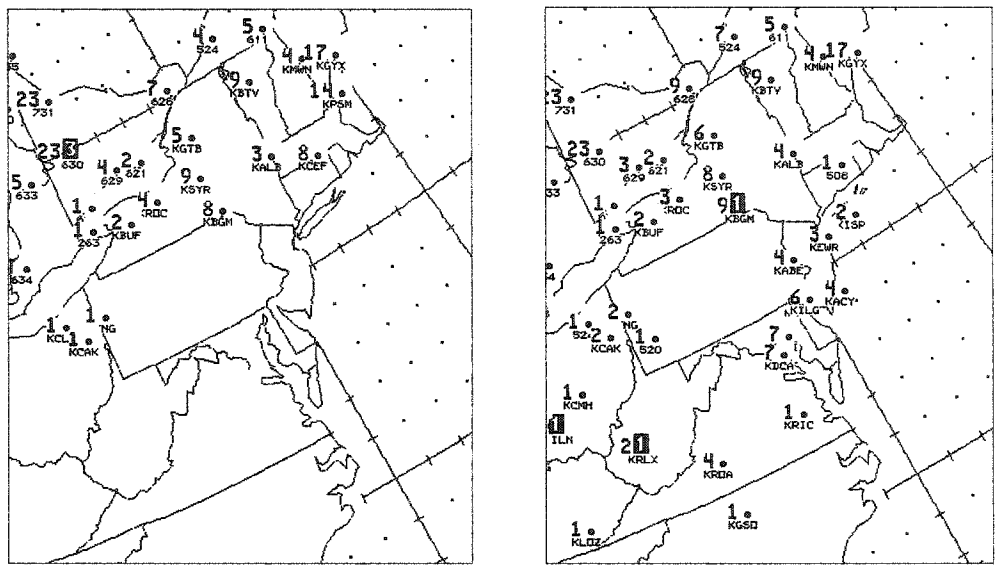

Figure 1.2 – Observed snow cover (inches): a) 12Z, February 6th; and b) 12Z February 8th.

The precipitation that fell from early evening on February 6th until mid-morning on the 7th occurred as a low pressure center translated up the eastern coast of the US. While the surface disturbance subsequently interacted with an upper level trough (and deepened significantly off the eastern coast of the US), the low-level cyclonic circulation was observed to be a relatively shallow feature at the time of maximum precipitation in the Washington DC area. Given the ample baroclinicity and moisture of the environment in which the disturbance was embedded, it is possible that the DRV growth mechanism was, at least in part, responsible for the observed deepening of the surface low and the significant precipitation that occurred.

The synoptic setup at 0Z February 7th is presented in Fig. 1.3 (for reference, this is approximately 30 minutes before snow began to fall on Washington DC). A southwest to northeast oriented baroclinic zone is present along the east coast of the US (Fig. 1.3a). A quick calculation indicates an average surface temperature gradient of approximately 2 K per degree latitude. This can be compared to the equivalent temperature gradient for the Eady basic state (shear of 3.0 ms^{-1} / km) of about 1.2 K per latitude. Associated with this low-level baroclinic zone is an upper-level, wind maximum (Fig. 1.3d). As expected from a simple thermal wind argument, the observed wind speeds at this level (about 65 ms^{-1}) are approximately double that of the Eady jet. Most importantly for this discussion, the upper-level jet is observed to be a relatively straight-line feature, indicating a lack of a significant upper-level cyclonic anomaly at this time.

In addition to environmental baroclinicity, the low-level environment is moist. The relative humidity at 850 mb (Fig. 1.3b) is greater that 70% throughout most of the region of interest. While an isolated surface pressure minimum is not indicated (likely as a result of the course horizontal resolution of these maps), one can ascertain from the surface pressure field that warm, moist advection is occurring throughout most of the southeastern US. A concurrent radar summary (Fig. 1.4a) lends credence to this logic, as a radar echo is observed over a wide area.

By 12Z on February 7th, an isolated surface pressure center measuring approximately 1005 mb is observed at approximately 36N, 75W (Fig. 1.5a). The low-level baroclinic zone has intensified over the previous 12 hours and is more closely paralleling the east coast of the US. By this time, the vast majority of the total-storm precipitation has fallen on the Washington DC area. While meterological data is somewhat difficult to come by for this period, we can venture an educated guess as to what transpired between 0Z and 12Z February 7th. It is likely that a surface pressure

1.3a)

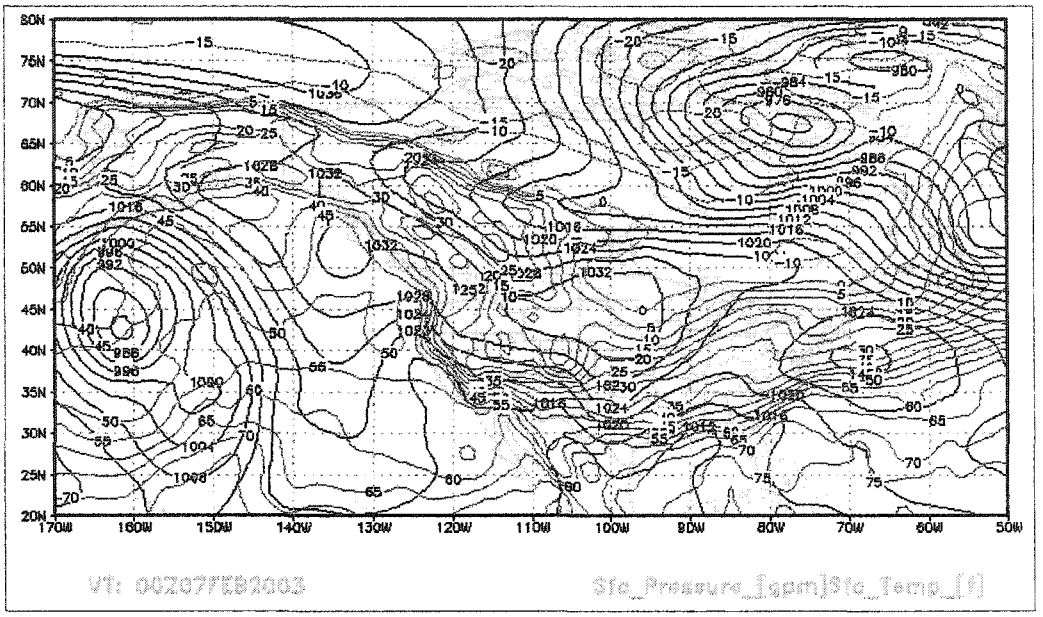

1.3b)

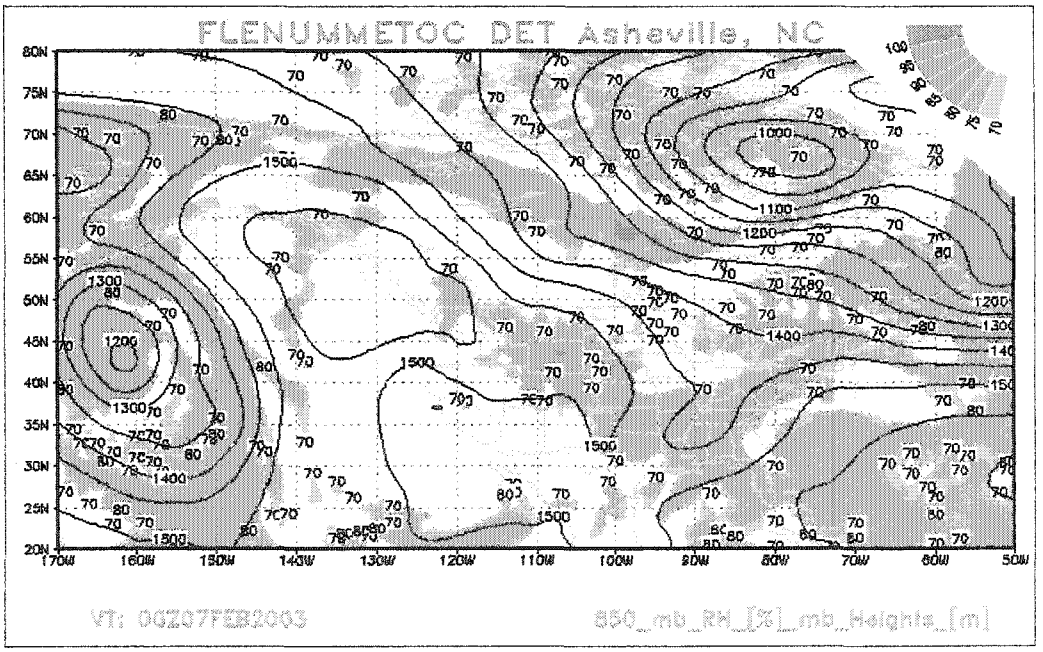

1.3c)

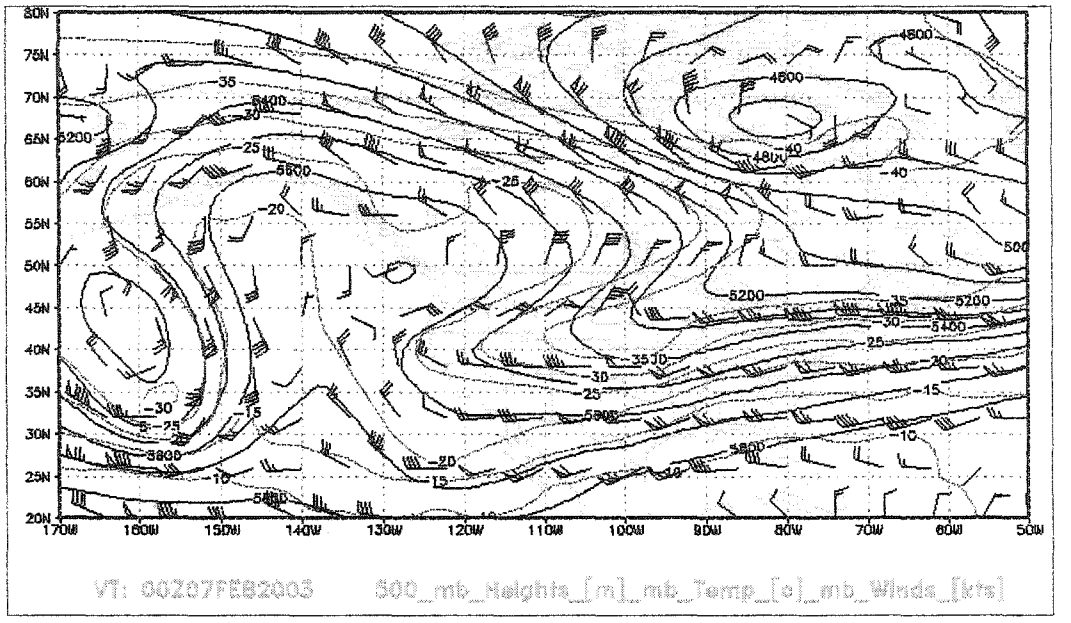

1.3d)

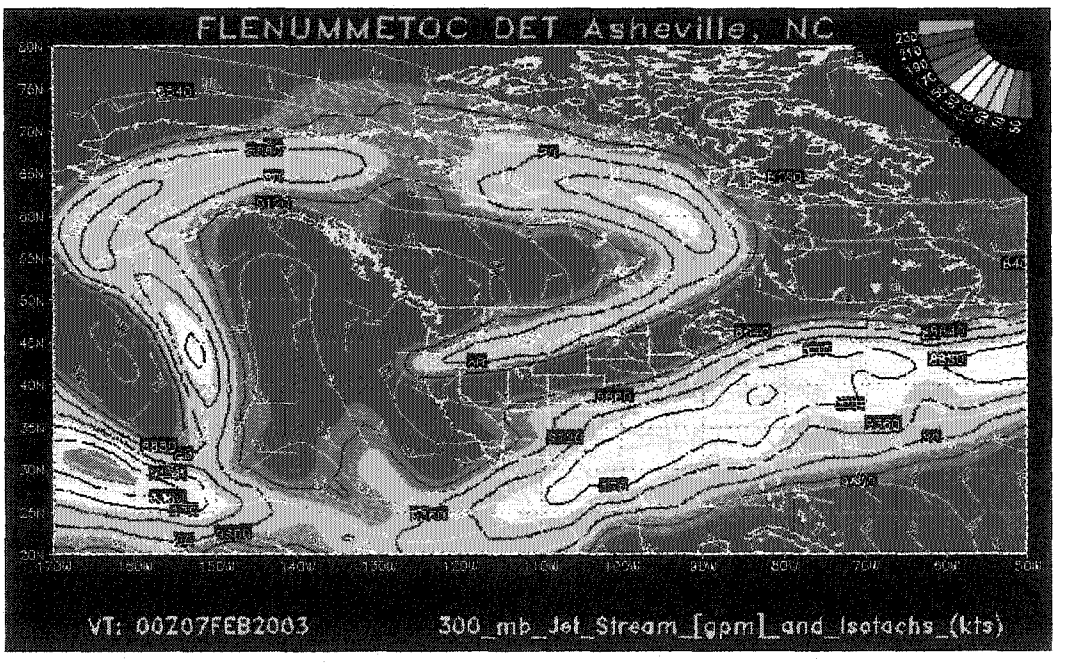

Figure 1.3 – Synoptic setup at 0Z February 7th, 2003: a) surface temperature (solid color; degrees Fahrenheit) and pressure (solid black; mb); b) 850 mb relative humidity (green shading; %) and heights (solid black; m); c) 500 mb temperature (dashed purple; degrees Celsius), heights (solid black; m) and wind barbs (kts); and d) 300 mb wind speed (color shading; kts), wind barbs (kts) and heights (white solid; m).

minimum and its associated cyclonic rotation formed soon after 0Z (in the vicinity of the Georgia / South Carolina border) and subsequently began to intensity. The disturbance then translated to the north/northeast, bringing with it enhanced warm moist advection in the north/northeast quadrant of the storm.

Again, an examination of radar summary plots appears to lend credence to this argument (Fig. 1.4). From approximately 4Z onward, two distinct regions of enhanced echo intensity (and presumably precipitation) consistently appear: 1) to the north/northeast of the estimated position of the surface low and 2) a nearly stationary linear region over the Florida peninsula, most likely associated with a cold front type feature. While there is little doubt that some large scale lifting associated with jet streak dynamics is occurring (Fig. 1.5d), aiding precipitation processes, it is likely that the former region of precipitation is at least in part due to DRV dynamics; specifically, warm, moist advection due to the southeasterly flow in the north / northeast quadrant of the low-level disturbance and forced rising motion in response to the environmental baroclinicity.

1.4a)

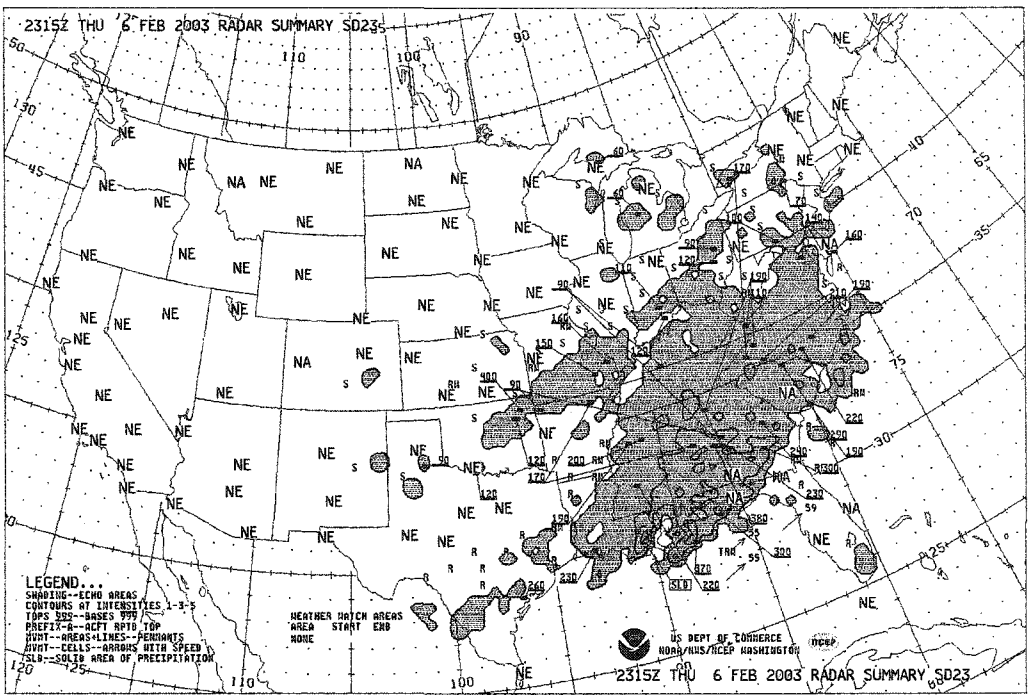

1.4b)

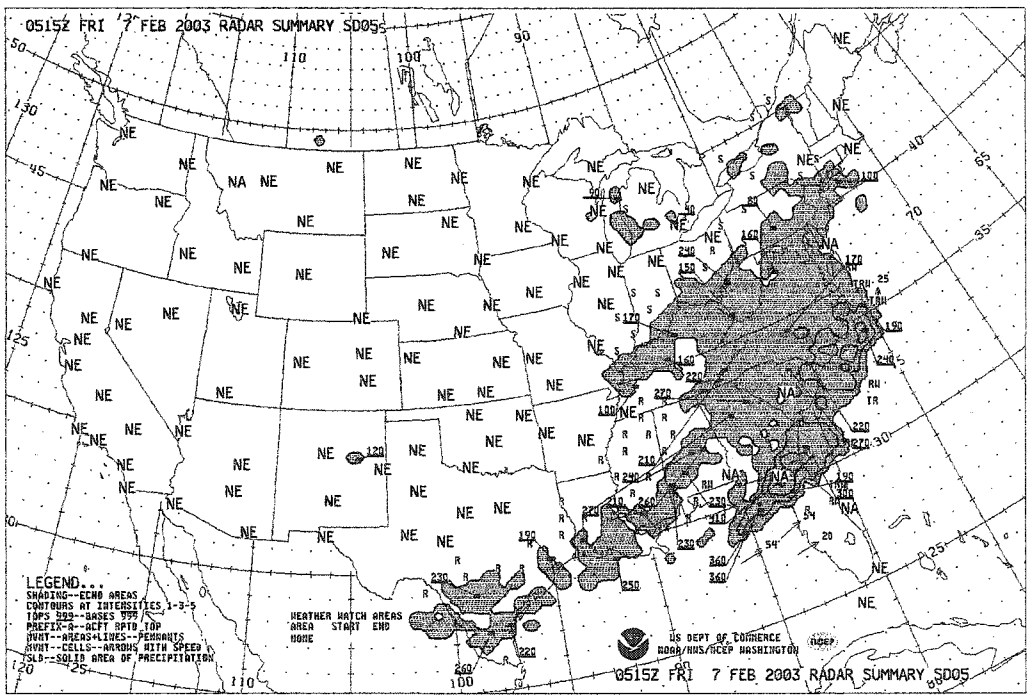

1.4c)

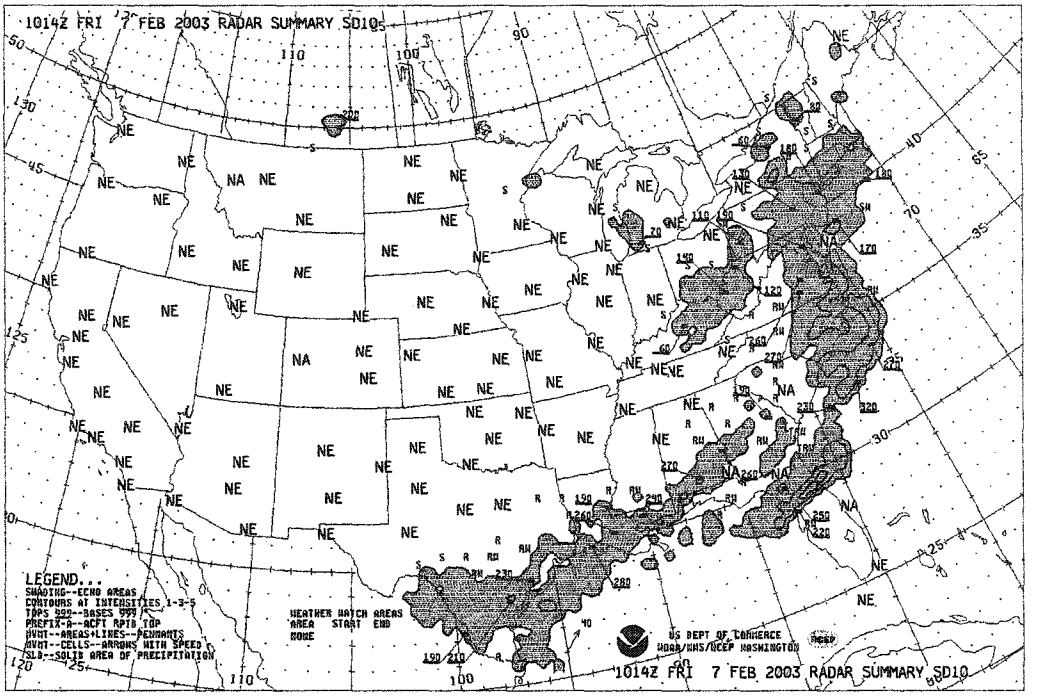

Figure 1.4 – Radar summary at: a) 2315Z, February 6th; and b) 0515Z February 7th; and c) 1015Z, February 7th. Radar echo areas (shading), contours of reflectivity intensity (10, 30, and 50 dbZ) and echo tops.

1.5a)

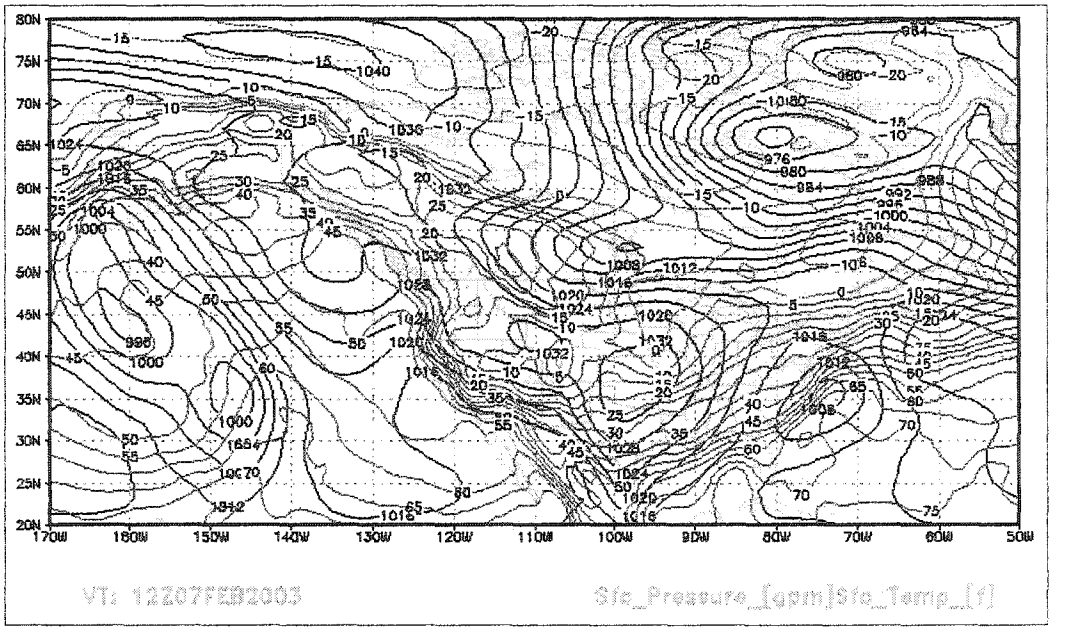

1.5b)

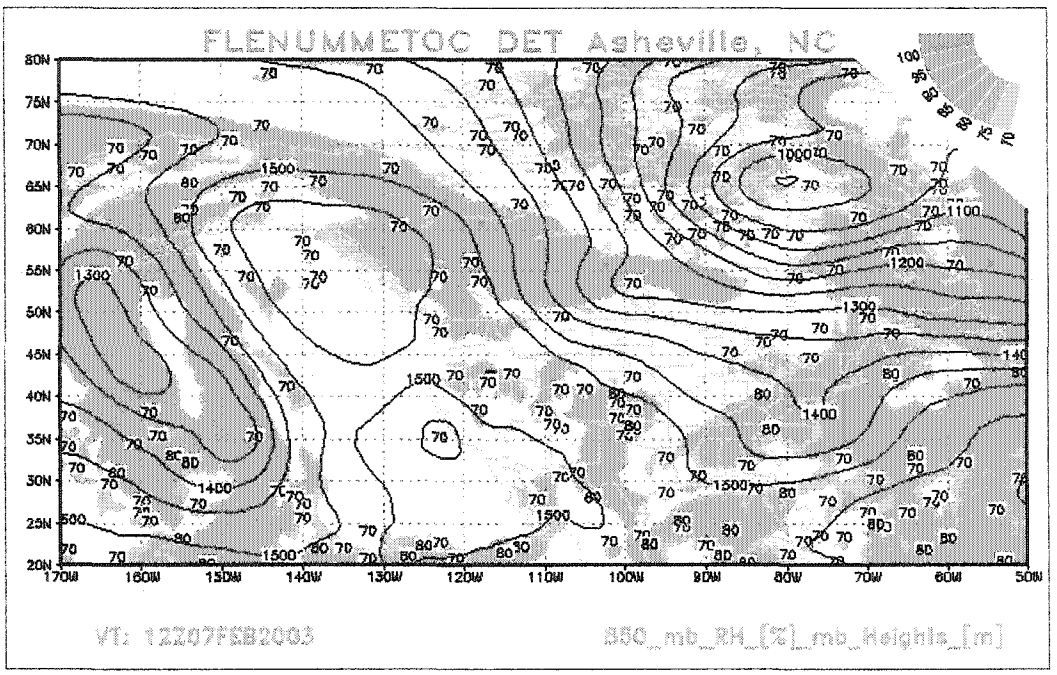

1.5c)

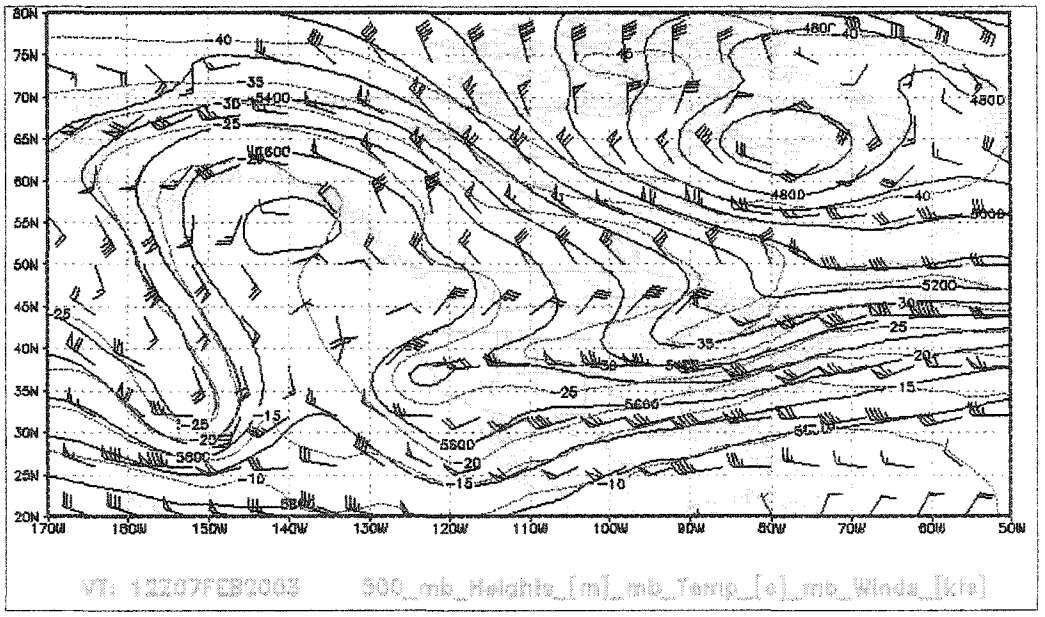

1.5d)

Figure 1.5 – Same as Fig. 1.3 except for 12Z February 7th.

As a final step, it is important to ascertain if the low-level disturbance observed at 12Z February 7th is interacting with the approaching upper-level trough that can be seen at 500 mb (Fig. 1.5c). This can be accomplished through a calculation of the Rossby radius of deformation of the local environment and a direct comparison with the physical distance between the two features. A back-of-the-envelope calculation for the Rossby radius gives a value of approximately 1300 km, while the physical distance between the lower- and upper-level features is about 1450 km at this time.

This somewhat subjective analysis suggests the upper-level trough was not providing a strong influence on the low-level disturbance throughout the period of most intense precipitation. This conclusion is further corroborated by the significant deepening of the surface low observed after this time (approximate 16 mb over the next 12 hours; Fig. 1.6). This explosive growth was almost assuredly the result of an approximate phase-locking of the upper- and lower-level disturbances. The timing of the

explosive growth implies that such a phase-locking was not occurring during the time of maximum precipitation, indicating that another mechanism for disturbance amplification was at work at this time. Given these facts, it is concluded that the DRV growth mechanism, in conjunction with jet streak dynamics, likely played an integral role in this case.

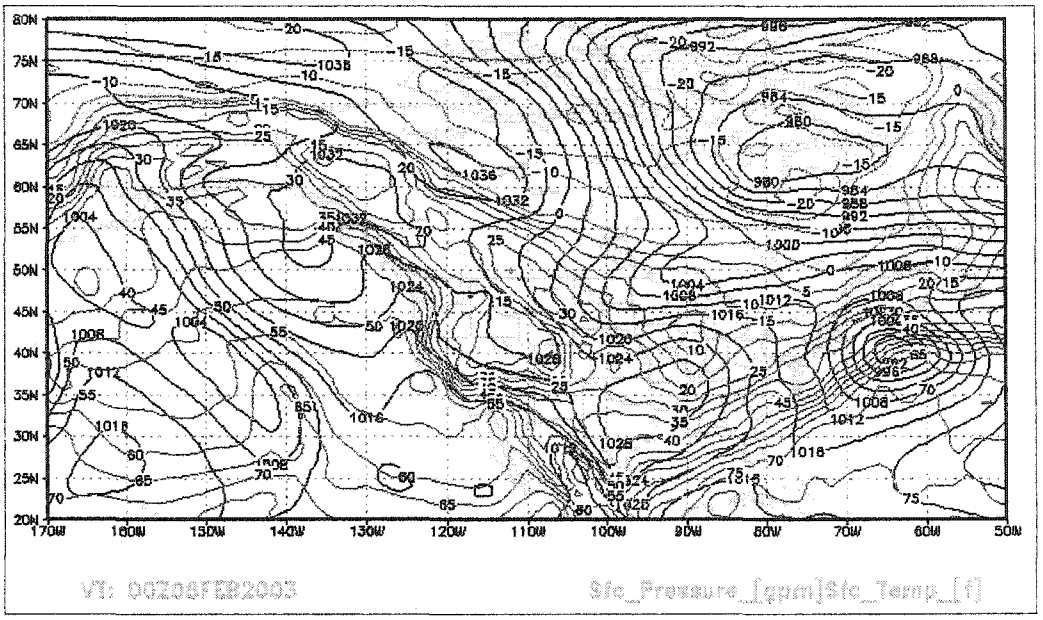

Figure 1.6 – Same as Fig. 1.3a except for 0Z February 8th

1.2.2 Hurricane Gabrielle: September 18-19, 2001

At its maximum intensity, Hurricane Gabrielle exhibited a 70 kt maximum wind speed, placing it as a category 1 disturbance on the Saffiir-Simpson scale of hurricane intensity. While not an intense hurricane, Gabrielle did account for approximately 230 million dollars of property damage and the death of a fifteen-year-old boy in Florida.

The aspect of this storm that relates to the present study is the subsequent re-intensification of Gabrielle. Associated with this re-intensification was a significant precipitation event over the Avalon Peninsula of Newfoundland. Six inches of rain was

recorded over a 12-hour or less period; during a single 1-hour period, 1.9 inches of rain was measured at Cape Race, Newfoundland.

The best track position, maximum sustained surface wind and minimum central pressure plots for Gabrielle are presented in Fig 1.7. Gabrielle achieved its maximum intensity (as measured by the strongest maximum sustained surface wind) at 12Z on September 17th, 2001. Over the subsequent 18 hours, Gabrielle was observed to weaken: by 6Z on the 18th, the maximum sustained surface wind and minimum central pressure were 55 kts and 990 mb, respectively.

It was at this time that the weakening of the system ceased and, subsequently, Gabrielle re-intensified. Over the next 24 hours, the surface pressure dropped 15 mb, including a 10 mb drop over the 6-hour period between 12Z and 18Z on the 18th. The timing of the re-intensification of Gabrielle is coincident with the translation of the disturbance into a low-level baroclinic zone, suggesting that the DRV growth mechanism may have been responsible.

1.7a)

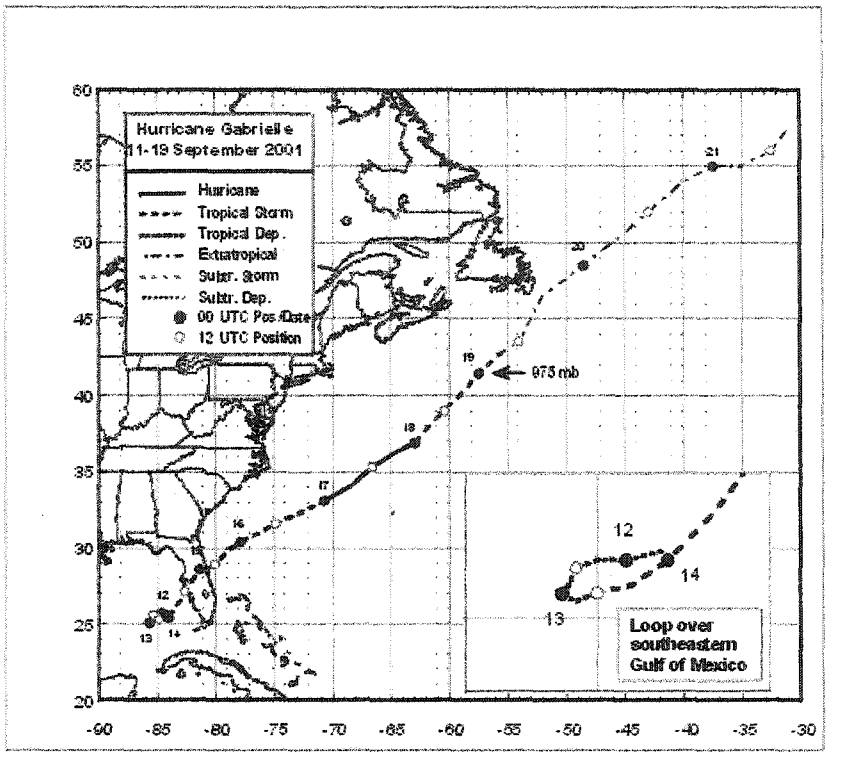

1.7b)

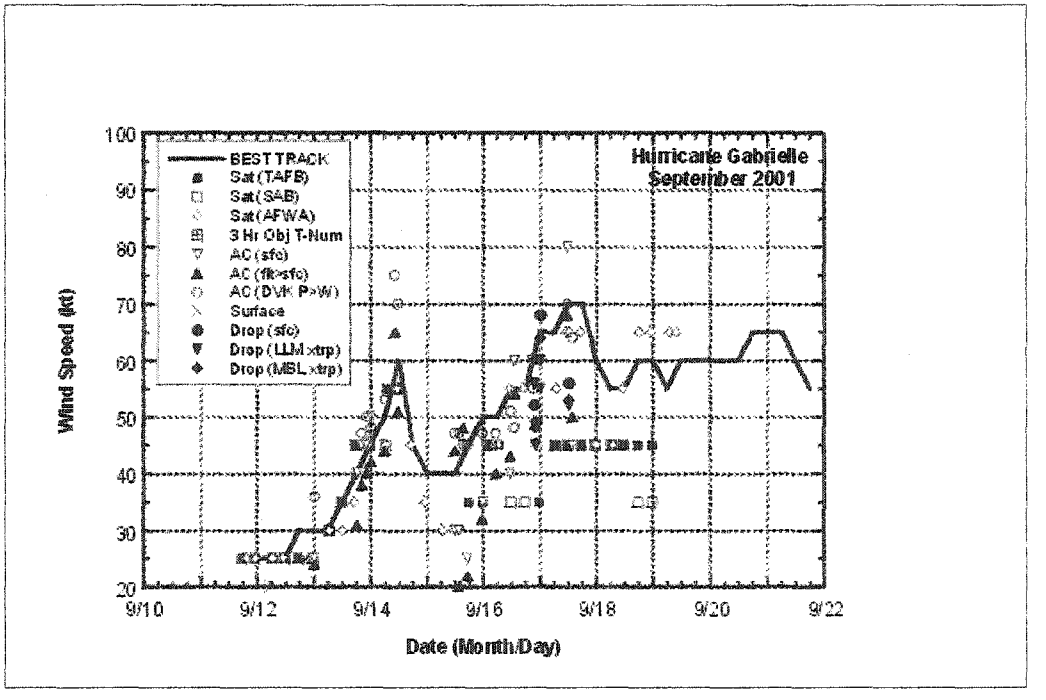

1.7c)

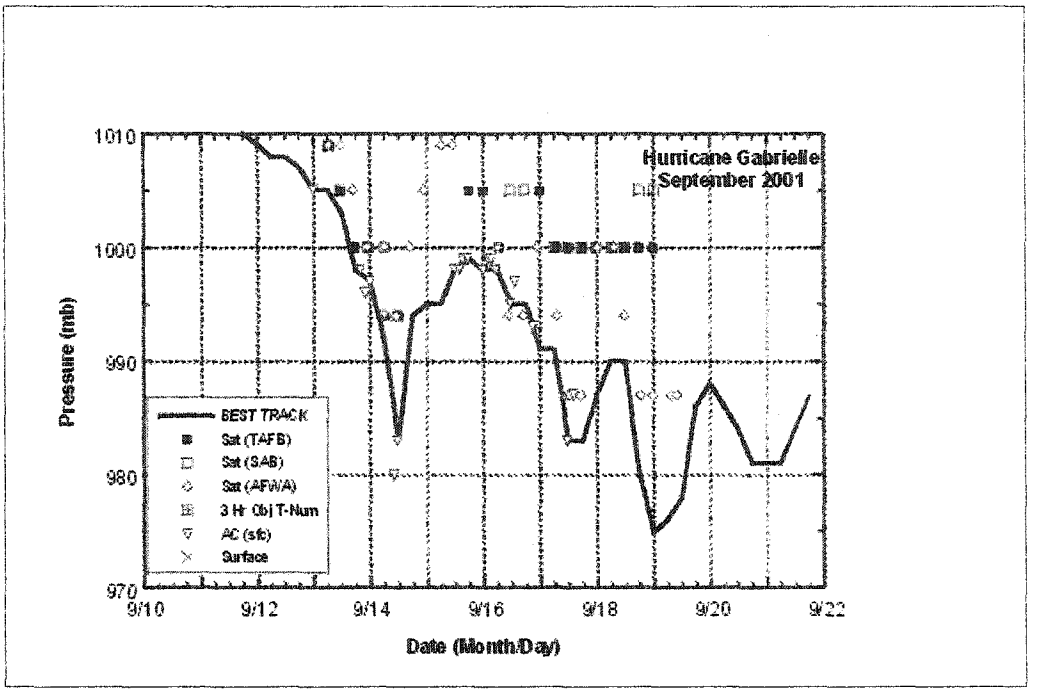

Figure 1.7 – National Hurricane Center best track estimates of: a) storm location; b) maximum sustained surface wind; and c) minimum central pressure.

The synoptic setup at 12Z on September 18th is presented in Fig. 1.8. The two necessary ingredients for the DRV growth mechanism to operate are sufficient environmental baroclinicity and moisture. It is clear from the surface and 850 mb maps, respectively, that both ingredients are present in the local environment of Gabrielle. Furthermore, there is a distinct lack of an upper-level trough that might, through the process of phase-locking and mutual amplification, account for the re-intensification of Gabrielle. Given these facts, it seems likely the re-intensification of Gabrielle that is observed at this time is due to the DRV growth mechanism.

Corroborative evidence for this viewpoint comes directly from the National Hurricane Center analysis of Gabrielle (http://www.nhc.noaa.gov/2001gabrielle.html).

1.8a)

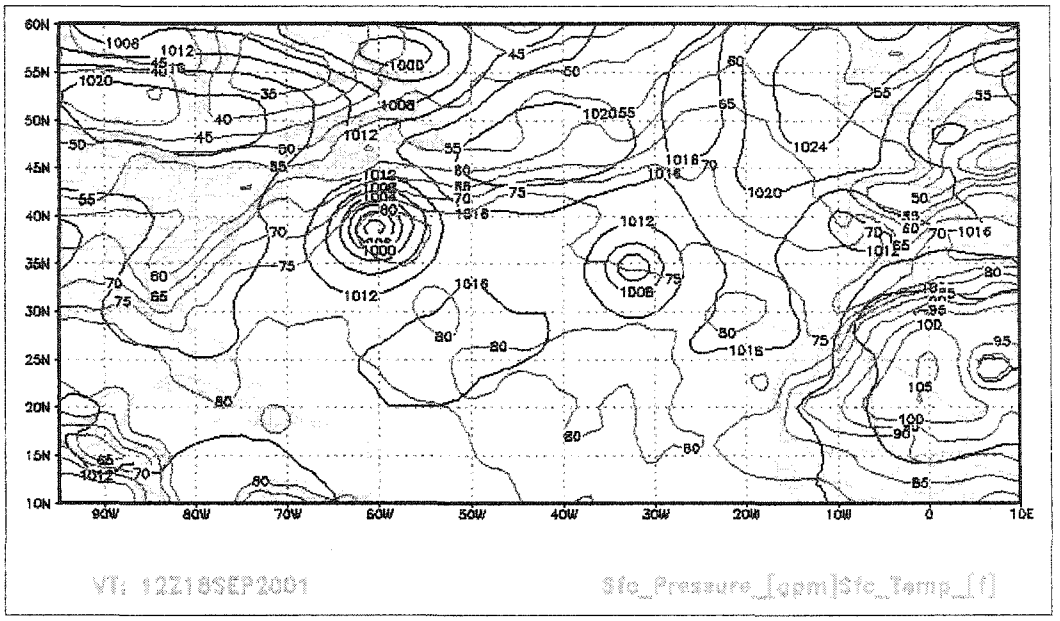

1.8b)

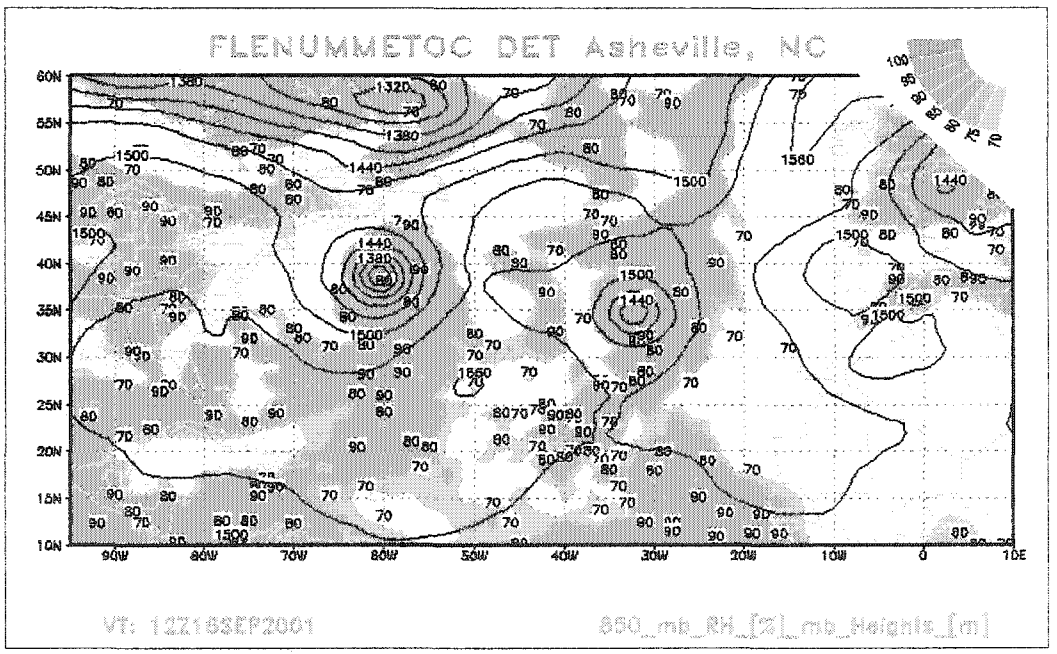

1.8c)

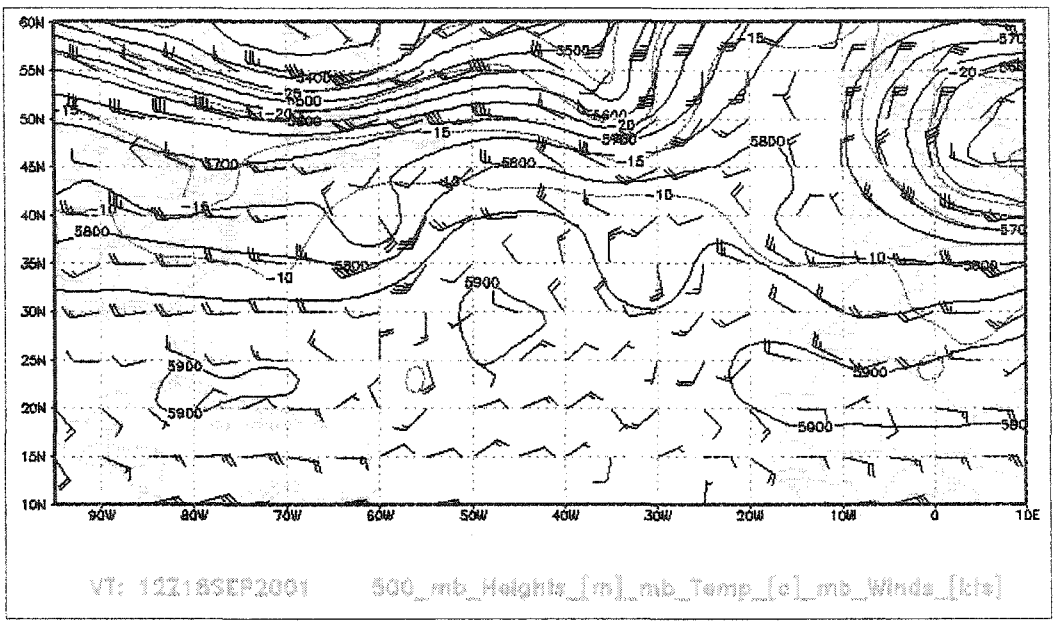

1.8d)

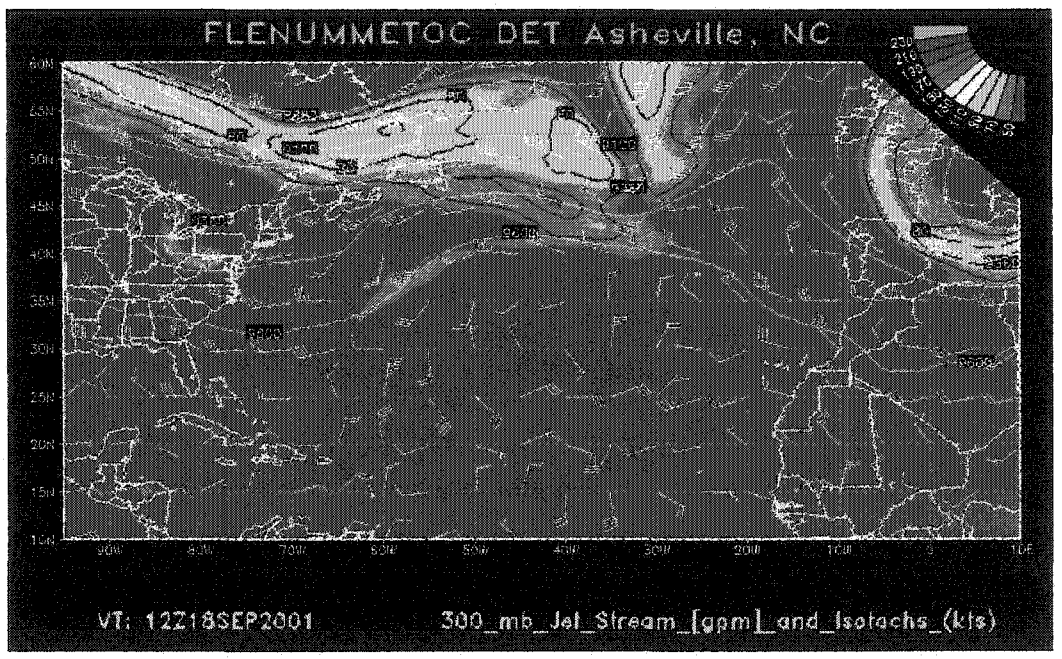

Figure 1.8 – Same as Fig. 1.3 except for 12Z September 18th, 2001.

After 6Z on the 19th, Gabrielle again began to weaken. It is precisely at this time that the tropical cyclone report states that Gabrielle 'lost all deep convection near the center'.

The previously-described evolution of Gabrielle suggests that the DRV growth mechanism was responsible for the re-intensification of the system. The process did not begin, even though deep convection was observed, until the Gabrielle encountered a low-level baroclinic zone. Furthermore, the re-intensification phase ended precisely at the time that deep convection ceased. The implication is that both diabatic and baroclinic effects were integral to this process. Given that there is a distinct lack of any upper-level disturbance with which Gabrielle could interact, we are left with the conclusion that it was likely the DRV growth mechanism that was responsible for Gabrielle's re-intensification.

1.3 Statement of Problem and Dissertation Outline

The fact that the DRV growth mechanism has been related to a myriad of atmospheric processes highlights the need for an understanding of this type of disturbance. However, there remains a paucity of research investigating the characteristics of DRVs themselves. It is this issue that we hope to address with this work.

As a first step, it is important to clearly differentiate between the dynamics of DRVs and long baroclinic waves. We will ask such questions as: what mechanisms are responsible for disturbance growth? How do their respective disturbance structure and evolution differ? How does the disturbance extract energy from the environment? What factors determine which type of disturbance is favored?

Consistent with past research, we will begin with the use a simplified, dynamical model to ascertain the growing modes of a moist, baroclinic atmosphere. The choice of a simplified, balanced model framework, as opposed to one incorporating the

full, primitive equations of motion, is consciously made: by minimizing the complexity of the system, we believe it easier to identify the important physical processes at work.

Once a clear distinction between long baroclinic waves and DRVs has been made, the remainder of the dissertation will concentrate on a comprehensive examination of DRV characteristics. Again, simplified model results will be used to elucidate this point. In addition to a complete description of DRV structure, evolution and energetics, we will address such important issues as the effect of frictional dissipation and growth at finite amplitude.

After building a foundation with the simplified model results, we will progress to a more complete model setting. The PSU/NCAR mesoscale model (MM5) is used to conduct a number of idealized numerical simulations of DRV formation, growth and evolution. This portion of the dissertation has two primary goals: i) ascertain the characteristics of a DRV in the 'true' atmosphere and compare / contrast with the simplified model results; and ii) better understand the dependence of the DRV dynamics on some of the more pertinent environmental and perturbation vortex parameters.

Finally, we will summarize the study results and briefly discuss not only the importance of DRVs in the true atmosphere but also the difficulty they pose to the operational forecast community.

An outline of the dissertation is as follows. A description of the atmospheric models used in this study is presented in Section 2. The results from the simplified, dynamical model are described in Section 3. In Section 4, the characteristics of a DRV in a full-physics, mesoscale model are presented. Finally, in Section 5, a summary of the study findings and a discussion of the practical importance of DRVs are given.

2. Atmospheric Models

2.1 The Two-Dimensional, Semi-Geostrophic Model

The model used in this study is the two-dimensional (2D), semigeostrophic Boussinesq Eady model (Hoskins and Bretherton, 1972). The choice of a simplified, balanced model framework, as opposed to one incorporating the full, primitive equations of motion, is consciously made in keeping with the motivations of this work. By minimizing the complexity of the system, we believe it easier to identify the important physical processes at work.

The clear caveat being that not all processes are captured in this particular model framework. In the real world, extratropical cyclones are three-dimensional (3D) and not necessarily constrained by balanced dynamics. However, while there is no distinction between cyclones and fronts in a 2D model framework, previous results have shown 2D systems can do an admirable job of simulating observed cyclone intensity and structure (EFT; JT; Montgomery and Farrell 1991; Parker and Thorpe 1995). Furthermore, it has been shown that even in rapidly intensifying cyclones the balanced equations are able to capture much of the nondivergent wind, irrotational wind and height tendency fields (Davis et al., 1996). In this spirit, we will be using the 2D model as a metaphor for the 3D problem. Future work is planned to examine moist cyclogenesis in a full-physics, cloud-resolving model.

2.1.1 Model Summary

(i) *The Inviscid System*

The two-dimensional semigeostrophic Boussinesq Eady model (Hoskins and Bretherton, 1972) is a useful system for the study of moist frontal dynamics due to its ability to capture the rapidity of frontogenetic processes by retaining advection of the ageostrophic winds producing strong convergence and infinite relative vorticity in finite time (MF91). In terms of the modified geopotential ($\Phi = \varphi + v_g^2/2$), the model takes a simple form when it is formulated in geostrophic coordinates:

$$X = x + \frac{v_g}{f} \tag{2.1a}$$

$$Z = z \tag{2.1b}$$

$$T = t \tag{2.1c}$$

The formulation of the model used in this study is described in detail in (MF91). A brief outline is given here.

The two dimensional Eady model consists of a two dimensional wave field superimposed upon a hydrostatic basic state with a zonally homogeneous constant shear in the thermal wind balance with a constant meridional temperature gradient. The basic state is:

$$\overline{U}_g = SZ;\ \overline{V}_g = 0;\ \overline{U}_{ag} = 0;\ \overline{V}_{ag} = 0;\ \overline{W} = 0 \tag{2.2a}$$

$$\overline{\Phi}(Y,Z) = -fSYZ + \left(\frac{N_0^2 Z^2}{2}\right) + gZ \tag{2.2b}$$

$$\overline{\Theta}(Y,Z) = -g^{-1}\theta_0 fSY + g^{-1}N_0^2\theta_0 Z + \theta_0 \tag{2.2c}$$

The basic state is disturbed with the amplitude of the disturbance not being assumed small. In accord with the two dimensionality constraint on the disturbance field, X-periodic solutions are sought in the form:

$$U_{total} = \overline{U}_g + u_{ag}(X,Z,T) \tag{2.3a}$$

$$V_{total} = v_g(X,Z,T) \tag{2.3b}$$

$$W_{total} = w(X,Z,T) \tag{2.3c}$$

$$\Theta_{total} = \overline{\Theta}(Y,Z) + \theta(X,Z,T) \tag{2.3d}$$

$$\Phi_{total} = \overline{\Phi}(Y,Z) + \Phi(X,Z,T). \tag{2.3e}$$

The inviscid system of equations is comprised of two prognostic equations [one for the anomalous potential vorticity ($q_g = Q_g - 1$) and another for the potential temperature (θ) on the upper and lower model boundaries] and two diagnostic equations [one for the modified geopotential ($\Phi = \varphi + v_g^2/2$) and another for the cross-frontal streamfunction (ψ)]. For simplification, the model parameters can be reduced by an appropriate choice of dimensionless variables. The dimensionless system has a zonal scale of 1000 km, a vertical scale of 10 km, one advective time unit corresponds to 9.25 hours, both the zonal and meridional velocity scale are 100 m/s, the potential temperature scale is 30 K and the ageostrophic scaling for u_{ag} and w are 30 m/2 and 30 cm/s, respectively. The dimensionless equations for the disturbance field are:

$$\left(\frac{\partial}{\partial T} + Z\frac{\partial}{\partial X}\right)q_g + w\frac{\partial}{\partial Z}q_g = J\frac{\partial}{\partial Z}\left\{w^*\left(1+q_g\right)\left[1-R(Z)\right]\right\} \tag{2.4a}$$

$$\left(\frac{\partial}{\partial T} + Z\frac{\partial}{\partial X}\right)\theta = \frac{\partial \Phi}{\partial X}, \quad \text{on Z=0,1} \tag{2.4b}$$

$$\left(q_g + 1\right)\frac{\partial^2 \Phi}{\partial X^2} + \frac{\partial^2 \Phi}{\partial Z^2} = q_g \tag{2.4c}$$

$$\frac{\partial}{\partial X}\left(Q_{geff}\frac{\partial \psi}{\partial X}\right) + \frac{\partial^2 \psi}{\partial Z^2} = -2\frac{\partial^2 \Phi}{\partial X^2} \tag{2.4d}$$

where:

1) The RHS of Equation 2.4a is replaced by zero when w < 0.

2) The quantity

$$Q_{geff} = \begin{cases} (1+q_g)R(Z) & when\ w > 0 \\ (1+q_g) & when\ w < 0 \end{cases} \tag{2.4e}$$

3) R(Z) is a vertically varying moisture parameter defined as,

$$R(Z) = \frac{\Gamma_m S_e(Z)}{\Gamma_d} \approx \frac{\Gamma_m S_e(X,Z;T)}{\Gamma_d} \tag{2.5a}$$

$$S_e = \frac{Q_{ge}}{Q_g} \tag{2.5b}$$

where Q_{ge} is the moist potential vorticity, Q_g the dry potential vorticity, Γ_m the moist adiabatic lapse rate and Γ_d the dry adiabatic lapse rate.

4) In this model setting, the vertical profile of latent heat release is largely controlled by the moisture parameter (R), essentially a measure of the deviation from moist neutrality along a constant absolute momentum surface. We adopt two choices for the moisture parameter,

$$R(Z) = R_o \tag{2.5c}$$

$$R(Z) = R_o + (1 - R_o)Z \tag{2.5d}$$

where R_0 is a constant. For reference, R(Z) equal to 1.0 everywhere corresponds to the dry case.

5) The starred ageostrophic velocities and the unstarred ageostrophic velocities are obtained via the expressions:

$$u_{ag}^{*} = \frac{\partial \psi}{\partial Z} \tag{2.6a}$$

$$w^{*} = -\frac{\partial \psi}{\partial X} \tag{2.6b}$$

$$w = Jw^{*} \tag{2.6c}$$

$$u_{ag} = u_{ag}^{*} - w\left(\frac{\partial^2 \Phi}{\partial Z \partial X}\right) \tag{2.6d}$$

$$J = \left[1 - \left(\frac{\partial^2 \Phi}{\partial X^2}\right)\right]^{-1} \tag{2.6e}$$

where J denotes the Jacobian of the transformation between the real and geostrophic coordinates. J represents the ratio of the vertical component of the absolute vorticity to f, the Coriolis parameter.

6) The fields in physical coordinates (x,z) are obtained via transformation from geostrophic coordinates:

$$x = X - v_g(X, Z, T) \tag{2.6f}$$

$$z = Z \tag{2.6g}$$

7) The boundary conditions on the geopotential Φ are that it remain periodic in X and satisfy $\theta = \partial\Phi/\partial Z$ along the horizontal boundaries Z = 0,1. The boundary conditions on the streamfunction ψ are that it remain periodic in X and vanish on the horizontal boundaries Z = 0,1 (for the inviscid system).

The model is integrated in the geostrophic coordinates and all fields are transformed back to real coordinates.

The dimensionless system has a zonal scale of 1000 km, a vertical scale of 10 km, one advective time unit corresponds to 9.25 hours, both the zonal and meridional velocity scale are 100 m/s, the potential temperature scale is 30 K, and the ageostrophic scaling for u_{ag} and w are 30 m/s and 30 cm/s, respectively.

The initial condition is comprised of the modified geopotential field (Φ) throughout the domain. From this information, self-consistent initial conditions are calculated for the anomalous potential vorticity (q_g), the potential temperature (θ), and the cross-frontal streamfunction (ψ). Integration proceeds by advancing q_g and θ on the boundaries in time, and then solving the diagnostic equations for the updated Φ and ψ. The process is then repeated for each time step. All time derivatives are solved numerically using a 2nd order Adams-Bashforth scheme, while a simultaneous over-relaxation (SOR) technique is used to calculate spatial derivatives.

The power method is used in this study. As an initial condition, the model is supplied with the geopotential field of a small amplitude, dry Eady normal mode of particular wavenumber / wavelength. The wave is then allowed to evolve over time. The process is repeated for numerous wavenumbers over the desired subspace.

(i) *Ekman Pumping*

The inviscid, dimensionless model equations (2.4a-d) must be altered when an Ekman boundary layer is included and the vertical velocity is allowed to be non-zero on the lower boundary (Z=0). While the prognostic anomalous PV equation and the diagnostic equations for the modified geopotential and transverse streamfunction (2.4a, c and d) remain correct as written, it should be noted they do change in practice on and near the lower boundary. For example, the vertical advection term on the LHS and the

diabatic heating term within the vertical derivative on the RHS of the prognostic anomalous potential vorticity equation (2.4a) must be calculated on the lower boundary.

Furthermore, the prognostic equation for the potential temperature on the lower boundary (2.4b) takes on a much more complicated form. The dimensionless equation can be written as:

$$\left(\frac{\partial}{\partial \mathrm{T}}+\mathrm{Z}\frac{\partial}{\partial \mathrm{X}}\right)\theta+\mathrm{w}\frac{\partial\theta}{\partial \mathrm{Z}}=\frac{\partial\Phi}{\partial \mathrm{X}}+\dot{\theta} \quad \text{, on Z=0} \tag{2.7a}$$

The vertical advection term on the LHS of (2.7a) can be re-written,

$$\mathrm{w}\frac{\partial\theta}{\partial \mathrm{Z}}=\mathrm{w}^{*}\mathrm{J}\frac{\partial\theta}{\partial \mathrm{Z}}=\mathrm{w}^{*}\mathrm{Q}_{\mathrm{g}}=\mathrm{w}^{*}(1+\mathrm{q}_{\mathrm{g}}) \tag{2.7b}$$

and the diabatic heating term ($\dot{\theta}$) on the RHS of (2.7a) can be expressed as

$$\dot{\theta}=\mathrm{w}^{*}(1+\mathrm{q}_{\mathrm{g}})[1-\mathrm{R(Z)}] \tag{2.7c}$$

Incorporating these terms gives the revised potential temperature equation used in the model,

$$\left(\frac{\partial}{\partial T}+Z\frac{\partial}{\partial X}\right)\theta+w^{*}(1+q_{g})=\frac{\partial\Phi}{\partial X}+w^{*}(1+q_{g})[1-R(Z)] \quad \text{, on Z=0} \tag{2.7d}$$

2.1.2 Estimate of Growth Rate

An important quantification of the evolution a baroclinic wave is the estimation of the instantaneous growth rate (σ), a measure of the intensification of the wave with time. The general formula used is,

$$\sigma=\frac{\Phi_{sfc}^{t+1}-\Phi_{sfc}^{t}}{\Delta t\cdot\left[\left(\Phi_{sfc}^{t+1}+\Phi_{sfc}^{t}\right)/2.0\right]} \tag{2.8}$$

where Φ_{sfc} is a measure of the geopotential minimum at the surface (Z = 0). The superscript t and t+1 in 2.8 represent two model times: time t+1 is equal to the time t

plus the model time step (Δt). Φ_{sfc} is a logical choice for the estimate of σ. It was used by EFT, and it is often used as a measure of cyclone intensity by forecasters and researchers alike.

To explore the sensitivity of σ to this choice, the calculation was also made using the maximum meridional wind at the surface ($v_{g,sfc}$) in 2.8. A comparison of the temporal evolution of σ for both variables for a wavenumber 2.3 disturbance, including moist dynamics, is presented in Figure 2.1. While the two methods give qualitatively similar results, a few features are worth noting. On average, the estimate of σ using Φ_{sfc} is slightly larger, and it exhibits less variability over both short and long time scales. One likely explanation, and a good argument for using Φ_{sfc} in 2.8, is that Φ_{sfc} always occupies the same position in relation to the overall wave structure. On the contrary, this cannot be assumed for $v_{g,sfc}$. It may vary spatially and, thus, lead to variability in the estimate of σ.

The temporal evolution of σ (using Φ_{sfc}) for the above wave is shown in Figure 2.2. For a pure normal mode, σ would be constant with time. However, Figure 2.2 clearly illustrates that the model solution for σ does change with time. Two noteworthy features are: 1) the oscillatory behavior of σ over very short time scales, and 2) the evolution of σ over long time scales. The former appears inherent to the model numerics. It is a simple matter to filter out this oscillation by averaging over time. The latter feature is indicative of the wave transformation from a dry normal mode to a moist normal mode. The transformation process is readily apparent in the wave structure, most conspicuously in the vertical velocity (w) field (see Figure 2.3). Normal mode structure is characterized by one region of ascent; however, in evolving from the dry to moist normal mode, there exists a period where multiple ascent regions are observed. This process was also noted by EFT and JT. Given sufficient time, the w field structure returns to a single ascent region. At this time, an estimate of σ can be calculated by averaging over an appropriate

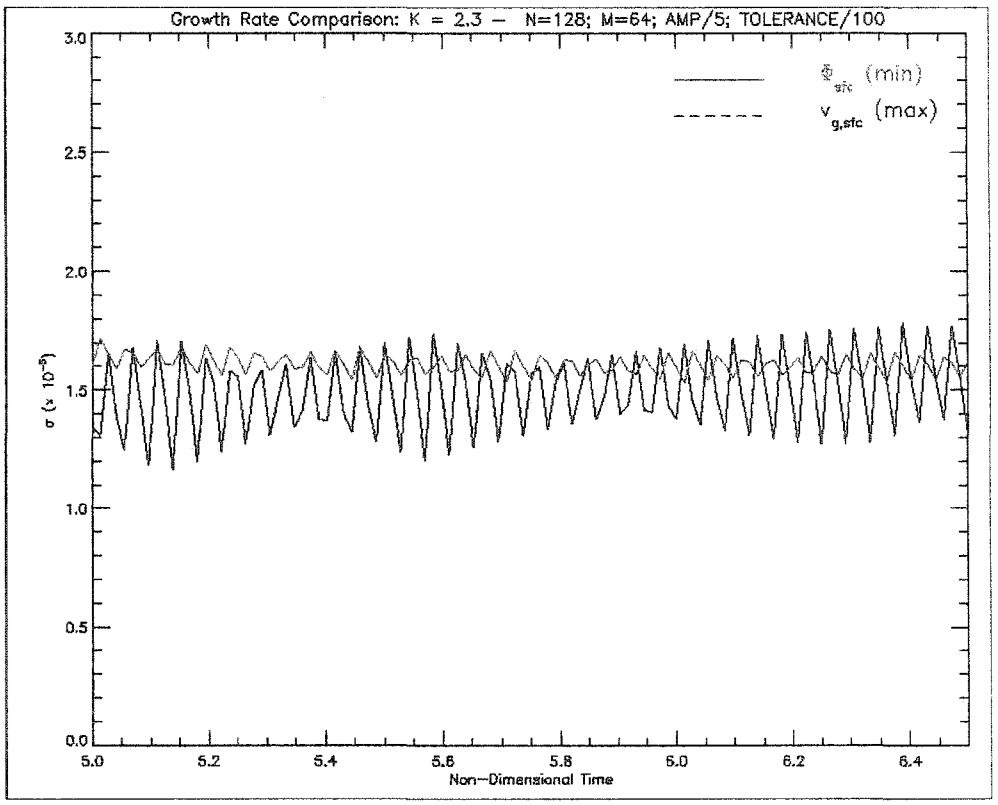

Figure 2.1 – Comparison of the evolution of the growth rate for a wavenumber 2.3 disturbance using two different field variables [the minimum surface geopotential (Φ_{sfc}) and the maximum surface meridional wind ($v_{g,sfc}$)].

time frame when σ is near constant with time and non-linear effects are negligible (i.e. when the magnitude of the advective terms is quite small due to the small value of the flow field).

2.1.3 Model Sensitivity and Validation

(i) *Resolution*

Numerous tests were made to determine the model sensitivity to variable resolution in space and time. Figure 2.4 shows the sensitivity of the growth rate (σ) to variations in the horizontal resolution for a wavenumber 2.2 disturbance. There are two major changes in the model solution in response to the increased horizontal resolution:

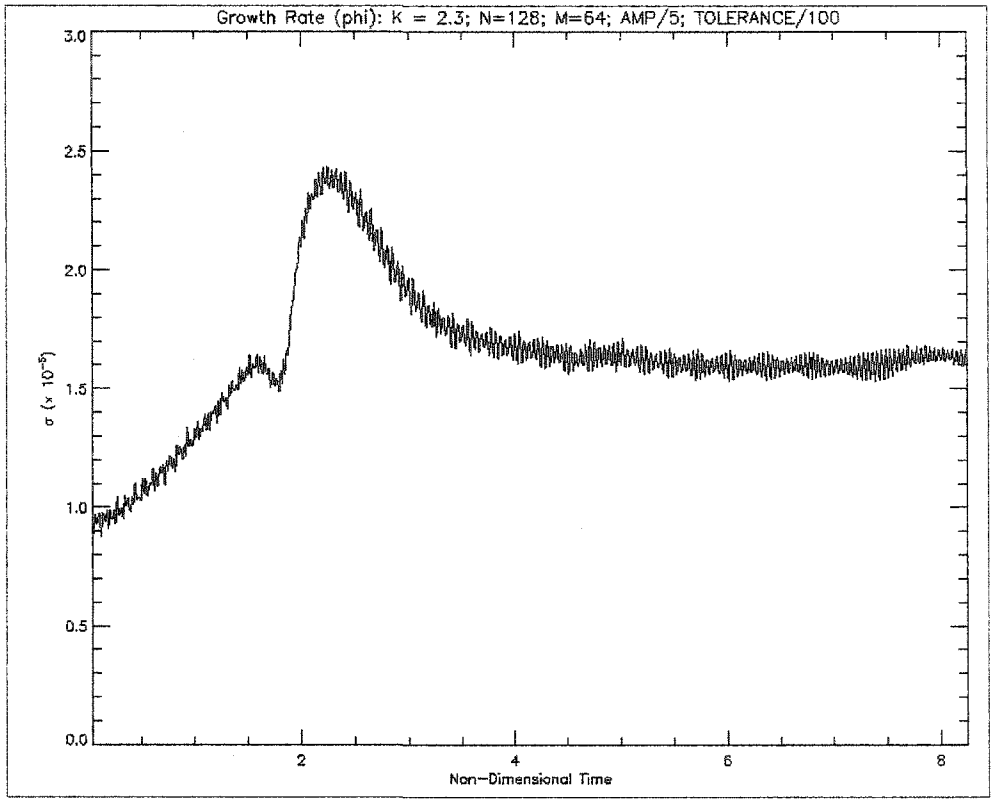

Figure 2.2 – The evolution of the growth rate for a wavenumber 2.3 disturbance using the minimum surface geopotential (Φ_{sfc}).

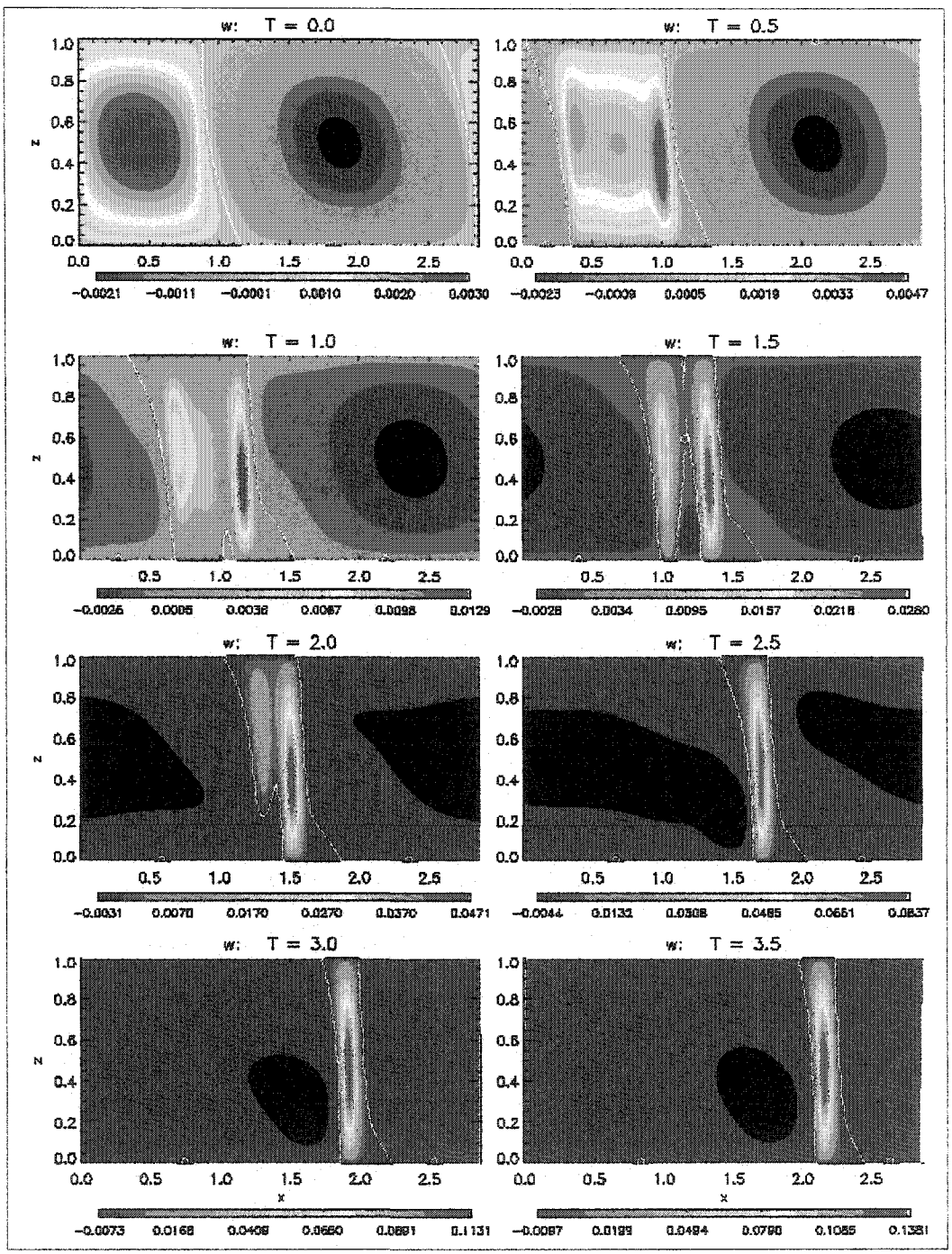

Figure 2.3 – The evolution of the vertical velocity (w) for a wavenumber 2.3 disturbance incorporating 128 horizontal grid points.

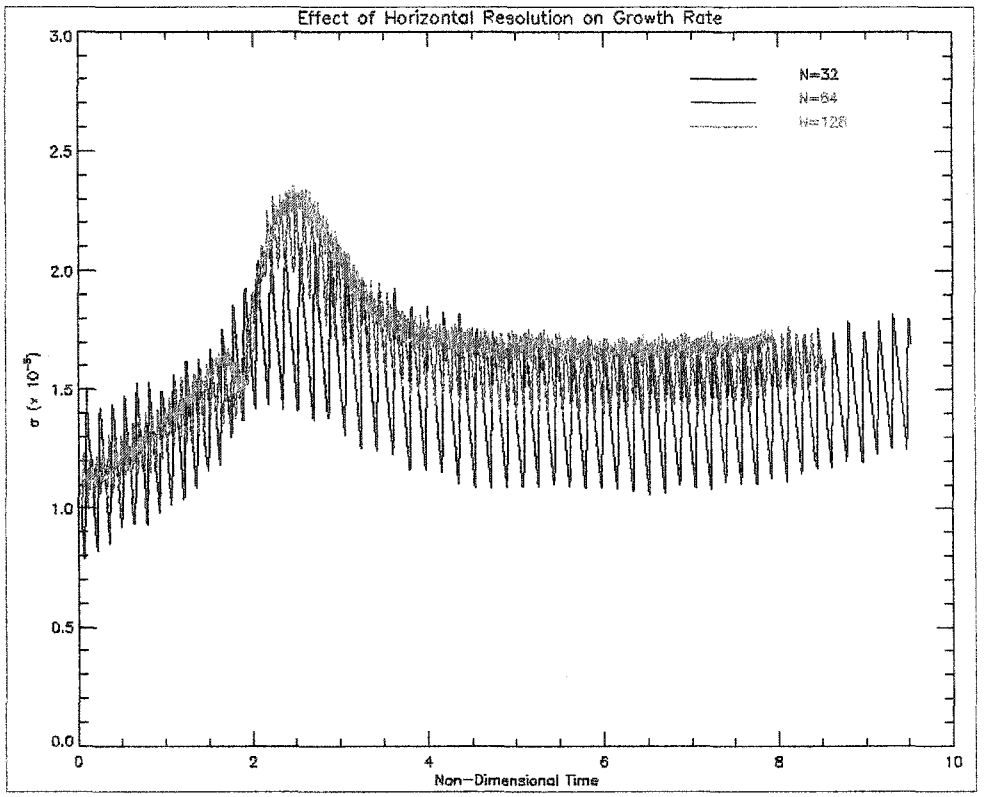

Figure 2.4 – The effect of horizontal resolution on the evolution of the growth rate for a wavenumber 2.2 disturbance.

1) a decrease in the magnitude of the oscillation of σ over short time scales, and 2) an increase in the estimate of σ. As one might expect, increased resolution allows for a more detailed representation of the dynamical processes at work. Again, this is most apparent in the vertical velocity (w) field. The evolution of w with time using a reduced horizontal resolution (32 versus the 128 grid points in Figure 2.4) is presented in Figure 2.5. The higher horizontal resolution is better able to capture the transformation from the dry Eady mode to the moist Eady mode discussed in the previous subsection. Specifically, it is able to resolve the multiple ascent regions that appear.

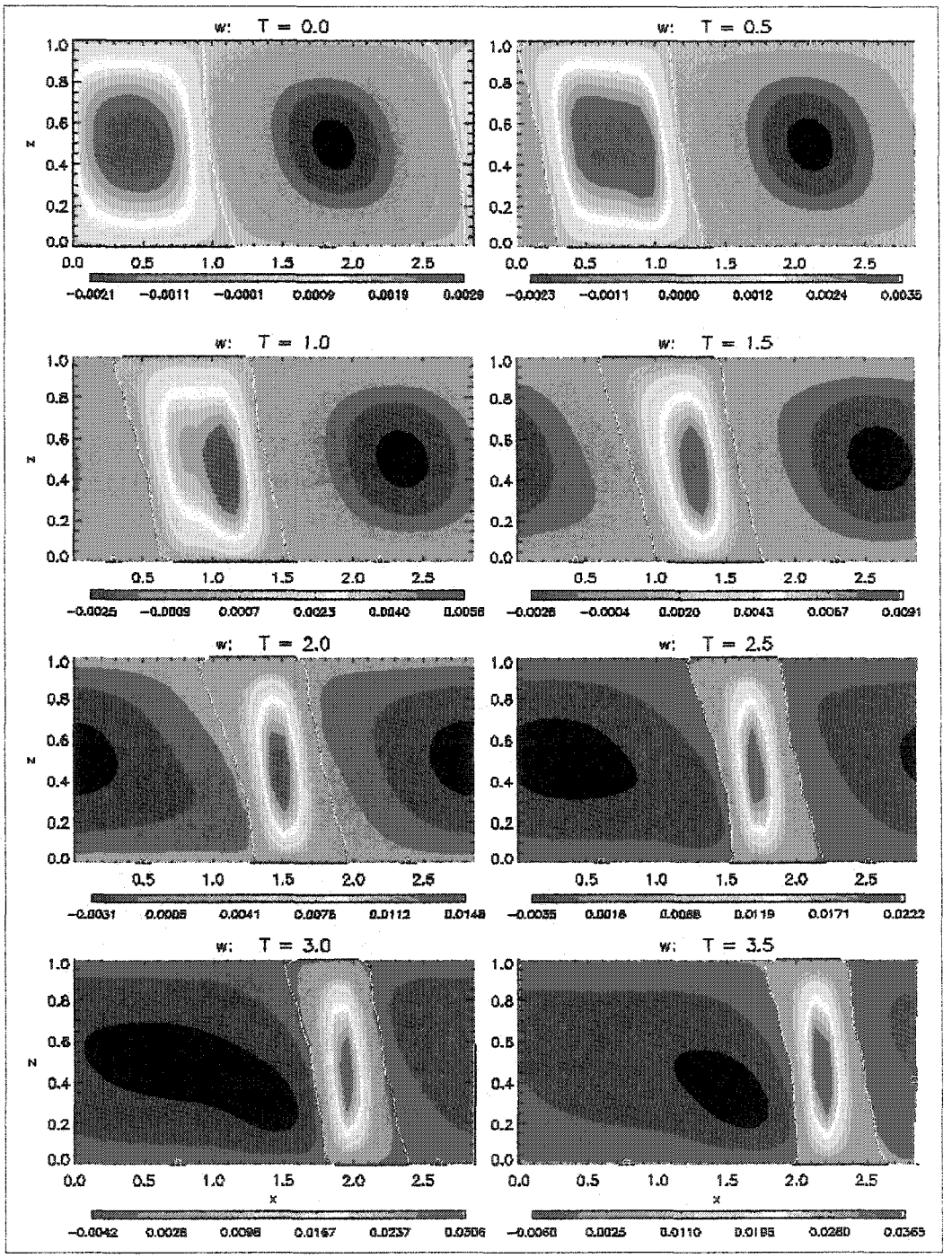

Figure 2.5 – The evolution of the vertical velocity (w) for a wavenumber 2.3 disturbance incorporating 32 horizontal grid points.

Increasing the vertical resolution has the opposite effect. Figure 2.6 illustrates that an increase in vertical resolution (64 versus 32 grid points) results in a decrease in the magnitude of σ, consistent with the findings of JT.

Finally, the results are insensitive to variations in the temporal resolution, provided the time step is small enough to meet the Courant-Fredrichs-Lewy necessary condition for stability.

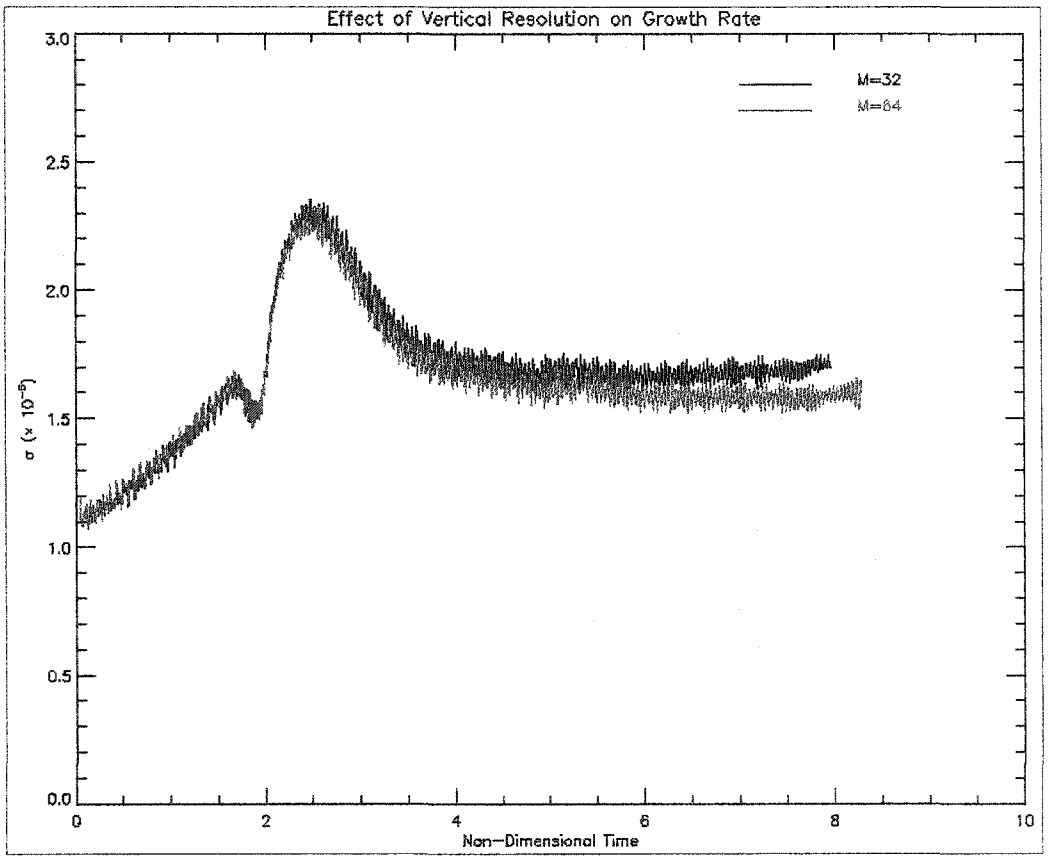

Figure 2.6 – The effect of vertical resolution on the evolution of the growth rate for a wavenumber 2.2 disturbance.

(ii) *Time Stepping Technique*

To determine the sensitivity of the model solution to the Adams-Bashforth time stepping routine, a leapfrog technique was also introduced. The general form for an explicit three-time-level method is (Durran 1999),

$$\phi^{t+1} = \alpha_1 \phi^t + \alpha_2 \phi^{t-1} + \beta_1 \Delta t F\left(\phi^t\right) + \beta_2 \Delta t F\left(\phi^{t-1}\right) \tag{2.9a}$$

where F is the derivative function to be evaluated and the variables α and β are coefficients. For a 2nd order Adams Bashforth method, the coefficient values are $\alpha_1 = 1$, $\alpha_2 = 0$, $\beta_1 = 3/2$, and $\beta_2 = -1/2$. In contrast, if the coefficient values are changed to $\alpha_1 = 0$, $\alpha_2 = 1$, $\beta_1 = 2$, and $\beta_2 = 0$, one is left with a leapfrog technique.

The weakness inherent in the leapfrog scheme is that it contains an undamped computational mode, which generally amplifies and generates a computational instability that is not representative of the continuous-in-time equation of motion (Durran 1999). To control the undamped mode, a Robert-Asselin time filter is incorporated into the time integration cycle. After each leapfrog step, the following filtering operation is used to arrive at the value used in the model,

$$\overline{\phi^t} = \phi^t + \gamma(\overline{\phi^{t-1}} - 2\phi^t + \phi^{t+1}) \tag{2.9b}$$

where γ is a filter parameter. Through a trial and error process, a value for γ of 0.2 was chosen.

A series of model runs were conducted, with the sole difference being the time stepping scheme, to determine the sensitivity of the results to the particular scheme used. Figure 2.7 shows the evolution of the wave structure for the resulting disturbance using the respective time stepping techniques (wavenumber 2.2.). It is clear that the wave evolution exhibits little to no dependence on the time stepping scheme.

(iii) *Model Parameters*

The model also exhibits sensitivity to model parameters. One of the most notable is the convergence criterion incorporated in the SOR technique. The result of a decrease by two orders of magnitude in the acceptable residual is a smoother estimate of the

2.7a) LEAPFROG

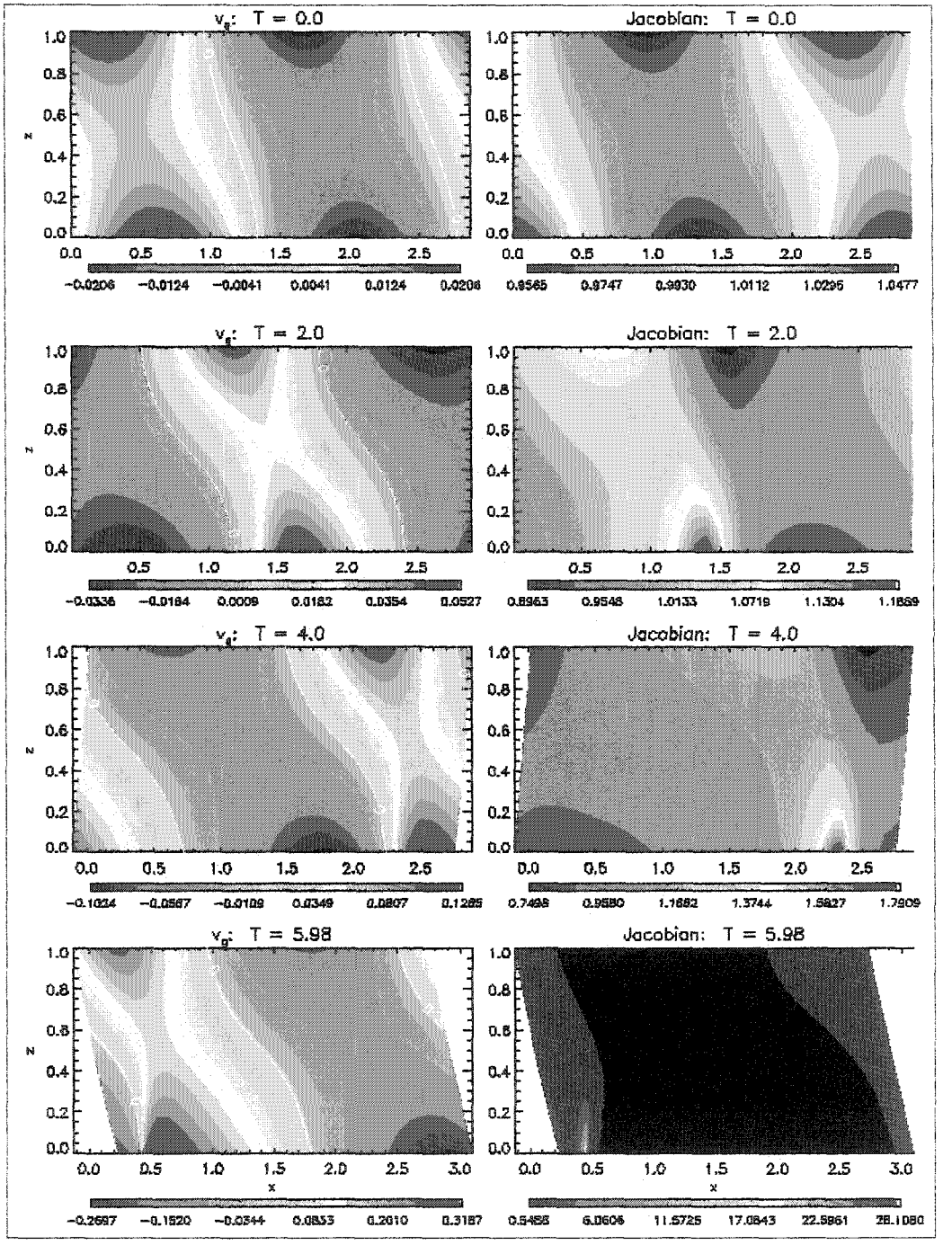

2.7b) ADAMS-BASHFORTH

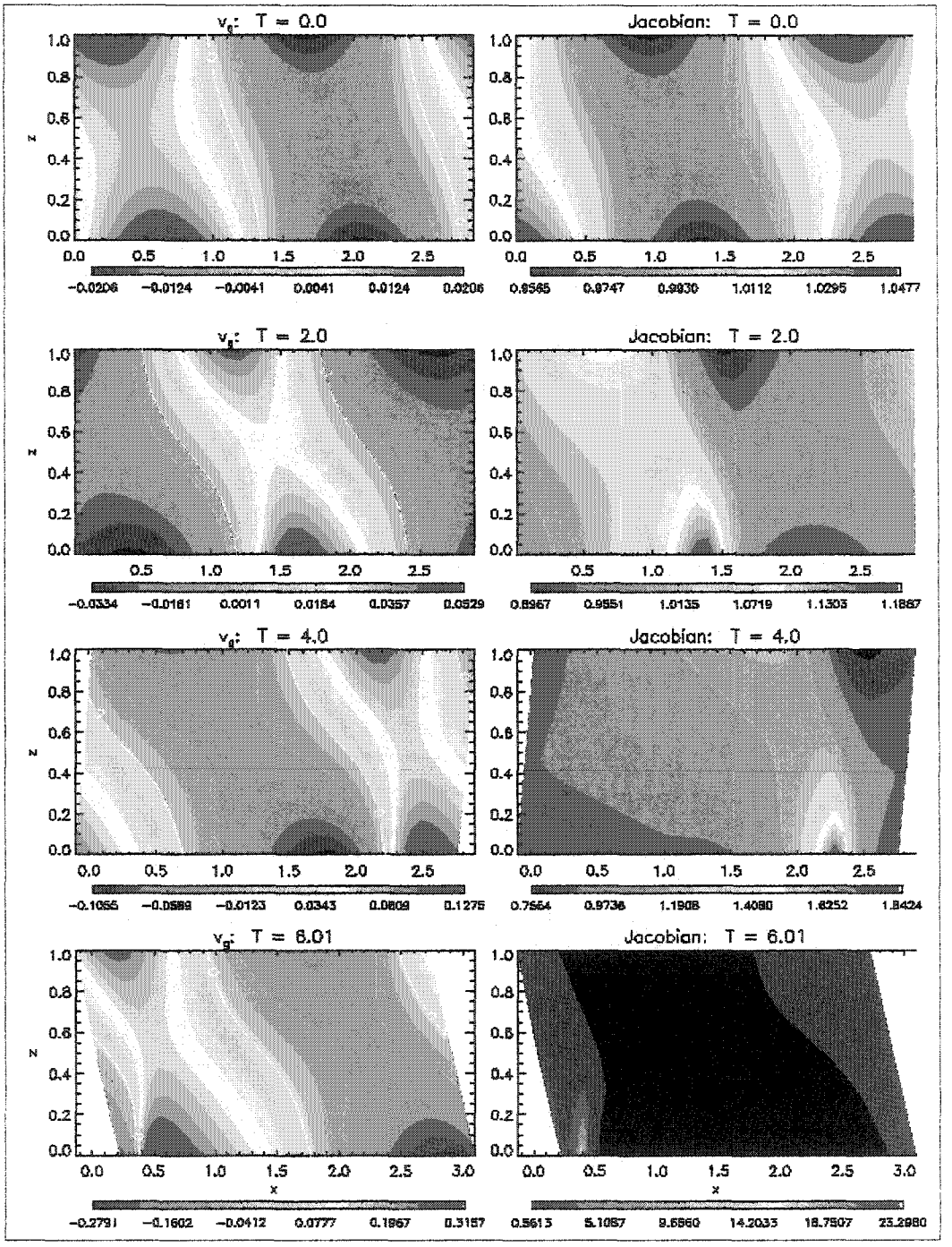

Figure 2.7 – The evolution of the meridional wind (v_g) and the Jacobian for a wavenumber 2.3 disturbance for two time-stepping schemes: a) leapfrog, and b) 2nd order Adams-Bashforth.

temporal evolution of σ, especially early in the simulation when the wave is characterized by very small perturbations (Figure 2.8). The value adopted for the numerical experiments is 10^{-6}.

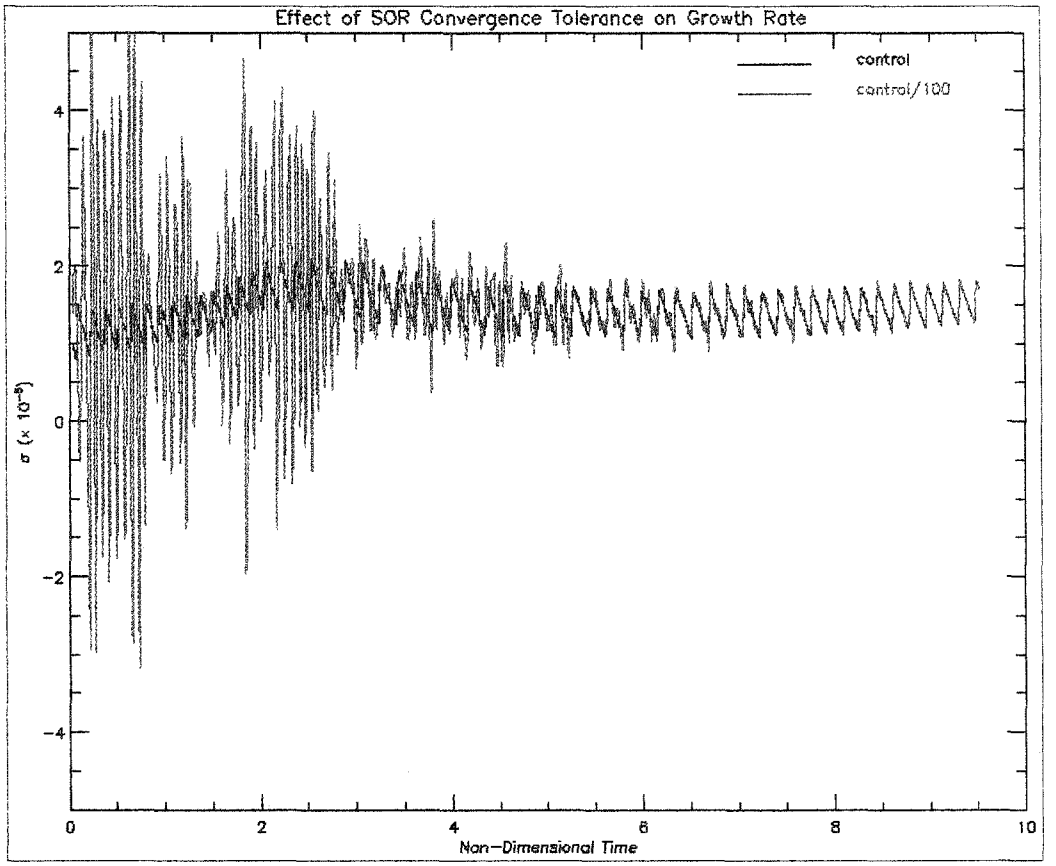

Figure 2.8 – The effect of the SOR convergence on the evolution of the growth rate for a wavenumber 2.2 disturbance.

(iii) *Solutions to the Dry Eady Problem*

An analytical solution does exist for the dry Eady problem. As a first step in model validation, it is essential to be able to recreate the solutions to the dry system. The procedure outlined in sections 2a and 2b are used to calculate the growth rates. The moisture parameter (Equation 2c) is set to 1.0 throughout the domain, the physical

equivalent of an environment with no latent heat release. Figure 2.9 compares the model and analytic solutions of the growth rate as a function of wavenumber for a subspace of unstable wavelengths. The two curves compare quite well, illustrating that in the case of dry dynamics, the model is performing satisfactorily.

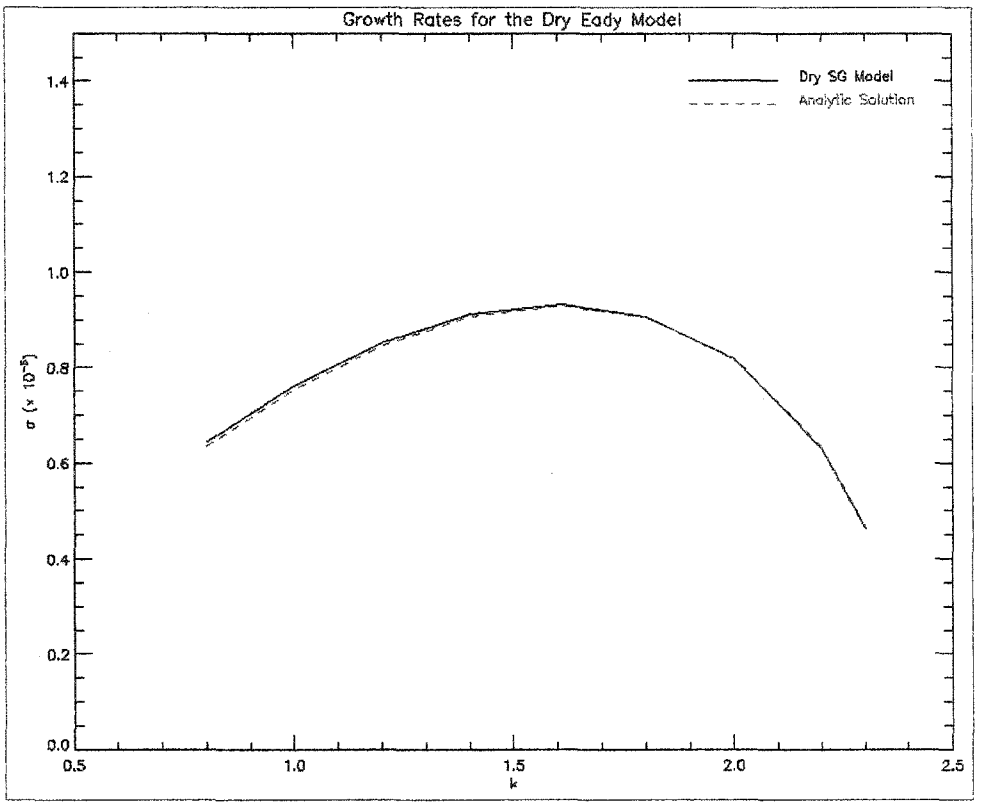

Figure 2.9 – Growth rate as a function of wavenumber for the dry Eady problem. Solutions for the 2D, Semigeostrophic model (black solid line) and the analytic solution (red dashed line) are presented.

Figure 2.10 shows the structural evolution of the most unstable, dry normal mode (wavenumber = 1.61; wavelength ≈ 3900 km). The mutual interaction between the upper and lower level disturbances results in a phase locked baroclinic wave that amplifies as it translates with the steering level flow. The baroclinic conversion of available potential energy to kinetic energy is occurring, as indicated by the westward tilt of v_g with height.

2.10a)

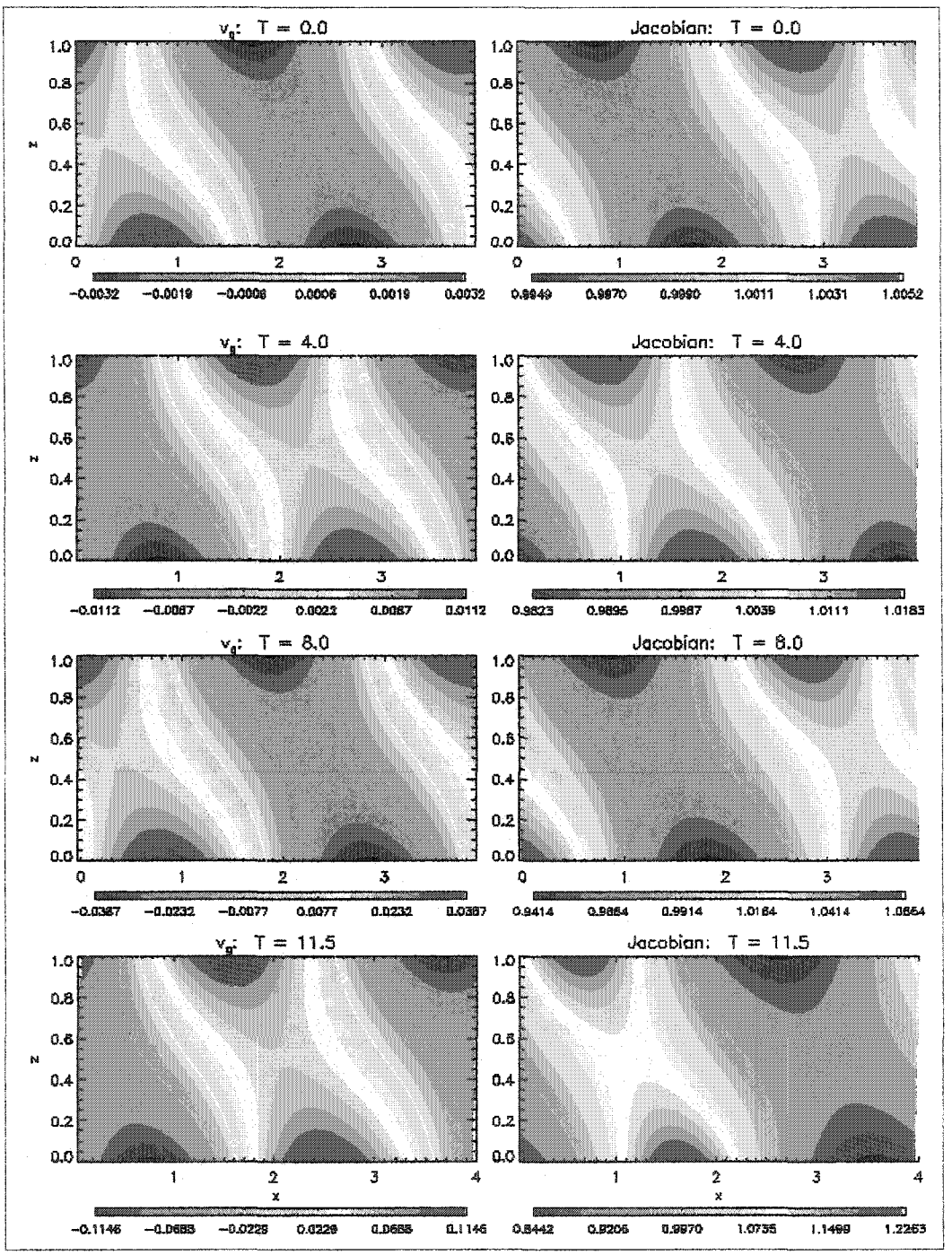

2.10b)

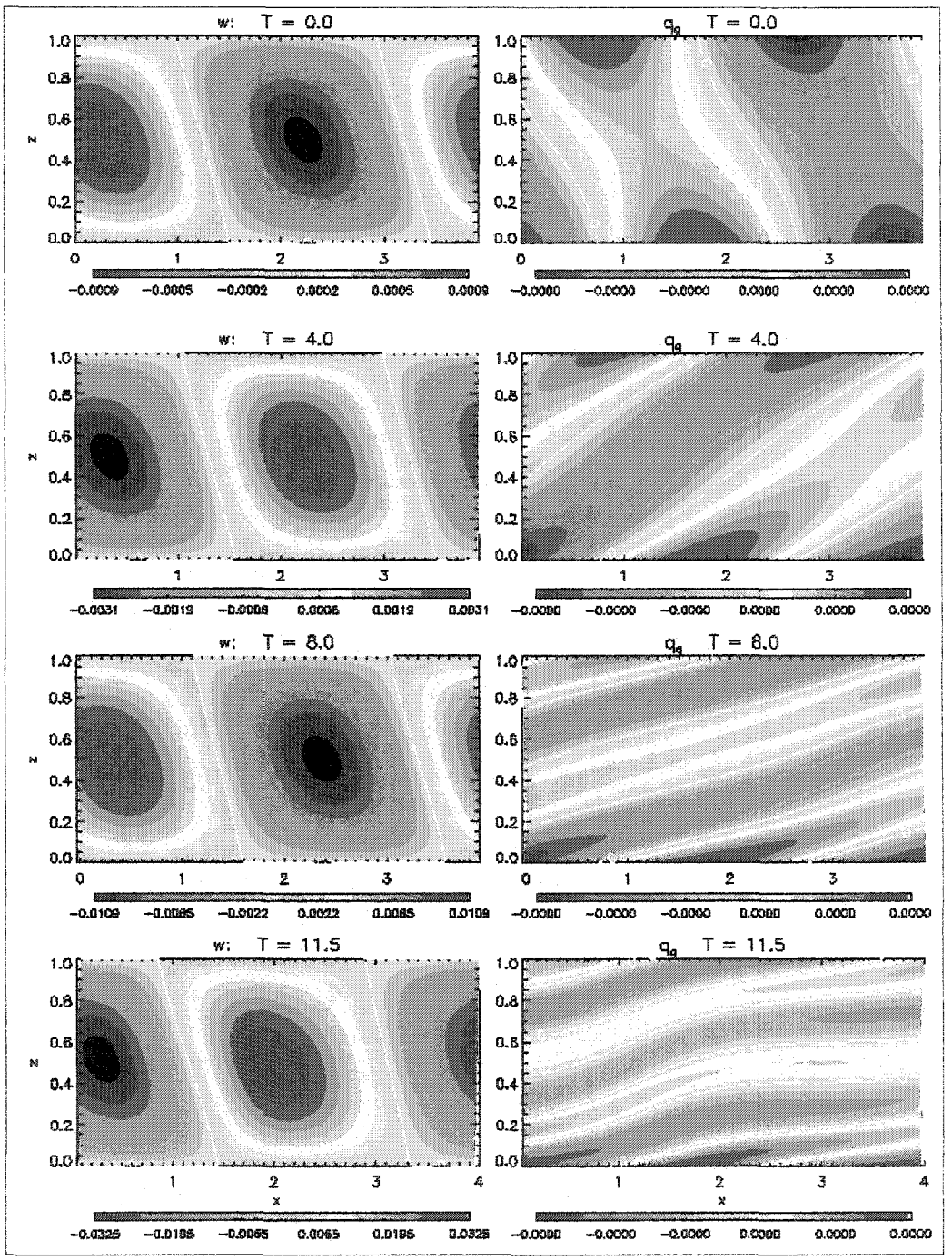

Figure 2.10 – The evolution of the most unstable dry Eady normal mode: a) the meridional wind (v_g) and the Jacobian; and b) the vertical velocity (w) and the anomalous potential vorticity (q_g).

In the dry system, the right hand side of Equation 1a demonstrates that the anomalous PV (q_g) cannot be created nor destroyed. Therefore, the temporal evolution of the initial q_g field is due solely to local advection by the zonal wind, resulting in the distorted structure seen at later times in Figure 2.10.b. [As a clarification, q_g is exactly zero at all points for a dry Eady wave, and it is the discretization error that is being distorted by the environmental flow.] Finally, it should be noted for future comparison that the horizontal scale of the ascent and descent regions are identical and do not vary with time.

2.2 The PSU/NCAR Mesoscale Modeling System (MM5)

To examine DRV formation, growth and evolution in a more complete and realistic three-dimensional setting, the PSU/NCAR mesoscale modeling system (MM5) is used to conduct a number of idealized simulations of the DRV lifecycle.

2.2.1 Model Summary

MM5 is a limited-area, non-hydrostatic, terrain-following sigma-coordinate numerical model. A complete description of MM5, including the model equations and their derivations can be found at (http://www.mmm.ucar.edu/mm5/documents/tutorial-v3-notes.html).

In this study, an idealized initial condition is used for all model simulations. With few exceptions, the initial condition is comprised of a low-level, perturbation vortex embedded on the southern side of a moist, baroclinic zone over an ocean surface. We will focus on disturbance growth in the middle latitudes during the northern hemisphere winter. An outline of the model setup for this study is given in this section.

With the exception of the sensitivity experiments exploring the effects of model-based parameters (e.g. cumulus parameterization, horizontal grid spacing, surface heat fluxes, surface friction), the following choices are used for all model runs: a domain size of approximate 12000 by 5000 km in the zonal and meridional directions, respectively; a horizontal grid spacing of approximately 90 km (with a Lambert Conformal map projection); 23 vertical levels; the simple ice (Dudhia) moisture scheme; the Grell cumulus parameterization (Grell et al. 1994); the MRF planetary boundary layer (Hong and Pan 1996); and no latent and sensible heat surface fluxes. The latter choice is consciously made to negate the possibility of an air-sea interaction type growth mechanism, as articulated by Ooyama (1969) and Rotunno and Emanuel (1987) for tropical cyclones and Emanuel and Rotunno (1989) for arctic hurricanes.

2.2.2 Initial Condition

(i). *Initial Basic State Baroclinic Zone*

Within the basic state baroclinic zone (between 25N and 65N), the basic state zonal flow ($\overline{U}$) vanishes at Z = 0 and attains its maximum at the tropopause. Outside this area, $\overline{U}$ is identically zero at all levels. At the tropopause, $\overline{U}$ varies sinusoidally from zero at 25N to its maximum value (defined by the imposed maximum vertical wind shear) at 45N and back to zero at 65N.

This procedure defines a meridionally-varying vertical wind shear [$\partial_z \overline{U} = S(y)$] that is used to compute the basic state geopotential ($\overline{\Phi}$) and potential temperature ($\overline{\Theta}$) fields as follows,

$$\overline{\Phi}(y,Z) = -\left[f \cdot S(y) \cdot y \cdot Z\right] + \left(\frac{N_T{}^2 Z^2}{2}\right) + gZ \qquad (2.10a)$$

$$\overline{\Theta}(y,Z) = -\left[g^{-1}\cdot\theta_0\cdot f\cdot S(y)\cdot y\right] + g^{-1}N_T{}^2\theta_0 Z + T_{25N} \qquad (2.10b)$$

where f is the Coriolis parameter ($2\Omega\sin\varphi$), N_T^2 is the static stability (10^{-4} s^{-2}), θ_0 is the reference potential temperature (294 K), and T_{25N} is the surface temperature at 25N. The y function in 2.10a-b represents the distance (in meters) from 25N, and Z is the pseudoheight (Hoskins and Bretherton 1972), defined as follows,

$$Z = -H\cdot\ln\left(\frac{p}{p_s}\right) \qquad (2.10c)$$

Values of $\overline{\Phi}$ and $\overline{\Theta}$ south of 25N and north of 65N assume their values at 25N and 65N, respectively.

A sloping tropopause is introduced (high to low pseudoheight from the south to the north) by using the following relationship,

$$H_{trop} = H + \left[\left(\frac{S_{45N}}{3.0}\right)\cdot H_{dev}\cdot\cos\varphi\right] \qquad (2.10d)$$

where H_{dev} is the maximum deviation from the average tropopause height, and $\cos\varphi$ ranges from 1 to –1 at the southernmost and northernmost latitudes of the baroclinic zone, respectively.

The model stratosphere is based on parameter values on the tropopause. The potential temperature is calculated as follows,

$$\overline{\Theta}_S(y,Z) = \overline{\Theta}_{trop} + (Z - H_{trop})\cdot N_S^2\cdot\left(\frac{\theta_0}{g}\right) \qquad (2.10e)$$

where N_S^2 is the static stability in the stratosphere. The zonal wind field is given by,

$$U_S(y,Z) = U_{trop} + (Z - H_{trop})\cdot\left[\frac{(U_{trop}\cdot FRAC) - U_{trop}}{H_{top} - H_{trop}}\right] \qquad (2.10f)$$

where FRAC is a user defined number (< 1) that determines the zonal wind at the top of the model. The term in brackets represents the vertical wind shear in the stratosphere. Finally, the geopotential field in the stratosphere is recovered from the zonal wind field by assuming geostrophic balance.

(ii). *Initial Perturbation Vortex*

The perturbation field is represented by a coherent vortex that is placed on the southern side of the baroclinic zone. The initial perturbation field is constructed by assuming: i) a delta function of potential temperature on the lower boundary; and ii) zero quasigeostrophic (QG) potential vorticity (PV) in the interior.

The equation for the QG, perturbation PV in the interior is,

$$q' = \frac{1}{f}\nabla_H^2\phi' + \frac{1}{\rho}\frac{\partial}{\partial Z}\left(\frac{f\rho}{N_T^2}\frac{\partial\phi'}{\partial Z}\right) \tag{2.11a}$$

If f, ρ and N_T^2 are assumed constant, (1.8) becomes,

$$q' = \frac{1}{f}\nabla_H^2\phi' + \frac{f}{N_T^2}\frac{\partial^2\phi'}{\partial Z^2} \tag{2.11b}$$

Assumption ii) above, allows for the following simplification of (2.11b),

$$\frac{1}{f}\nabla_H^2\phi' + \frac{f}{N_T^2}\frac{\partial^2\phi'}{\partial Z^2} = 0 \tag{2.11c}$$

Assuming wavelike solutions of the form,

$$\phi'(k,l,Z) = \hat{\phi}(Z)\exp[i(kx+ly)] \tag{2.11d}$$

where k and l are the zonal and meridional wavenumbers, respectively, and substituting into (2.11c) gives,

$$\frac{d^2\hat{\phi}}{dZ^2} - \frac{N_T^2}{f^2}\left(k^2 + l^2\right)\hat{\phi} = 0 \tag{2.11e}$$

The solution of (2.11e) is,

$$\hat{\phi}(Z) = A\exp(CZ) + B\exp(-CZ) \tag{2.11f}$$

where

$$C = \frac{N_T}{f}\sqrt{k^2 + l^2} \tag{2.11g}$$

Physically, the solution must be bounded in Z, indicating that A must be equal to 0. This gives,

$$\phi'(k,l,Z) = B\exp(-CZ)\exp[i(kx + ly)] \tag{2.11h}$$

The hydrostatic equation for this system is given by,

$$\frac{g}{\theta_0}\theta' = \frac{\partial\phi'}{\partial Z} \tag{2.11i}$$

Assuming a wavelike solution for the perturbation potential temperature

$$\theta'(k,l,Z) = \hat{\theta}(Z)\exp[i(kx + ly)] \tag{2.11j}$$

and substituting (2.11j) and (2.11h) into (2.11i) gives,

$$\hat{\theta}(Z) = -BC\left(\frac{\theta_0}{g}\right)\exp(-CZ) \tag{2.11k}$$

$$\theta'(k,l,Z) = -BC\left(\frac{\theta_0}{g}\right)\exp(-CZ)\exp[i(kx + ly)] \tag{2.11l}$$

To solve for B, a lower boundary condition must be imposed. On Z=0, the perturbation potential temperature is assumed to take the form of a Gaussian in x and y,

$$\theta'(x,y,Z=0)=\exp\left[-\frac{(x^2+y^2)}{\sigma^2}\right],\ \text{on } Z=0 \tag{2.11m}$$

This initial condition is then transformed into Fourier space. The Fourier transform of a Gaussian in one spatial dimension is

$$\exp(-a^2x^2),a>0 \quad \text{is} \quad (a\sqrt{2})^{-1}\exp\left(-\frac{k^2}{4a^2}\right) \tag{2.11n}$$

(Gradstein and Ryzhik 1980, pg. 1147). For this case, $a=1/\sigma$. In two spatial dimensions, the Fourier transform is

$$\frac{\sigma^2}{2}\exp\left[-\frac{(k^2+l^2)\sigma^2}{4}\right] \tag{2.11o}$$

Equating (2.11o) and (2.11m) on Z=0 gives the following result for B,

$$B=-\frac{1}{C}\frac{g}{\theta_0}\left\{\frac{\sigma^2}{2}\exp\left[-\frac{(k^2+l^2)\sigma^2}{4}\right]\right\} \tag{2.11p}$$

Substituting (2.11g) and (2.11p) into (2.11h) and (2.11l) gives the initial condition for the perturbation geopotential and potential temperature (in Fourier space),

$$\phi'(k,l,Z)=-\left(\frac{g}{\theta_0}\right)\left(\frac{f}{N}\frac{1}{\sqrt{k^2+l^2}}\right)\left\{\frac{\sigma^2}{2}\exp\left[-\frac{(k^2+l^2)\sigma^2}{4}\right]\right\}\cdot$$

$$\exp\left[-\left(\frac{N_T}{f}\sqrt{k^2+l^2}\right)Z\right]\exp[i(kx+ly)] \tag{2.11q}$$

$$\theta'(k,l,Z)=\left\{\frac{\sigma^2}{2}\exp\left[-\frac{(k^2+l^2)\sigma^2}{4}\right]\right\}\exp\left[-\left(\frac{N_T}{f}\sqrt{k^2+l^2}\right)Z\right]\exp[i(kx+ly)]$$

(2.11r)

The final step is to transform the solution back to physical space using the following relation,

$$\phi',\theta'(x,y,Z)=\frac{1}{2\pi}\int_{-\infty}^{\infty}\int_{-\infty}^{\infty}\phi',\theta'(k,l,Z)dk\cdot dl \qquad (2.11s)$$

(iii). *Complete Initial Condition*

The complete initial condition is a combination of the basic state and perturbation fields.

$$U_{total}=\overline{U}_g(y,z)+u_g'(x,y,Z) \qquad (2.12a)$$

$$V_{total}=v_g'(x,y,Z) \qquad (2.12b)$$

$$\Theta_{total}=\overline{\Theta}(y,z)+\theta'(x,y,Z) \qquad (2.12c)$$

$$\Phi_{total}=\overline{\Phi}(y,z)+\phi'(x,y,Z). \qquad (2.12d)$$

The above formulation of the MM5 initial condition allows for the variation of many parameters, including: the magnitude of the baroclinic zone (and, consequently, the strength of the jet through the thermal wind relation), as well as the size and magnitude of the initial perturbation vortex.

2.2.3 Control Case

To ascertain the general features associated with DRV formation and structure, a 'typical' DRV simulation is presented in detail. The initial condition for this 'control case' is shown in Fig. 2.11 and its characteristics are as follows.

2.11a)

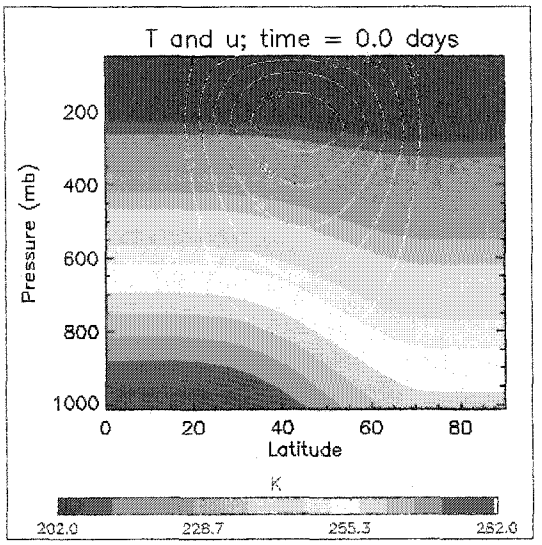

2.11b)

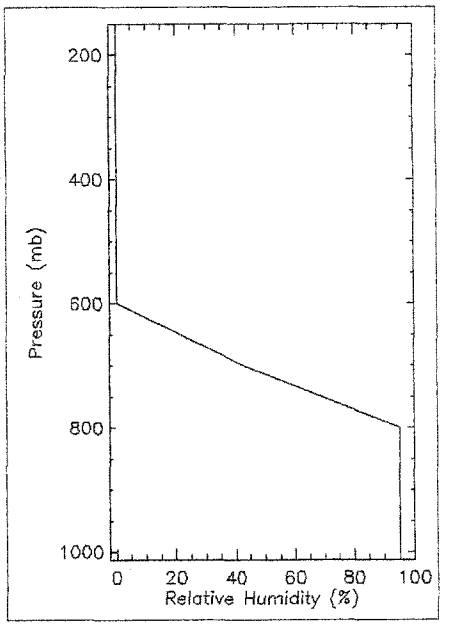

2.11c)

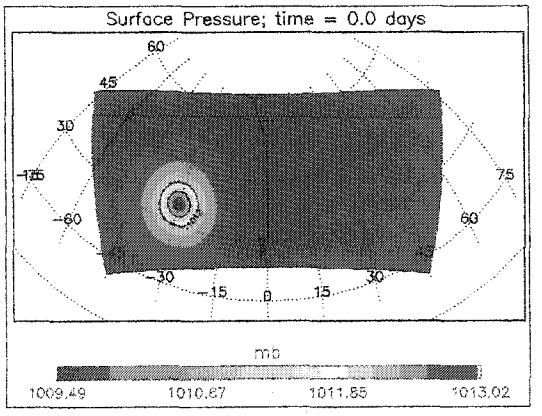

2.11d)

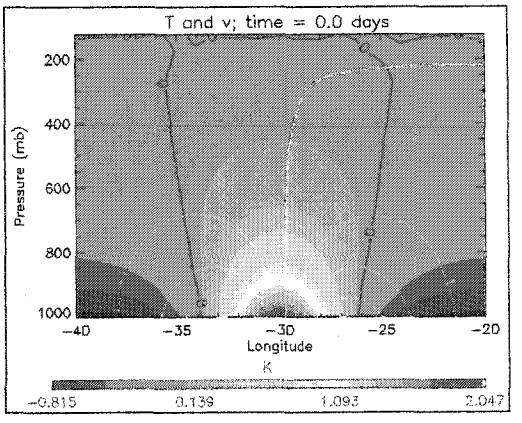

Figure 2.11 – Initial condition for the control simulation: a) the basic state temperature (K) in shading and the zonal wind field (overlaid contours; ms^{-1}) at a longitude 0; and b) the vertical profile of relative humidity (%); c) surface pressure (mb) and d) the temperature anomaly of the initial perturbation vortex (K) in shading and the meridional wind field (overlaid contours; ms^{-1}) at a latitude of 35N.

The basic state consists of a zonally-homogeneous, vertical wind shear in thermal wind balance with a y-varying meridional temperature gradient. The result is a

meridionally-symmetric jet with a maximum wind speed at the tropopause level. The meridional structure of the jet is defined by a sinusoidal variation of the zonal wind within the meridional channel of the jet (40 degrees of latitude for the control case). The maximum vertical wind shear (1.5 ms^{-1} / km) at the center of the baroclinic zone is exactly half that of the standard Eady basic state shear (3.0 ms^{-1} / km). This relatively meager value of vertical shear is chosen so as to avoid an interaction between the DRV and the upper levels. As shown by Wernli et al. (2002) in their study of extreme winter storm 'Lothar', this process does occur under certain environmental conditions and can have serious repercussions for both life and property. By avoiding this subspace of model solutions, however, we can concentrate on the intrinsic characteristics of the DRV.

Moisture is initialized in the form of a horizontally-homogeneous vertical profile of relative humidity. The atmosphere is nearly saturated (relative humidity of 95%) from the surface to 800 mb. Above this level, the relative humidity decreases linearly to 0% at 600 mb and remains dry to the top of atmosphere.

The perturbation field to represent the initial DRV is represented by a coherent, low-level warm core vortex [see section 2.2.2 (ii)]. A positive 3 K, delta-function perturbation in the potential temperature field on the lower boundary is assumed. The potential temperature perturbation decays horizontally from the center of the vortex in the form of a gaussian distribution (e-folding radius of 300 km) and exponentially with pseudoheight in the vertical. By enforcing the constraint of zero quasigeostrophic PV within the interior of the domain, a 3D solution for the geopotenital and potential temperature fields is attained.

The perturbation wind field is recovered from the perturbation geopotential field by assuming geostrophic balance. While there is in principle an inherent error involved in applying geostrophic balance to curved flow, geostrophy is adequate in regimes of small to moderate Rossby number. To explore the appropriateness of geostrophic

balance, we use the values typical of the control run to calculate the Rossby number for the perturbation vortex. If 3.5 ms^{-1}, $8.4x10^{-5}$ s^{-1} and 600 km are used for U, f and L, respectively, the Rossby number (U/fL) is approximately 0.07.

2.2.4 Model Diagnostics

For all model simulations, a DRV will be characterized by its instantaneous growth rate and translation speed. In addition, to clarify the dynamical processes at work and building on the approach used by Parker and Thorpe (1995) and MM04, we will examine the energy conversion terms that constitute the RHS of the diagnostic eddy available potential energy (APE) equation:

$$\frac{\partial A_E}{\partial t} = C_A - C_E + G_E \tag{2.13a}$$

where A_E is the eddy APE, C_A the conversion from basic-state APE to A_E, C_E the conversion from A_E to eddy kinetic energy, and G_E the conversion from diabatic heat sources to A_E (Lorenz 1955). These terms are defined as follows:

$$A_E = \int_{p_1}^{p_2} \frac{\overline{[T']^2}}{2\bar{\sigma}} dp \tag{2.13b}$$

$$C_A = -\int_{p_1}^{p_2} \frac{\overline{[v'T']}}{\bar{\sigma}} \frac{\partial [T]}{\partial y} dp - \int_{p_1}^{p_2} \frac{\overline{[\omega'T']}}{\bar{\sigma}} \frac{\partial [T]}{\partial p} dp \tag{2.13c}$$

$$C_E = -\frac{1}{g} \int_{p_1}^{p_2} \frac{R}{p} \overline{[\omega'T']} dp \tag{2.13d}$$

$$G_E = \int_{p_1}^{p_2} \frac{\overline{[Q'T']}}{c_p \bar{\sigma}} dp \tag{2.13e}$$

$$\bar{\sigma} = \frac{1}{g} \left(\frac{[T]}{c_p} - \frac{p}{R} \frac{\partial [T]}{\partial p} \right) \tag{2.13f}$$

where $\overline{(\,)}$ represents a zonal average and $[\![(\,)]\!]$ an area mean (Muench 1965; Norquist et al. 1977). A prime indicates a deviation form a zonal average and an asterisk a deviation of a zonal average from the area mean. All variables have their usual meteorological meaning and $\overline{\sigma}$ represents the mean static stability.

The diabatic heating (Q) is computed using the residual method; that is, we calculate the terms on the RHS of the following equation,

$$Q=\left[\frac{\partial\theta}{\partial t}+\mathbf{V}\cdot\nabla_p\theta+\omega\frac{\partial\theta}{\partial p}\right]\cdot c_P\left(\frac{p}{p_o}\right)^{R/c_p} \tag{2.13g}$$

Before any of the above calculations are undertaken, the sigma level, MM5 output data is interpolated to constant pressure surfaces. Furthermore, since MM5 is a limited area model, both the zonal average and area mean calculations are, by definition, made over a limited area. This horizontal area of integration is time dependent, evolving with the disturbance field. As a general rule, the horizontal plane of integration is a box containing the low-level cyclonic circulation and the mid-tropospheric anti-cyclonic circulation that are characteristic of a DRV. For all cases, the vertical-pressure integral is evaluated from the surface to 250 mb.

The conversion ratio of the diabatic (G_E) to baroclinic (C_A) generation of eddy APE (hereafter referred to simply as 'the ratio') has been shown to be a useful diagnostic for differentiating between the dynamics associated with a long baroclinic wave and a DRV (Parker and Thorpe 1995; MM04).

$$CONVERSION\ \ RATIO=\frac{G_E}{C_A} \tag{2.13h}$$

The two-dimensional results of Parker and Thorpe (1995) and MM04 indicate that a conversion ratio much less than one is typical for a long baroclinic wave, whereas a conversion ratio larger than one is expected for a DRV.

2.2.5 Sensitivity Study

In addition to documenting the formation, structure and evolution of a DRV in a full-physics, 3D model, a sensitivity study is undertaken to better understand which parameters (both environmental and perturbation) play an important role in the DRV dynamics, and to quantify the effect of each parameter. The basic approach used in this study is to vary a single parameter of the initial condition, re-run the model and compare the results to those of the control run. In this way, insight can be gained into not only the physical processes at work, but also into the necessary information for an operational forecast model to properly forecast a DRV.

A full list of model runs is shows in Table 2.1. In summary, the sensitivity of DRVs to the environmental baroclinicity, the environmental moisture (in the form of the vertical profile of relative humidity), and the perturbation vortex size and strength is examined.

Experiment name	Baroclinicity Maximum Shear (ms^{-1} / km)	Moisture Level 1 (mb)	Moisture Level 2 (mb)	Initial Vortex 'Size' (km)	Initial Vortex 'Strength' (K)	Cumulus Parameterization	Horizontal Resolution (km)	Surface Fluxes	Surface Friction
Control	**1.5**	**800**	**600**	**300**	**3**	**Grell**	**90**	**Off**	**On**
B1	2								
B2	2.5								
B3	3								
M1		700	500						
M2		600	400						
M3		ERA RH data							
SI1				200					
SI2				400					
SI3				500					
ST1					2				
ST2					4				
ST3					5				
DRY						DRY			
NOSHEAR	0.0 ms^{-1} / km								
Appendix									
CUMPAR						Kain-Fritsch 2			
RES							30		
SFCFLX								On	
SFCFRIC									Off

Table 2.1 – Summary of MM5 numerical model simulations.

3. DRV Dynamics in a 2D, SG Model Framework

3.1 Moist Normal Mode Solutions

To explore the normal mode growth of the moist, Eady system, equation 2.5d for the moisture parameter [R(z)] is used, with R_o set to 0.01. A plot of growth rate as a function of nondimensional wavenumber is presented in Figure 3.1. Also included is the model and analytical solutions for R_o equal to 1.0 (the dry system). The latter information is included for comparison with the moist system.

Consistent with past research, diabatic effects on the unstable modes result in a shift of the most unstable mode and shortwave cutoff to shorter scales and increased growth rates. The dimensional wavelength of the most unstable, moist normal mode is 2565 km (nondimensional k = 2.45), indicating a reduction in wavelength of about 0.66 from the most unstable mode of the dry system. The growth rate of this mode (σ = 1.63 x 10^{-5} s^{-1}; e-folding time of 0.71 days) is approximately 1.75 times greater than that for the most unstable, dry normal mode. The shortwave cutoff of the moist system occurs at approximately 1365 km (nondimensional k = 4.6).

These findings compare well with those of JT, who found a scale contraction of 0.68 and an increase in maximum growth rate of approximately 1.9. The observed differences are likely the result of the increased vertical resolution used in these model runs (65 levels versus 40 for JT). In JT, the authors note as the vertical resolution in a multi-level model is reduced, the growth rate maximum is increased. Lower vertical resolution runs using the present model confirm this finding.

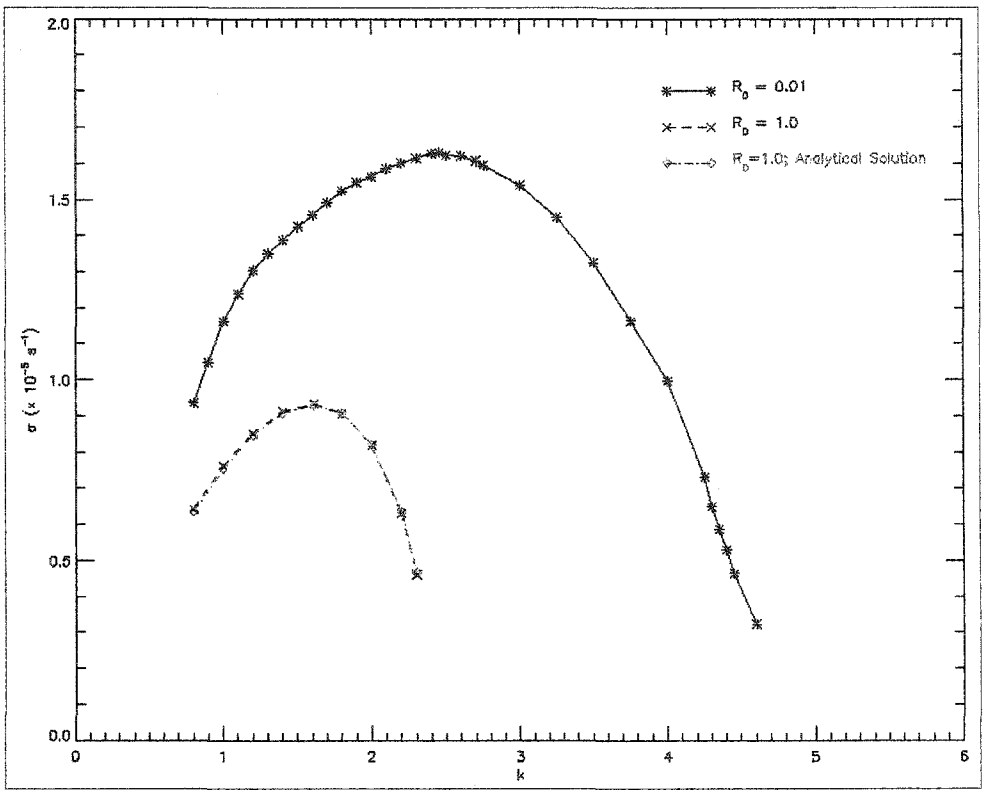

Figure 3.1 – Growth rate as a function of nondimensional wavenumber for a constant moisture parameter [$R(Z)=R_0=0.01$; black, solid line]. Model results for the dry problem ($R(Z)=R_0=1.0$; black, dashed line) and the analytical result (red, dashed-dotted line).

Figure 3.2 shows the temporal evolution of selected model fields of the most unstable mode. The mutual interaction between the upper- and lower-level disturbances results in a phase locked baroclinic wave that amplifies as it translates with the steering level flow. Baroclinic conversion of available potential energy to kinetic energy is occurring, as indicated by the westward tilt of the geostrophic meridional wind (v_g) with height.

Examination of right hand side of Equation 2.4a shows that for the dry system ($R_0 = 1.0$), PV cannot be created or destroyed. This is not the case for the moist system. If PV and w* are nonzero and vertically varying, PV will be either created or destroyed.

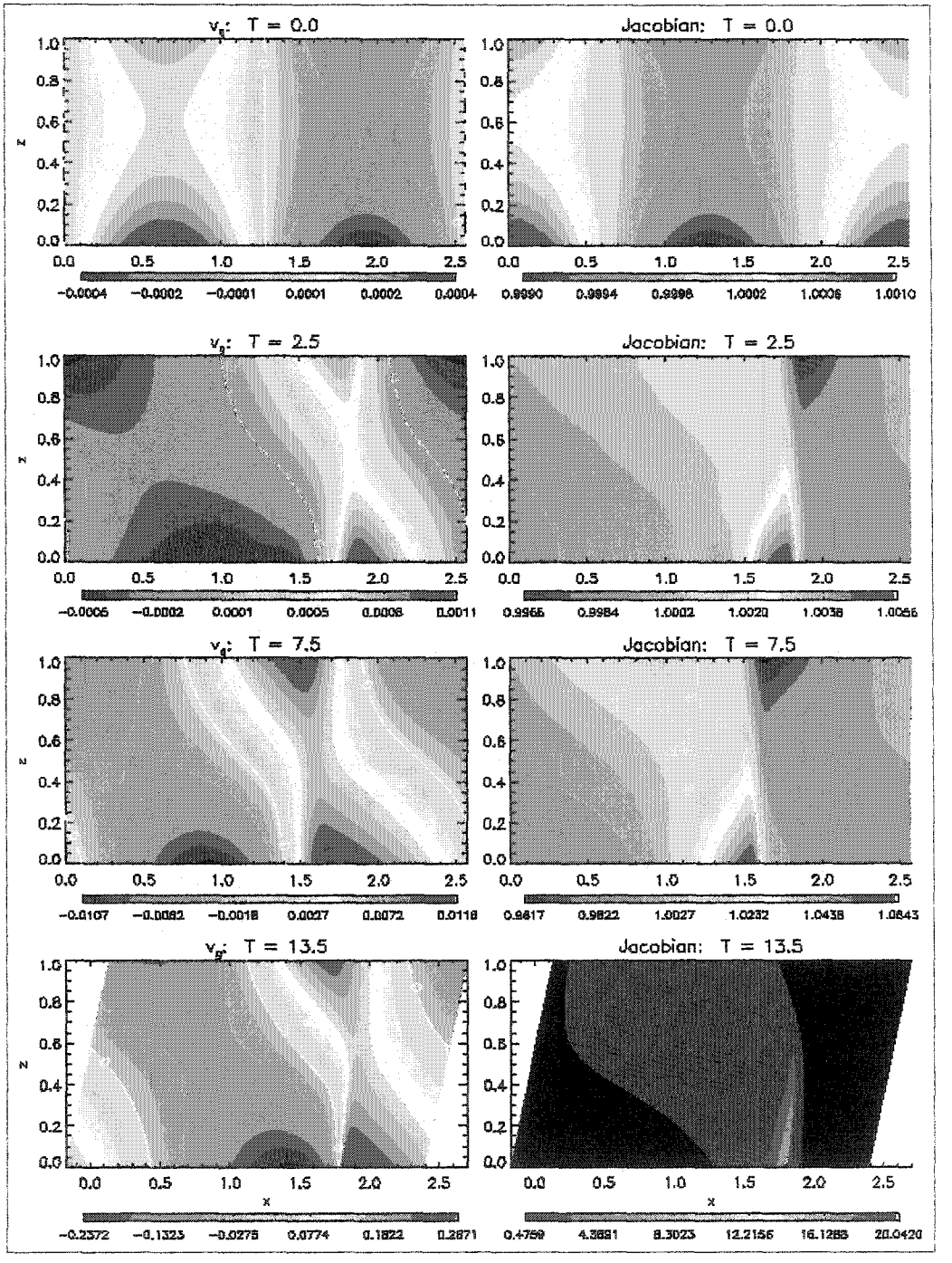

Figure 3.2(a) – The evolution of the most unstable, moist Eady normal mode with a zonal wavenumber of k = 2.45 (dimensional wavelength of 2,565 km). Shown are contour plots of the nondimensional v_g and Jacobian fields at T = 0, 2.5, 7.5 and 13.5 nondimensional advection times. Unit values of v_g and T correspond to 100 m s^{-1} and 9.25 hours, respectively.

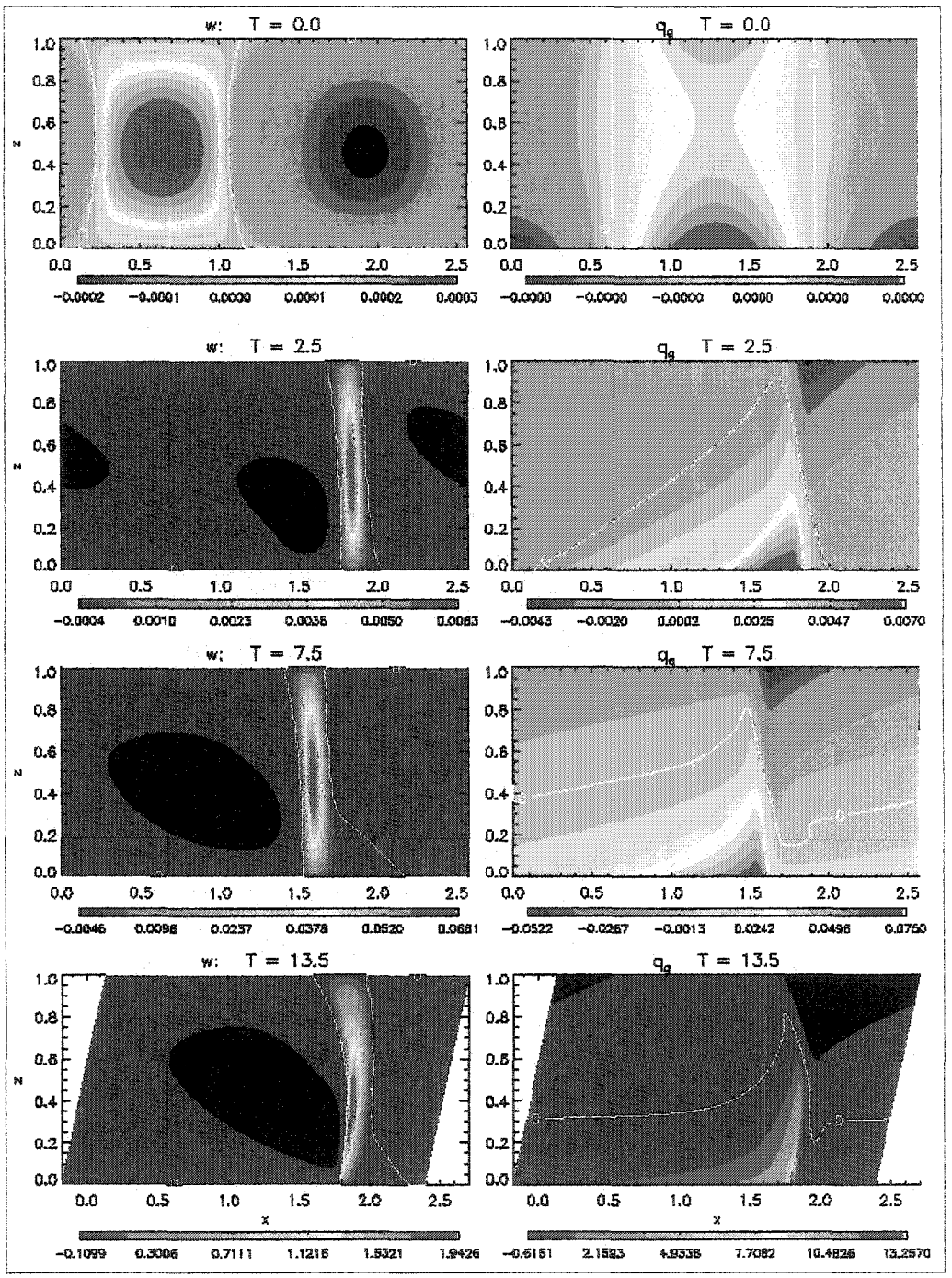

Figure 3.2(b) – The evolution of the most unstable, moist Eady normal mode with a zonal wavenumber of k = 2.45 (dimensional wavelength of 2,565 km). Shown are contour plots of the nondimensional vertical velocity (w) and anomalous dry potential vorticity (q_g) at T = 0, 2.5, 7.5 and 13.5 nondimensional advection times. A unit value of w corresponds to 30 cm s^{-1} and a unit value of corresponds to 10^{-4} s^{-2} [(≈1/4) PV units].

Early in the simulation, when PV is small compared to unity, the rate of induction of PV is largely controlled by the change of w* with height. In this regime, a positive (negative) induction of PV occurs when the vertical velocity is increasing (decreasing) with height. Since $\partial w^*/\partial Z$ is largest at $Z = 0$, the largest values of PV are observed at the surface. The result is a positive near-surface PV anomaly at the base of the updraft and negative PV maximum located on the upper boundary and slightly eastward of the positive anomaly. This dipolar structure of PV transports heat poleward with interaction of the induced anomalies enhancing the conversion of mean flow available potential energy to disturbance kinetic energy (MF91).

In contrast to the dry case (not shown), a pronounced reduction in scale of the cyclonic vorticity region is evident. Given sufficient time, the result is surface frontal collapse. The scale contraction is a consequence of the constraint of thermal wind balance, which requires strong updrafts below and downstream of the negative potential temperature disturbance at the tropopause. The only way this can be accomplished is by reducing the horizontal scale of the updraft region (MF91).

3.2 The Modified Moist System

Both EFT and JT used the EFT parameterization, in the form of a small but everywhere constant R, to diagnose the moist, normal modes of the Eady basic state. The emphasis of these studies was to determine the growth and evolution of the long baroclinic waves that result from the interaction of upper- and lower-level boundary anomalies.

More recent studies (e.g. MF91; Whitaker and Davis 1994) have noted the unrealistic nature of a moisture parameter that is constant with height. MF91 argued that,

since latent heating is proportional to the mixing ratio, the magnitude of latent heating should be much smaller at low temperatures than at high temperatures. Consequently, to more accurately represent an atmosphere in which the temperature decreases with height, the PV generation term on the RHS of the diagnostic PV equation (2.4a) should be smaller aloft than at the surface, given a similar vertical velocity field.

Following the method of MF91, (2.5d) is used to approximate this effect, with R_o set to 0.01. The result is a moisture parameter that increases linearly with height from 0.01 at the model surface to 1.0 at the model tropopause. The choice of a linear function of height is made to qualitatively mimic the nearly linear decrease of temperature with height in the troposphere. In the true atmosphere, the deviation from moist neutrality would be a more complex function of the local vertical profile of thermodynamic variables (such as temperature and moisture) that can and will vary in both space and time. However, the quasi-static approximation made here has been validated for short to moderate time integrations (MF91).

3.2.1 Growth Rates

The growth rate and real part of the phase speed in the small but finite amplitude regime for this modified moist system are presented in Figures 3.3 and 3.4, respectively. Also presented for comparison in Figure 3.3 are the results of the dry [$R(Z) = R_o = 1.0$] and small but constant R [$R(Z) = R_o = 0.01$] cases as well as the model solution for a system qualitatively similar to that of Whitaker and Davis (1994; hereafter WD94), who used a 2D, quasigeostrophic model with the EFT parameterization and a moisture parameter based on the local temperature and pressure (see their Figure 1).

Please note that, per convention, all figures of this type are plotted as a function of the initial nondimensional wavenumber (k; hereafter referred to as wavenumber). This must be explicitly stated because, in physical space (as opposed to geostrophic space), the

scale of a disturbance changes with time: a reduction in the scale of the cyclonic vorticity region is observed as wave amplitude increases.

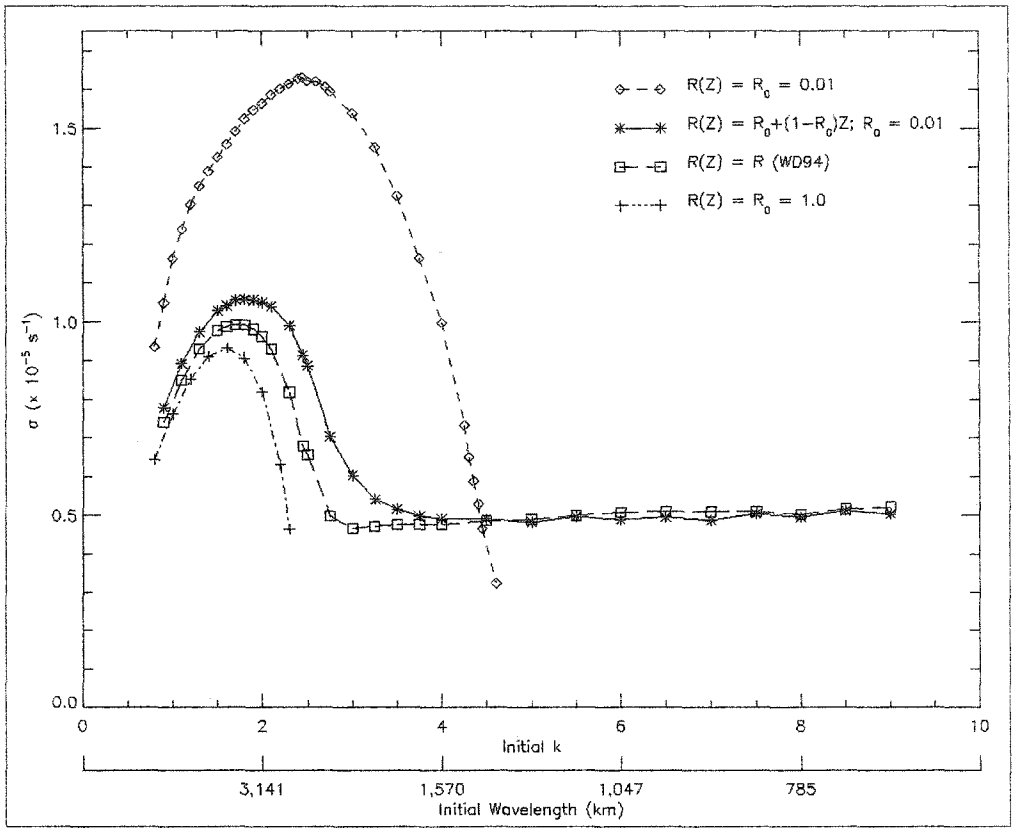

Figure 3.3 – Growth rate (σ; x 10^{-5} s^{-1}) as a function of initial nondimensional wavenumber and dimensional wavelength (km) for a small but constant moisture parameter [R(Z) = R_o = 0.01; ◊], a vertically varying moisture parameter [R(Z) = R_o+ (1-R_o)Z; R_o=0.01; *], the dry system [R(Z) = R_o = 1.0; +], and a system qualitatively similar to that of Whitaker and Davis [1994; □]. For reference, an e-folding time of one day corresponds to a value of σ = 1.157 x 10^{-5} s^{-1}.

In comparison with the small but constant R case, the more realistic approach results in: i) decreased growth rates, ii) a shift to longer scale of the most unstable mode, iii) the absence of a shortwave cutoff, iv) constant growth rates for zonal wavelengths less than approximately 1900 km, and v) a larger decrease in phase speed with decreasing characteristic zonal scale. The growth rate of the most unstable mode of the modified

moist system (1.058 x 10^{-5} s^{-1}; e-folding time of 1.09 days) is 1.14 times the dry value, with a zonal wavelength (3490 km) about 0.895 that of the most unstable, dry mode.

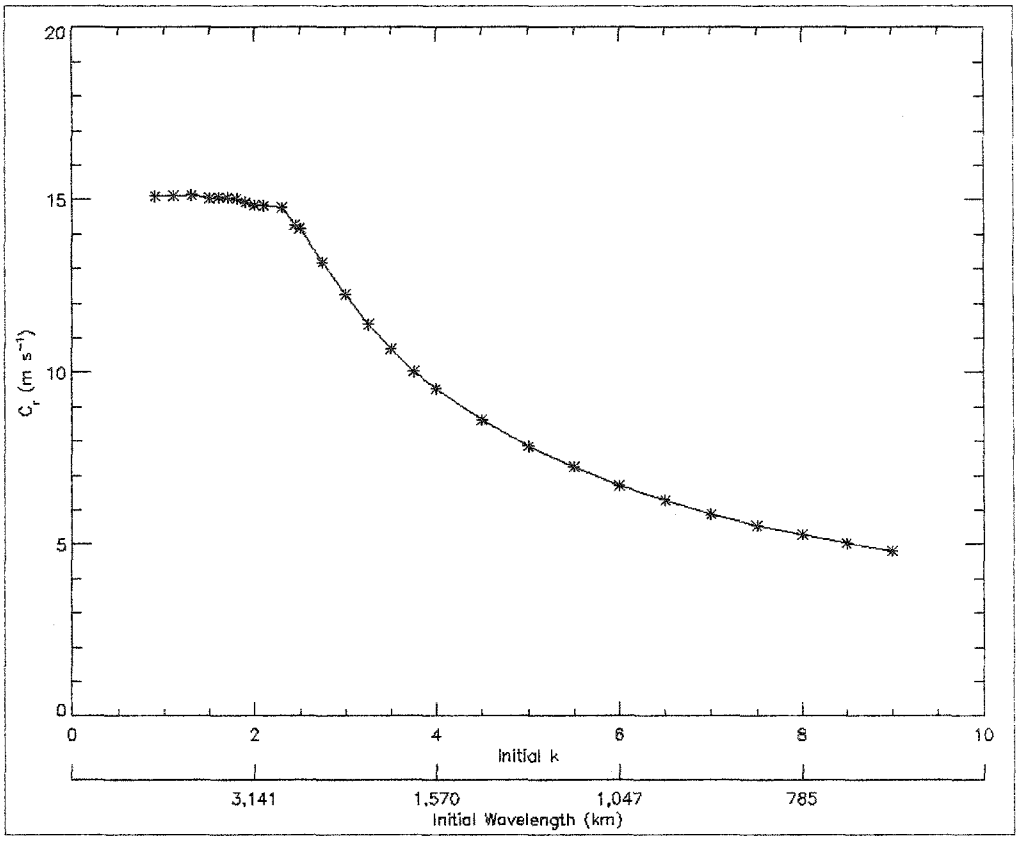

Figure 3.4 – The real part of the phase speed (C_r; ms^{-1}) as a function of initial nondimensional wavenumber and dimensional wavelength (km) for a vertically varying moisture parameter [$R(Z) = R_o + (1 - R_o)Z$; R_o=0.01; *].

Two growth regimes are evident in Figures 3.3 and 3.4, with a transition occurring at a zonal wavelength of approximately 1900 km (wavenumber = 3.25). For zonal scales longer than 1900 km, the growth rate curve qualitatively resembles that of the small but constant R case, and the phase speed shows little sensitivity to wave scale. These modes can be thought of as dry, long baroclinic waves whose structure and growth characteristics have been modified by diabatic effects. In contrast, waves with a characteristic zonal scale shorter than this value bear little resemblance to dry baroclinic

waves: growth rates are nearly constant with wavelength and the phase speed decreases sharply with decreasing scale. In Eady's classic 1949 paper, the author used the terminology of long waves and cyclone waves to differentiate between the characteristic scales of observed disturbances in the middle and high latitudes. While it is a departure from some more recent studies that have used the terminology long and short waves, we will hereafter adopt the convention of Eady (1949), referring to the long wave and cyclone wave regimes for dimensional zonal wavelength greater and less than 1900 km, respectively.

These findings verify, in a qualitative sense, those of WD94. Without explicitly stating the fact, they implied the existence of two growth regimes; however, they found the transition to be closer to a zonal wavelength of about 2700 km. As Figure 3.3 indicates, the predicted discrepancy between the two studies is solely due to differences in the vertical structure of R and, hence, the vertical parameterization of latent heat release. The moisture parameter incorporated by WD94 increases more quickly with height in the lower- to mid-levels of the atmosphere, resulting in: i) decreased growth rates in the long wave regime, and ii) a shift to longer scales of both the most unstable mode and the transition to flat growth.

However, it is apparent that regardless of the precise definition, the results with a vertically varying moisture parameter are quite robust in this model setting: as zonal wavelength decreases, there is a transition from long wave modes to a constant growth regime. As the remainder of this section will show, the short-scale modes are inherently different than the dry, long waves described by Eady (1949) as well as the moist long wave normal modes found by EFT and JT. They owe their existence to diabatic effects and are not dependent on an upper-level disturbance for wave amplification.

3.2.2 Disturbance Structure and Evolution

As an example of wave growth in the long wave regime, selected model fields for the most unstable mode of the modified moist system (k = 1.8; dimensional wavelength = 3490 km) are presented in Figure 3.5. Consistent with the dry and small but constant R cases (not shown), the mutual interaction between upper- and lower-level boundary disturbances results in a phase locked baroclinic wave that amplifies as it translates with the steering level flow. Baroclinic conversion of available potential energy to kinetic energy is occurring, as indicated by the westward and eastward tilt with height of the geostrophic meridional wind (v_g) and potential temperature, respectively.

When a more realistic vertical profile of latent heating in near neutral environments is used significant structural differences are predicted. In comparison with the small but constant R system: i) the pronounced reduction of the updraft width is significantly reduced (recall that updraft and downdraft widths are equal in the absence of moisture), ii) the disparity between the updraft and downdraft intensities is much less, and iii) the vertical velocity maximum is weaker.

An additional change to wave structure with far reaching consequences is predicted in the PV field. Mak (1994) noted the production of interior PV anomalies occurs in regions where a sharp vertical gradient in the heating rate exists. In the small but constant R case, PV generation is a maximum on the model boundaries. Not so in the modified moist system: due to the reduction of latent heating with height, the region of largest negative PV generation is displaced downward from the upper boundary. Specifically, the height of this region becomes a function of zonal wavelength, being lower in the atmosphere for shorter scales. We will soon see that it is this effect that allows for an alternative growth mechanism for scales shorter than the shortwave cutoff of the small but constant R system.

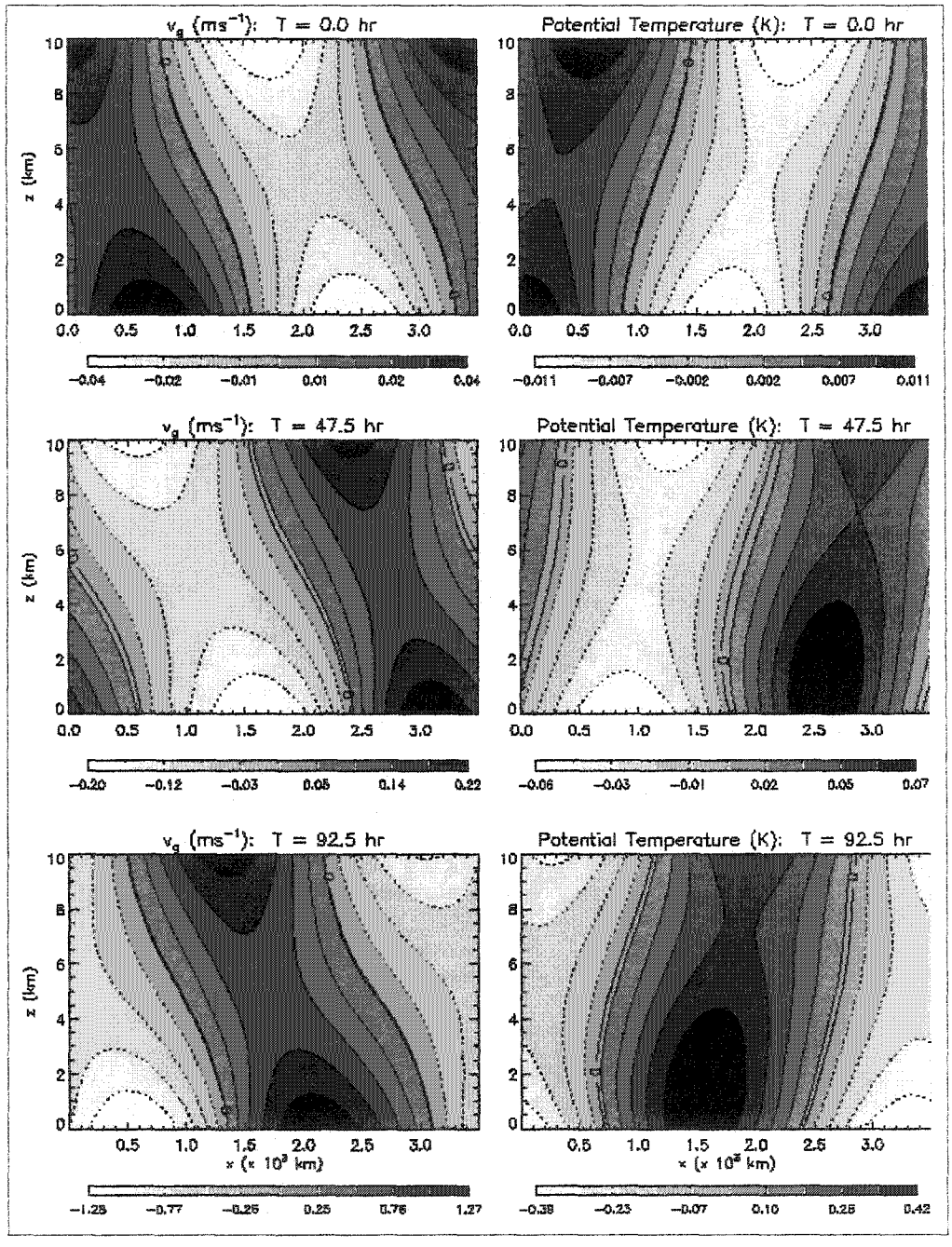

Figure 3.5(a) – The evolution of the most unstable, moist mode (initial nondimensional wavenumber k = 1.8; dimensional wavelength = 3490 km) for a vertically varying moisture parameter [$R(Z) = R_o + (1 - R_o)Z$; R_o=0.01]. Shown are the meridional wind (v_g; ms^{-1}) and the potential temperature perturbation at times (T) = 0.0, 47.5 and 92.5 hours.

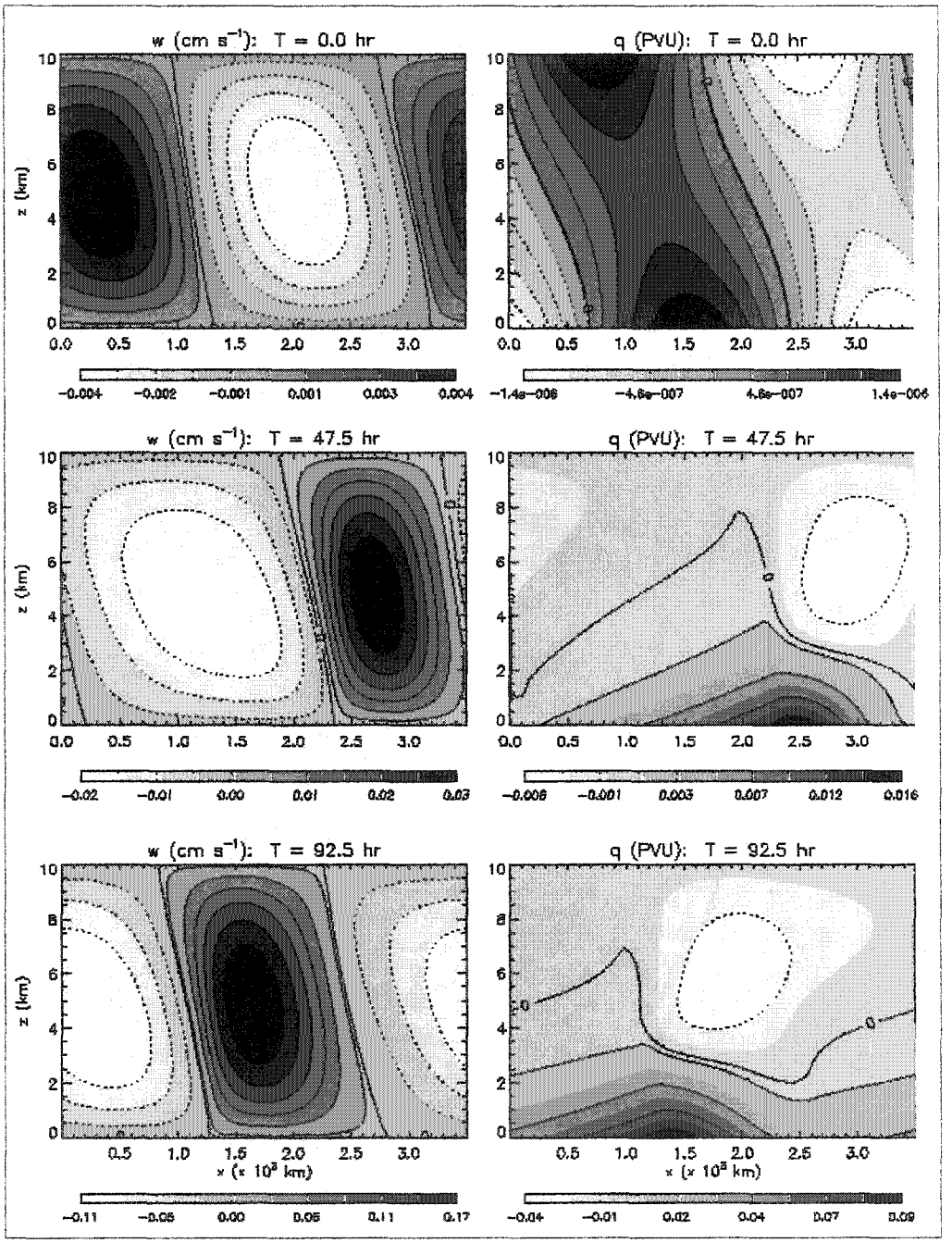

Figure 3.5(b) – Same as Fig. 3.5(a) except for the vertical velocity (w; cms^{-1}) and anomalous dry potential vorticity (q; PVU).

As an example of wave growth in the cyclone wave regime, the model results for a previously neutral wave in the moist system with a small but constant R (k = 6.0; dimensional wavelength = 1047 km) are presented in Figure 3.6. The surface concentrated nature of the wave is evident, as all significant wave dynamics are confined to the mid to lower troposphere. In contrast to the long wave regime, there is a distinct absence of secondary maximum of v_g and PT in the upper troposphere, indicating a lack of upper-level forcing.

Eady (1949) ascribed the growth of cyclone waves to the same physical processes as those of the dry, long wave modes. They were obtained using the same model results by substituting smaller values of the static stability and smaller vertical extents. Therefore, the structures of the long waves and cyclone waves were identical in this model formulation, with the exception of a significantly reduced scale (both in the horizontal and vertical) for the latter. The results presented in Figure 3.6, however, appear to rule out the traditional, dry baroclinic growth mechanism of the phase locking and mutual amplification of boundary PT anomalies. We believe that, in a moist baroclinic atmosphere, it is more relevant to think of cyclone wave growth in terms of diabatic processes (specifically the diabatic generation of PV associated with latent heat release) and, as we will see in the next subsection, the energetics of the disturbance.

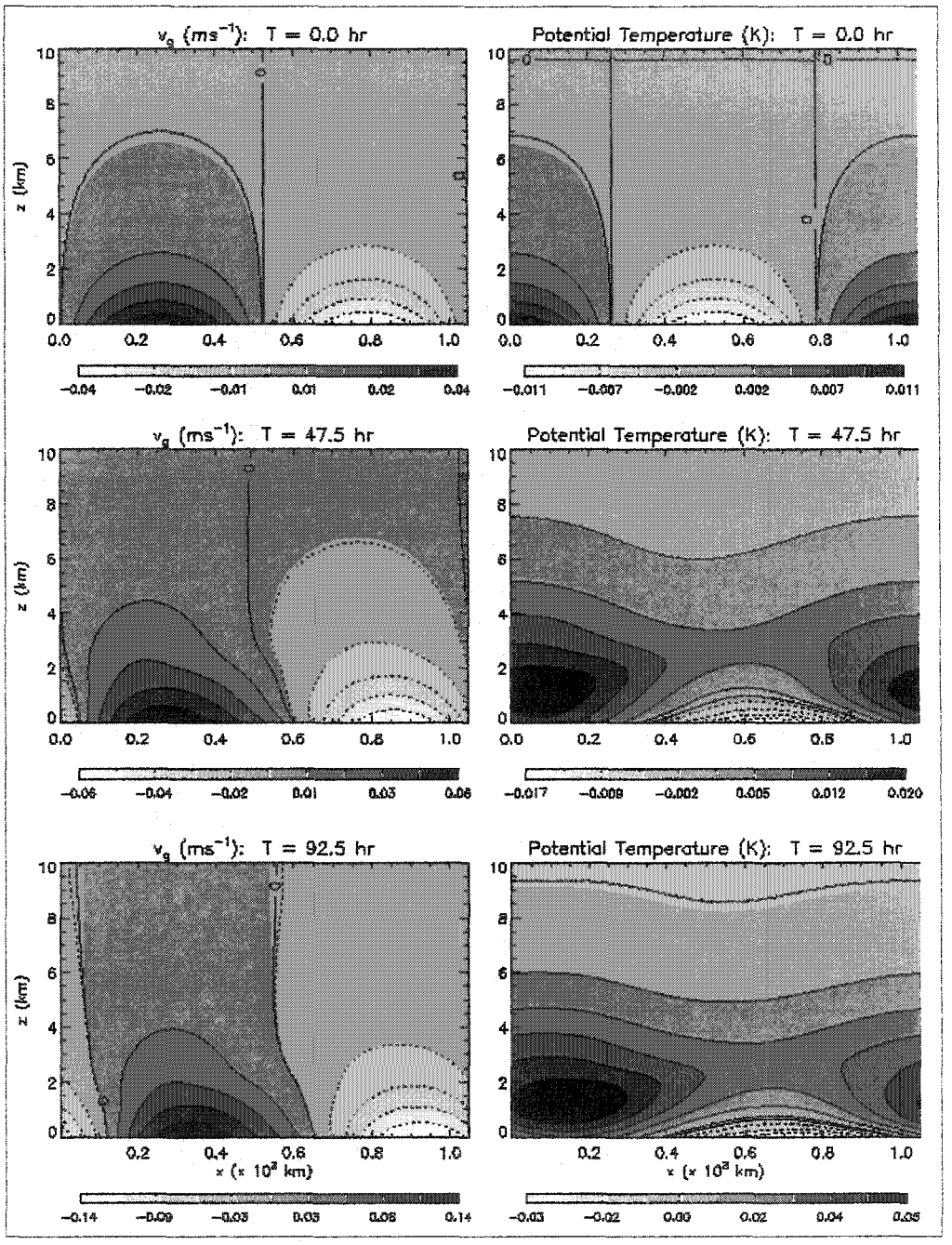

Figure 3.6(a) – Same as Fig 3.5(a) except for a previously neutral wave (initial nondimensional wavenumber k = 6.0; dimensional wavelength = 1047 km).

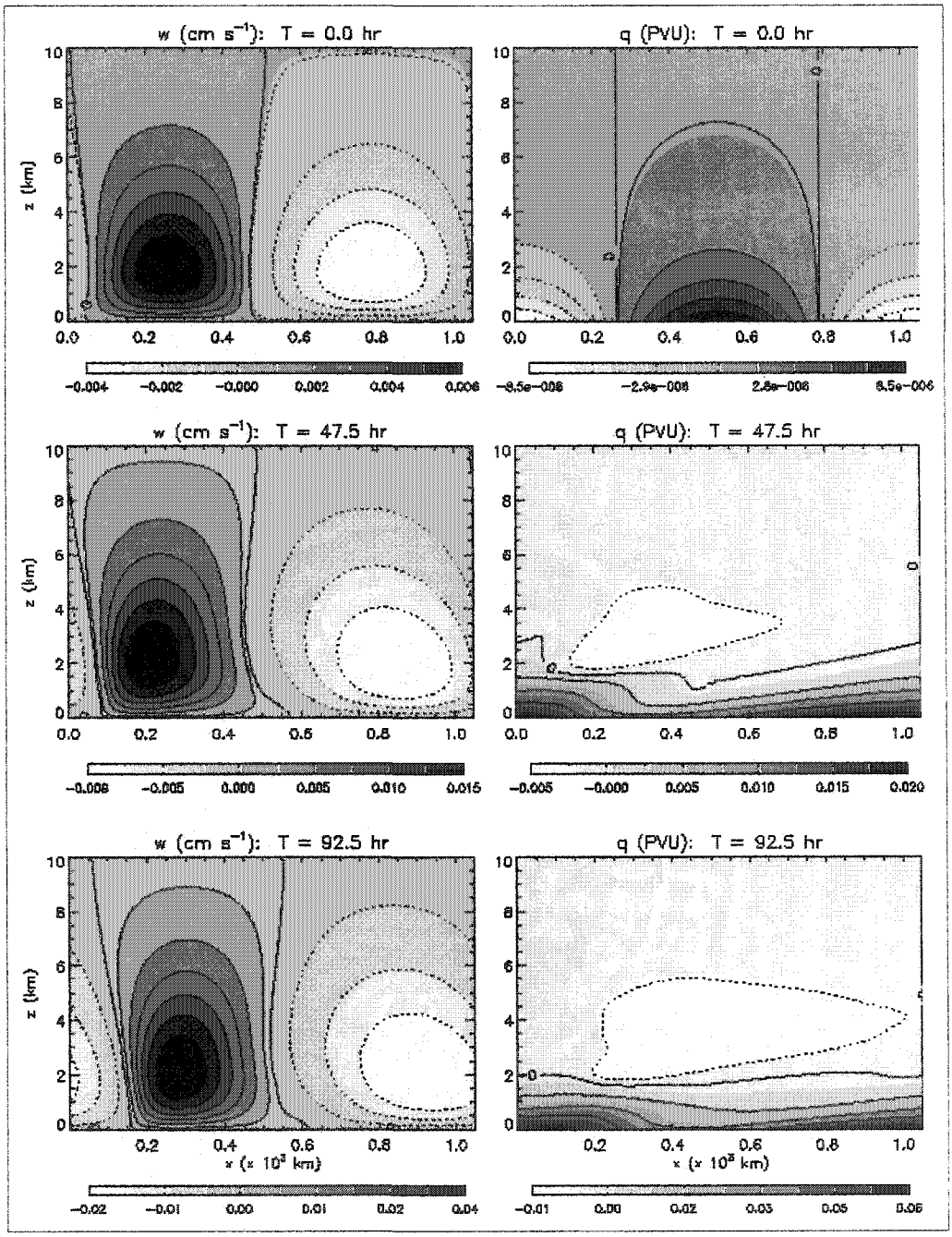

Figure 3.6(b) – Same as Fig 3.5(b) except for a previously neutral wave (initial nondimensional wavenumber k = 6.0; dimensional wavelength = 1047 km).

3.2.3 Growth Mechanisms and Energetics

As one way to clarify the growth characteristics of the modified moist system, the energy conversion terms that constitute the RHS of the diagnostic eddy available potential energy (APE) equation are calculated. Following Parker and Thorpe (1995; hereafter PT95), for a two-dimensional system, they can be expressed as

$$GE = \frac{g}{2\theta_0 \overline{\theta_z}} \overline{(\theta' S')} \tag{3.1a}$$

$$CE = -\frac{g}{2\theta_0} \overline{(w'\theta')} \tag{3.1b}$$

$$CA = \frac{f \overline{U_z}}{2\overline{\theta_z}} \overline{(v_g'\theta')} \tag{3.1c}$$

where S is diabatic heating, GE is the conversion from diabatic heat sources, CA is the conversion from basic-state APE, and CE is the conversion from eddy APE to eddy kinetic energy. An overbar within a parentheses represents a spatially integrated quantity.

To investigate the relative effects of diabatic and baroclinic processes on wave growth, the ratio of GE to CA as a function of wavenumber (dimensional wavelength) is presented in Figure 3.7. It is evident that the production of eddy APE by diabatic processes becomes increasingly important with decreasing zonal wavelength. In fact, while significant baroclinic production of eddy APE is predicted in the long wave regime, diabatic production begins to dominate as the characteristic zonal scale decreases.

The results contained in Figures 3.3-3.7 provide the necessary clues to help explain the existence of two growth regimes. As in the dry and small but constant R cases, the long wave modes grow as a result of the mutual interaction of surface and tropopause PT anomalies and the baroclinic production of eddy APE is of order one importance. However, with the downward displacement of the largest negative PV

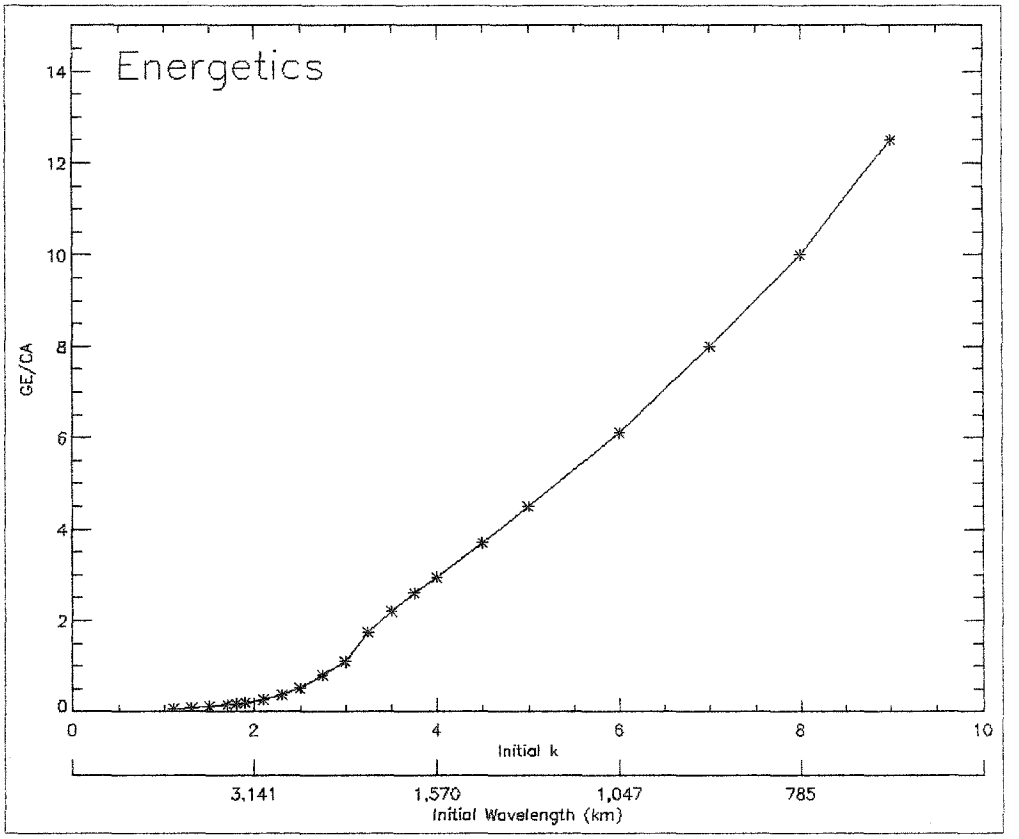

Figure 3.7 – Ratio of the conversion of diabatic heat sources to eddy APE (GE) over the conversion of basic state APE to eddy APE (CA) as a function of initial nondimensional wavenumber and dimensional wavelength (km) for a vertically varying moisture parameter [$R(Z) = R_o + (1 - R_o)Z$; $R_o = 0.01$; *].

generation from the upper boundary, the disturbance is less efficient at converting mean flow potential to kinetic energy, and the characteristic zonal scale at which this process is most efficient has shifted to longer wavelengths (as indicated in Figure 3.3).

As previously stated, a different growth mechanism is at work in the cyclone wave regime. These modes owe their existence to diabatic effects: exponential growth is due to the interaction of a diabatically-generated interior PV anomaly and a surface PT anomaly (WD94). No upper boundary disturbance is necessary for growth (MF91; Mak

1998). These modes exhibit the behavior of a diabatic Rossby wave (Raymond and Jiang 1990; Snyder and Lindzen 1991; Parker and Thorpe 1995), a topic that will be further explored in Section 5.

The latter growth mechanism accounts for the lack of a shortwave cutoff in the modified moist system. When the diabatically-generated PV anomalies are forced to be on the upper and lower model boundaries, as is the case when R is constant with height, there has to be a cutoff wavelength where the penetration depth of these boundary anomalies is no longer large enough to allow phase locking and mutual amplification.

In the modified moist system, this inherent problem is circumvented. As a result of the scale dependence of the region of largest negative PV generation, the penetration depths of the interior, diabatically-generated PV anomaly and the surface PT anomaly are always large enough to allow a mutual interaction, and exponential growth is observed for all wavelengths.

To account for constant growth in the cyclone wave regime, one must further explore the effect of the vertical structure of heating. It has been demonstrated previously that the dynamic response of a tropical or extratropical vortex to a diabatic heat source is strongly dependent on the vertical structure of the heat source (Hack and Schubert, 1986; Craig and Cho, 1988). While it is clear from Figure 3.7 that the conversion of diabatic heat sources becomes dominant in the cyclone wave regime, what is not apparent is that the diabatic generation of eddy APE becomes nearly constant with wavelength. Since in this model framework a decrease in zonal wavelength is synonymous with a lowering of the maximum heating level, the implication is that a disturbance becomes more efficient at converting diabatic heat sources to eddy APE when the level of maximum heating occurs lower in the atmosphere. Therefore, even though significant heating is occurring over a smaller spatial area, the increased

efficiency provides the requisite reservoir of eddy APE (that is subsequently converted to eddy kinetic energy) to support a constant growth rate over these zonal scales.

Finally, it is important to note that in this model setting the preferred 'final' scale of the disturbance is controlled by the horizontal scale of the initial condition. Due to the linear nature of the moisture parameter, there is no environmentally preferred region of a sharp vertical gradient in the heating rate and diabatic PV production (Mak 1994); it is the structure of the initial disturbance (specifically, the initial vertical velocity and PV fields) that 'creates' a vertical gradient in the heating rate, diabatic PV production, and the resulting scale of the ensuing disturbance. In the true moist atmosphere, a sharp vertical gradient in the heating rate and, hence, the preferred 'final' scale of the disturbance field, can be created by such factors as moisture stratification (Fantini and Buzzi 1994 and 1997; Mak 1994; Fantini 1995), the variation of the static stability with height (Mak 1998) or, if the disturbance is a remnant of some previous development (e.g. an extratropically transitioning tropical cyclone), by the scale of the previous disturbance.

3.3 Finite Amplitude Growth

In their 1994 paper on cyclogenesis, WD94 used 3D, nonlinear primitive equation simulations to explore wave growth at finite amplitude. They found that, while dry waves continue to grow at nearly the linear growth rate, moist waves grow significantly faster at finite amplitude. At a certain point in the lifecycle of a cyclone, WD94 identified a reduction of the moist static stability in the region of the warm front, due to moisture advection, that facilitated a rapid amplification of a mesoscale PV anomaly generated by latent heat release. They concluded it is the superposition of the circulation associated with this feature upon the circulation associated with the surface

and upper boundary potential temperature anomalies responsible for the 'burst' of growth observed in their study

To examine the exponential growth in the nonlinear regime, we restrict our attention here to the simplified, 2D model. The model is initialized as in Section 4 and the integration is continued for longer times than in Section 4.

In the absence of moisture effects, a single unstable mode is an exact solution to the 2D nonlinear equations. Dry model runs (not shown) confirm growth rates are invariant at finite amplitude. This is not the case, however, for the moist system. Growth rates are found generally to be a function of both wave amplitude and scale in the nonlinear regime.

The growth rate spectrum for numerous wave amplitudes, as defined by the maximum geostrophic, meridional wind at the surface (v_{gmax}), is presented in Figure 3.8. Again, two regimes of growth are evident. Qualitatively, growth rates increase (decrease) with increased wave amplitude for waves longer (shorter) than approximately 1900 km; however, even within these two regimes, a scale-dependence is observed.

To facilitate interpretation, the normalized change of growth rate is calculated as follows,

$$\sigma_{\text{Normalized}} = \frac{\left(\sigma_{\text{Nonlinear}} - \sigma_{\text{Linear}}\right)}{\sigma_{\text{Linear}}} \tag{3.2}$$

and is plotted as a function of v_{gmax} (not shown). For a given scale, there is a nearly linear relationship between the two variables. For waves longer than about 1900 km, the increase of $\sigma_{\text{Normalized}}$ with increasing v_{gmax} becomes smaller as wavelength becomes larger, resulting in the most unstable mode being shifted to a slightly shorter wavelength. This finding is consistent with the idea that the effect of moisture is to shift growth to smaller scales.

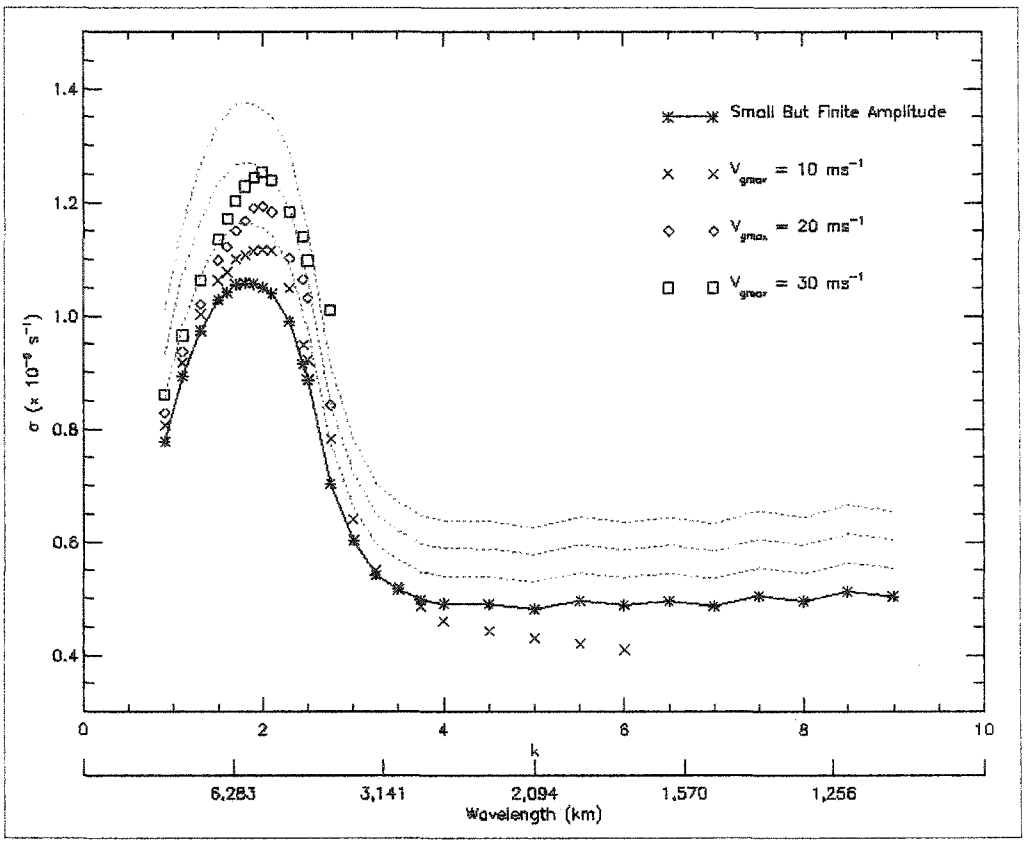

Figure 3.8 – Growth rate (x 10^{-5} s^{-1}) as a function of nondimensional wavenumber and dimensional wavelength (km) for a vertically varying moisture parameter [$R(Z) = R_o + (1-R_o)Z$; R_o=0.01] for various wave amplitudes as measured by the maximum meridional wind at the surface (v_{gmax}). Dashed lines indicate a 10, 20 and 30 percent increase from the small but finite amplitude results.

In contrast, for waves shorter than approximately 1900 km, the decrease of $\sigma_{Normalized}$ with v_{gmax} becomes smaller as wavelength becomes larger. This can be best understood by considering the efficiency with which the wave converts mean flow available potential energy to disturbance kinetic energy in the context of a temporally varying Rossby penetration depth. When the PV approaches O(1), the scaled Rossby penetration depth can be expressed as

$$R_d = k^{-1}(1+q)^{-1/2} \tag{3.3}$$

Equation 3.3 predicts that, for the same characteristic zonal scale, the penetration depth will tend to be reduced in regions where PV is positive and decreased where PV is negative. Due to the square root dependence on PV, however, the penetrations depth is still predominantly controlled by the zonal wavenumber (MF91).

As wave amplitude grows with time, so does the absolute magnitude of PV. However, for a given increase of wave amplitude, the fractional increase in PV is larger for shorter scales. Recall that, as wavelength is decreased in the modified moist system, the physical depth of the wave decreases. Since PV production is dependent on the vertical gradient of heating (see Equation 2.4a), this effect enhances the production of PV as a wave becomes more shallow with decreasing zonal scale. Returning to 3.3, the characteristic variability of PV production with zonal scale implies a larger relative decrease in penetration depth for shorter waves. The overall effect is to decrease the efficiency with which shorter waves convert available potential energy to kinetic energy, as confirmed by the explicit calculation of the baroclinic conversion rate (not shown).

To address the issue of a time invariant moisture parameter, model simulations are conducted in which local advection of this parameter is allowed to take place. At small amplitude, wave growth and structure remain nearly identical. At finite amplitude, allowing advection of the moisture parameter provides a small boost to wave growth. The enhanced growth is not as large as found by WD94, most likely due to the two-dimensionality of the present model. The process as observed in WD94 involves the alignment of features in three dimensions. However, consistent with the results of WD94, advection of unstable air by the zonal wind reduces the static stability in the region of ascent (see Figure 3.9), thereby increasing the intensity of the vertical velocity, latent heat release and wave growth.

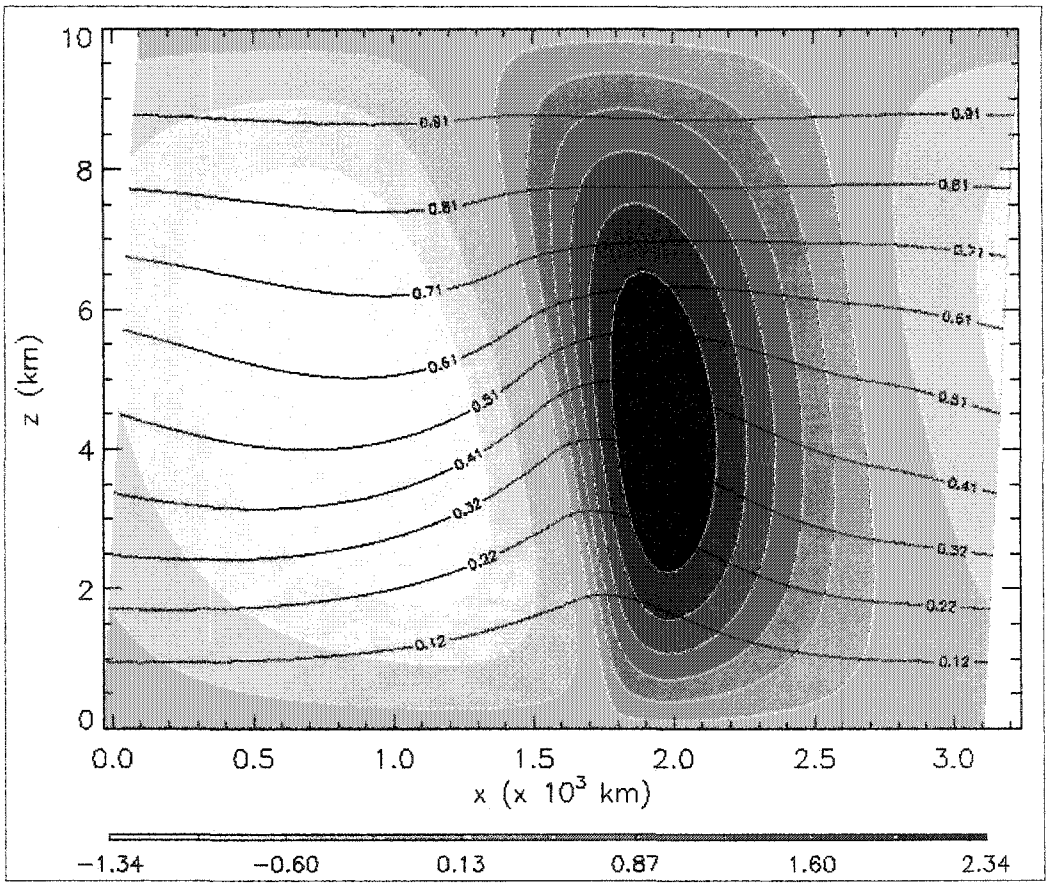

Figure 3.9 – Spatial distribution of the vertical velocity (cm s^{-1}; shaded) and moisture parameter, R, (overlaid contours) for a nondimensional wavenumber k=2.0 (dimensional wavelength = 3141 km) disturbance at nondimensional time T=11.0 hours.

3.3 The Influence of Surface Friction

Figure 3.3 clearly shows that, in the absence of friction, significant growth is expected for wave scales much shorter than the most unstable mode of the modified moist system. However, to ascertain the practical importance of these short-scale,

diabatic normal modes, we must examine the influence of frictional damping on wave growth.

There has been a debate in the literature as to what degree surface friction inhibits baroclinic wave growth. Farrell (1984, 1985, 1989) explored the effect of Ekman friction in both the Eady and Charney models of baroclinic instability. He found that, even when moderate values of the kinematic eddy viscosity are used [$\nu = 2.5\ m^2s^{-1}$; see Fig, 4 of Farrell (1985)], Ekman damping significantly limits the range of unstable wavenumbers and reduces the growth rate of the remaining instabilities.

In their 1988 manuscript, Lin and Pierrehumbert qualify the findings of Farrell (1985) when they state: "Farrell's results are not definitive, however, because he computed the stabilization threshold for only a single channel width and zonal wavenumber", noting that the choice of channel width is crucial. Given this fact, they chose to examine the problem with a one-dimensional model with various channel widths and values of Ekman damping, and a 2D model with varying values of shear parameter and Ekman damping. The study concluded that Ekman friction almost certainly cannot eliminate baroclinic instability in the oceanic storm tracks. For values of dissipation deemed realistic for the atmosphere (as calculated by their boundary layer model, they judged $\nu = 3.6\ m^2s^{-1}$ to be representative of the real atmosphere over the ocean), they concluded the e-folding time and wavelength of the most unstable mode is consistent with observations of synoptic cyclones.

Other investigators agree with this assessment. Valdes and Hoskins (1988) used a hemispheric, spectral, primitive equation model to show that the zonally averaged atmosphere is baroclinically unstable, even in the presence of reasonable boundary layer friction. Additionally, Rotunno and Bao (1996) note that, while it is an important factor at large amplitude, Ekman friction plays only a minor role in the early stages of development.

3.3.1 Ekman Pumping

To investigate the effect of surface dissipation on the moist dynamics of our 2D model, Ekman pumping is introduced to parameterize the effect of the planetary boundary layer. Ekman pumping is defined as the curl of the surface stress (Fleagle and Nuss 1985),

$$w_E = \left(\frac{1}{\rho f}\right)\nabla \times \tau_S \cdot \hat{k} \quad \text{on Z=0} \tag{3.4}$$

The bulk aerodynamic formula for the surface stress (τ_S) is:

$$\tau_S = \rho C_D |v| v \tag{3.5}$$

where C_D is the drag coefficient. This formulation of Ekman pumping is valid when the curl of the surface stress is large and advection and local change can be neglected (Bond and Fleagle, 1985).

This method for estimating the vertical velocity at the top of the boundary layer has been validated with observations. Bond and Fleagle (1985) noted that frictional convergence accounted for nearly the entire updraught mass flux for two cold fronts over land. Furthermore, Wakimoto and Cai (2002; Section 4, p. 1903) calculated Ekman pumping in such a manner and found the vertical velocities to be close to values obtained using dual-Doppler radar observations.

For wind speeds between 10 and 25 ms^{-1}, an equation for C_D for neutral stability over the ocean was derived from empirical data by Large and Pond (1982),

$$C_D = (0.49 + 0.065|V|) \times 10^{-3} \tag{3.6}$$

giving a range of $1.14 - 2.12 \times 10^{-3}$. For values of $|V|$ between 3 m s^{-1} and 10 m s^{-1}, C_D was estimated at 1.14×10^{-3}.

3.3.2 Quadratic vs. Linear Surface Drag

In contrast to many studies, we represent the surface stress with a quadratic (as opposed to linear) dependence on surface wind speed. The use of linear surface drag is somewhat ill posed in the sense that the boundary layer is, in general, turbulent. While, in this case, we are not interested in the structure of the boundary layer per se, the choice of the form of the surface stress does have far reaching consequences and therefore must be considered carefully.

A common approach used to simplify the system is to linearize (3.5) around an average value of the surface wind speed (u_{av}), and subsequently to equate the lower boundary condition for the quadratic and linear surface drag cases (Gill 1982; p. 332), giving

$$\left(\frac{\nu f}{2}\right)^{\frac{1}{2}} \approx 2C_D u_{av} \tag{3.7}$$

where ν is the kinematic eddy viscosity. In this way, one can estimate ν, in terms of the parameters describing the structure of the turbulence in the boundary layer and the momentum exchange with the underlying surface.

The kinematic eddy viscosity is an explicit function of the drag coefficient and is implicitly dependent on wave amplitude [via the dependence on u_{av} in 3.7)]. For this approach to be consistent, it is necessary to allow ν to change with these variables, something that is not typically done.

When studying problems where u_{av} is not changing drastically, say in the case of a linear stability analysis, the problem is in principle a minor one. The choice of a constant value for u_{av}, however, is problematic when the magnitude is highly variable, as it would be in practice as in the case of the lifecycle of an extratropical cyclone. Rotunno and Bao (1996) speak to this problem when they note that the saturation amplitude for

wave growth is much larger without the nonlinear feedback of the quadratic surface stress.

Since it is our goal to characterize wave growth over a relatively large range of wave amplitudes (0-30 ms^{-1}), we believe the quadratic form of surface stress is the appropriate choice. To address the foreseeable objection that a quadratic form of the surface stress is inappropriate in the small but finite amplitude regime, we have configured the model to incorporate linear drag as well. An appropriate value of ν is approximated by (3.7): assuming a value of 1.14×10^{-3} for C_D (Large and Pond 1982) and a range of 0-4 ms^{-1} for u_{av} in the small but finite amplitude regime, an average value of 0.6 m^2s^{-1} is obtained. As anticipated, the linear drag results with this value of ν (not shown) are consistent with those presented below for quadratic drag.

3.3.3 Results with Quadratic Drag

Using (2.5d) for the moisture parameter (R_o=0.01), the response of the system to quadratic surface drag is examined over a range of drag coefficients, ranging from values representative of smooth sea surface ($C_D = 1 \times 10^{-3}$) to rough terrain ($C_D = 4 \times 10^{-3}$) (Fantini and Buzzi 1997). For these model runs, the drag coefficient is set to a constant value and is not allowed to vary with time or wave amplitude. While (3.6) clearly shows C_D should not be considered constant, the same equation also indicates the variability of C_D, for a given surface type, is fairly small over a reasonable range of wind speeds.

Figure 3.10 presents the growth rate spectrum of small but finite amplitude disturbances when quadratic surface drag is included. Qualitatively, the effect of frictional damping is to reduce wave growth for all scales and, as a result of frictional dissipation working more efficiently on smaller scales, a small shift of the most unstable mode to longer scales is anticipated.

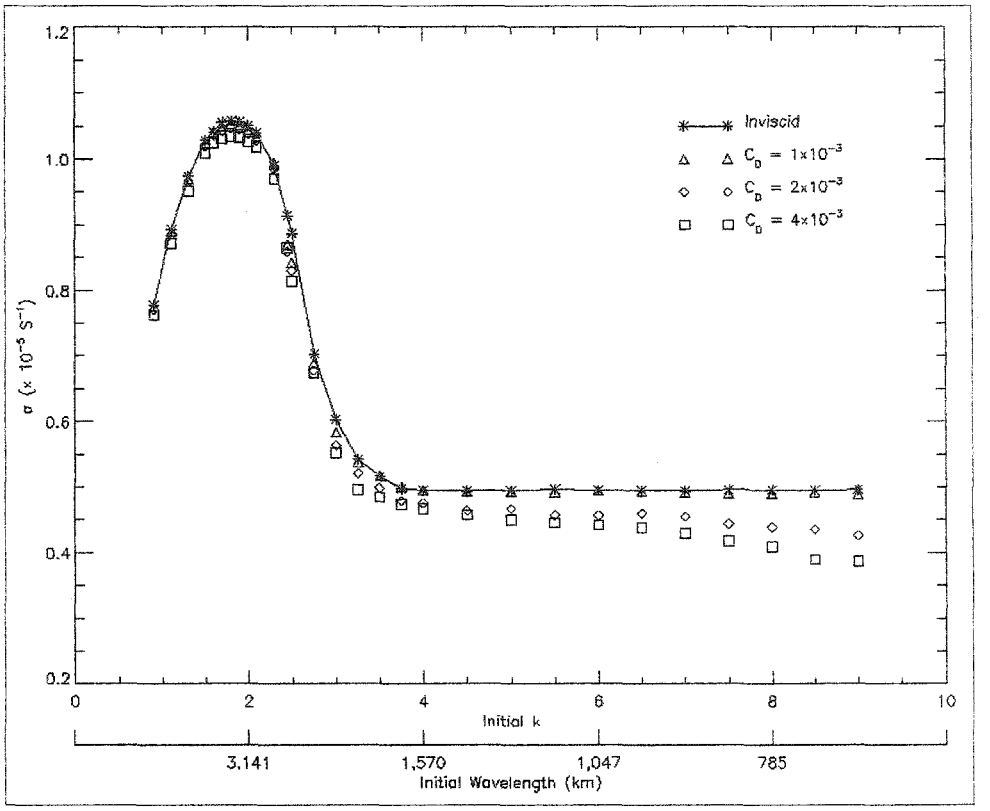

Figure 3.10 – Growth rate (σ; x 10^{-5} s^{-1}) as a function of initial nondimensional wavenumber and dimensional wavelength (km) for a vertically varying moisture parameter [$R(Z) = R_o + (1- R_o)Z$; R_o=0.01] with quadratic surface drag for the following values of the drag coefficient (C_D): 1 x 10^{-3} (Δ), 2 x 10^{-3} ($\Diamond$) and 4 x 10^{-3} ($\Box$). The inviscid case (solid line; *) is also shown.

It is evident, however, that the reduction of the disturbance growth rate is quite small. The implications of this result are noteworthy: not only does it extend to the moist atmosphere the finding of Rotunno and Bao (1996) that Ekman friction plays a minor role in the early stages of cyclogenesis, but it suggests that significant growth can occur at relatively small scales (dimensional wavelength $\leq$ 1000 km).

To explore the effect of frictional damping in the nonlinear regime over an ocean surface, (3.6) is used to define a temporally-varying C_D and model integration is continued for longer times. Figure 3.11 presents the instantaneous growth rate for

numerous wave amplitudes (using the maximum, surface meridional wind speed as a proxy for wave amplitude).

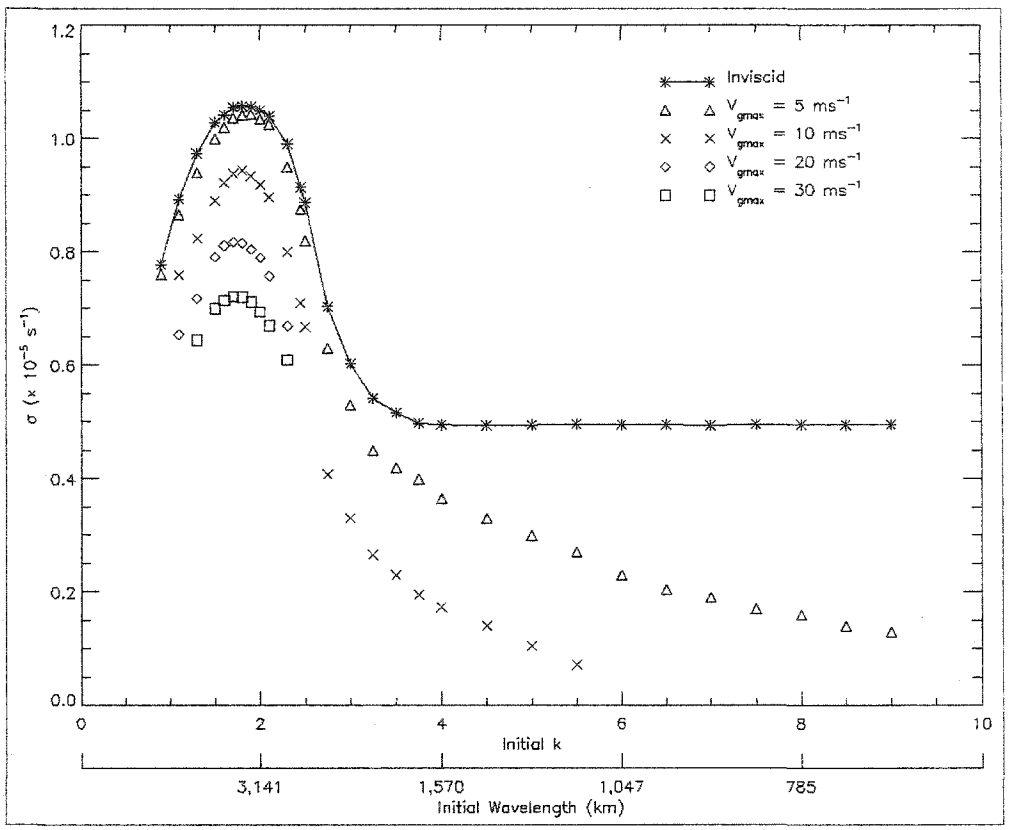

Figure 3.11 – Growth rate (σ; x 10^{-5} s^{-1}) as a function of initial nondimensional wavenumber and dimensional wavelength (km) for a vertically varying moisture parameter [$R(Z) = R_o + (1 - R_o)Z$; R_o=0.01] with quadratic surface drag and a temporally-varying drag coefficient (C_D) defined by Equation 3.6 for various wave amplitudes as measured by the maximum meridional wind at the surface (v_{gmax}).

As wave amplitude grows with time, quadratic surface drag becomes more efficient at reducing disturbance growth over all scales and has a larger relative effect on smaller scales (as was seen in Figure 3.10). However, it is clear that exponential growth in the long wave regime is predicted in the presence of realistic surface friction (even with maximum near surface winds on the order of 30 m s^{-1}), confirming the finding of

Lin and Pierrehumbert (1988) that it is extremely unlikely Ekman friction can eliminate baroclinic instability in the oceanic storm tracks.

For any specific wavelength in the cyclone wave regime, an examination of the temporal evolution of the instantaneous disturbance growth rate (not shown) demonstrates that disturbance growth converges to zero (i.e. no growth or decay) with increasing wave amplitude. This illustrates that, while the maximum disturbance amplitude is limited by frictional dissipation, disturbances in the cyclone wave regime, once generated, do persist.

Furthermore, it is possible that there is an underestimation of nonlinear growth in this model setting. Hack and Schubert (1986) demonstrate that as the intertial stability of an axisymetric vortex increases with disturbance amplitude, the efficiency with which the vortex converts potential energy to kinetic energy increases. This effect produces a dramatic pressure drop in their model results (see their Fig. 1). While their model was formulated for the study of tropical cyclones, we believe it quite possible that the same effect may play a primary role in the rapid deepening of explosive extratropical cyclones. Unfortunately, this effect is not quantitatively captured in the present model formulation. The inertial stability of an atmospheric vortex is much larger in a model system invoking circular symmetry and including curvature effects. The neglect of curvature effects is a shortcoming of the 2D, SG model used in this study.

Another shortcoming of the 2D, SG model is the presence of unlimited APE (due to the time invariant meridional temperature gradient of the basic state). In the true atmosphere, APE is converted to eddy kinetic energy, thereby reducing the supply of APE and limiting disturbance growth.

Even without an increase in disturbance growth, the results of this section demonstrate that it is possible for short-scale disturbances to form and persist in the presence of 'realistic' quadratic surface drag. Given this fact, we believe that these short-

scale, diabatic modes are a likely candidate for the antecedent, low-level disturbances previously identified in studies of explosive cyclogenesis (Bosart 1981; Gyakum 1983 and 1991; Gyakum et al. 1992; Uccellini 1986).

3.4 The Diabatic Rossby Vortex

The notion of a diabatic Rossby wave was introduced independently by Raymond and Jiang (1990) and Snyder and Lindzen (1991). For these waves, the diabatic generation of PV plays the role of the meridional advection of PV in the classical Rossby wave. The growth mechanism, as described by PT95 (see their Fig. 6), is as follows: warm thermal advection to the east of a low-level positive PV anomaly results in forced ascent and the generation of positive low-level PV due to diabatic heating. In a balanced or quasi-balanced system, a positive PV anomaly is associated with a cyclonic relative circulation. Therefore, warm thermal advection occurs farther to the east, continuing the process and resulting in wave propagation in the direction of the thermal wind.

Under atmosphere-like conditions (such as in PT95 and this study), the low-level cyclonic circulation is associated with a diabatically produced, positive PV anomaly and a surface PT anomaly. Snyder and Lindzen's 1991 study of the unbounded baroclinic shear problem (where the Earth's surface is infinitely far away from the heating layer) illustrates that diabatic Rossby wave growth can occur in the absence of a PT anomaly. In their case, a discontinuity in the heating rate serves as a surrogate 'surface' where diabatic PV production takes place. In both cases, however, the growth mechanism can be described as above.

To our knowledge, the existence of diabatic Rossby waves in a system with the EFT parameterization of latent heat release has yet to be explicitly addressed. Are these diabatically-forced, coherent structures also present in our model framework?

As defined above, the answer is unmistakably yes. Overlays of the vertical velocity, meridional wind, PV and PV generation fields for a wavenumber 4.0 disturbance (dimensional wavelength = 1570 km) are presented in Figure 3.12a. Southerly winds are observed to the east of a positive low-level PV anomaly, leading to warm air advection, ascending motion and latent heat release to the east of the center of circulation. Positive low-level PV is thus generated to the east of the original PV anomaly and the wave propagates to the east (in the 2D model).

The simplified model results allow us to physically understand how wave growth can occur in the absence of upper-level forcing. In a conducive local environment, all that is necessary to initiate a diabatic Rossby wave is forced ascent. If the atmosphere is sufficiently unstable (through a combination of humidity and baroclinicity), latent heat release and PV generation will occur. Once the process has begun, continued ascent will occur in the form of warm air advection from the south (in the northern hemisphere) and the associated isentropic lifting that occurs as an air parcel travels northward on a potential temperature surface. The cyclonic disturbance will thus be able to sustain itself, through the constant production of diabatically-generated PV to the east of the original low-level PV anomaly, until the environment is no longer favorable.

While the above results illustrate that the existence of diabatic Rossby waves is not peculiar to the wave-CISK type of latent heat release parameterization, it is noteworthy that there are significant differences in the behavior of these waves for the two parameterization schemes. The 'solitary' modes presented in PT95 are typified by: i) a minimum updraft width that is nearly constant with zonal wavelength (see their

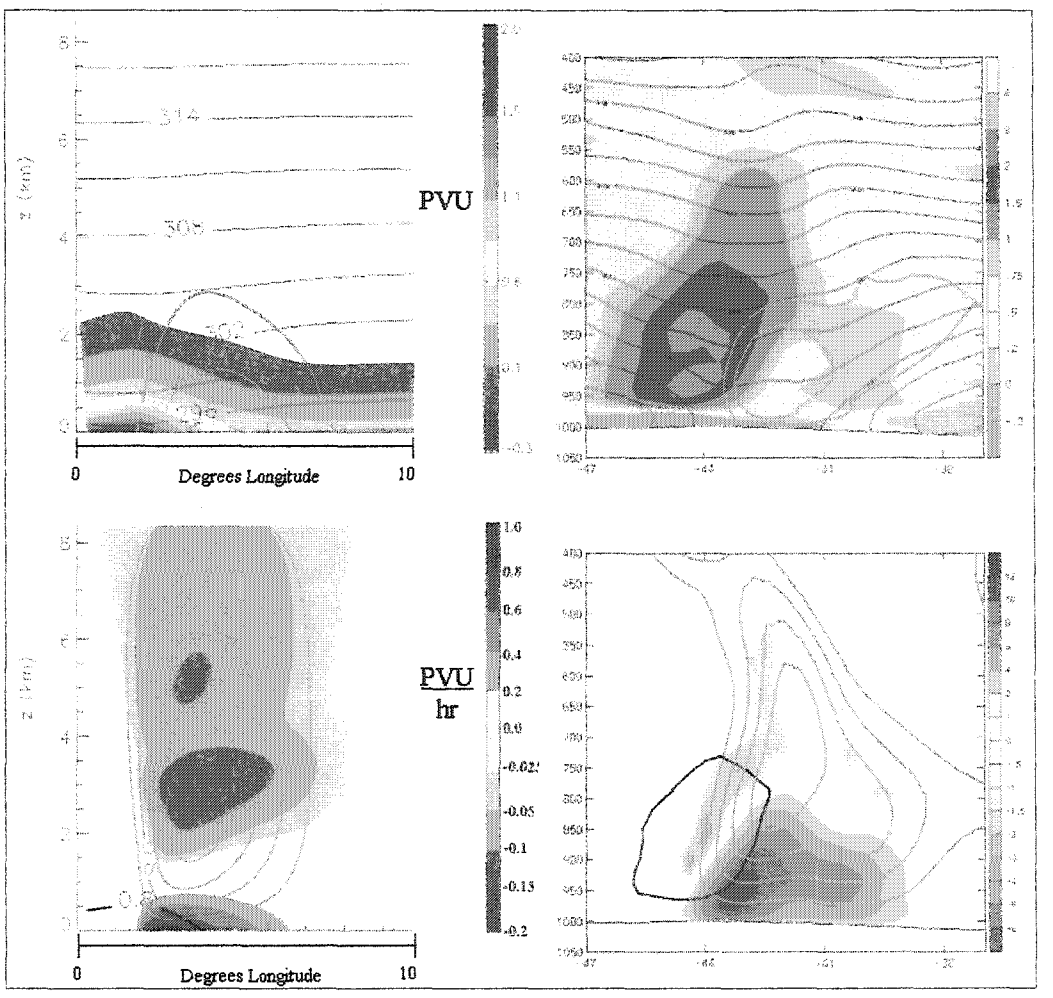

Figure 3.12 – Comparison between 2D, SG model results and ECMWF Reanalyses data for the precursor disturbance of extreme winter storm 'Lothar'. (a) West-east oriented vertical cross-section of selected 2D, SG model fields for a for an initial nondimensional wavenumber k=4.0 (dimensional wavelength = 1570 km) disturbance for a vertically varying moisture parameter [$R(Z) = R_o + (1 - R_o)Z$; $R_o=0.01$] at time T=6.93 days: upper panel) PV (PVU; shaded), potential temperature (K; thin black line) and three green, bold contours for the meridional wind (3, 5, and 7 ms^{-1}); and lower panel) diabatic PV generation rate (PVU hr^{-1}: shaded), vertical velocity (cms^{-1}; green contour lines at 0.4 cms^{-1} intervals; only ascending motion is shown), and the 0.8 PVU contour (bold black line). Please note the z = 0 surface corresponds to the top of the boundary layer. (b) West-east oriented vertical cross-section through the center of 'Lothar' from Wernli et al. (2002): upper panel) PV (PVU; shaded), potential temperature (K; thin black line) and

two green, bold contours for the meridional wind (20 and 23 ms^{-1}); and lower panel) diabatic PV generation rate (PVU hr^{-1}; shaded), vertical velocity (cms^{-1}; green contour lines, only ascending motion is shown), and the 1.5 PVU contour (bold black line).

Figure 3) and ii) an upper-level, meridional jet of larger magnitude than the low-level, meridional jet. With the EFT parameterization: i) the minimum updraft width decreases with decreasing zonal wavelength and ii) the strongest meridional winds are found at low-levels.

In a more realistic three-dimensional framework, these 2D features simulated with simple dynamical models appear as coherent vortices [see Raymond and Jiang 1990 (their Figure 6) and Montgomery and Farrell 1992 (their Figure 2)]. They are characterized by a closed circulation and the absence of the alternating high / low structure that is associated with wave-like disturbances. For this reason, we suggest that a more appropriate term for these disturbances is a diabatic Rossby vortex (we will hereafter use this designation). Future work is planed to address the debate as to the actual 3D structure and propagation characteristics of these features by running a mesoscale model, with and without explicit convection, to simulate the structure and evolution of a 'true' diabatic Rossby vortex.

3.5 Extreme Winter Storm 'Lothar'

Winter storm 'Lothar' was one of the most harmful storms to impact continental Europe in recent memory (Wernli et al. 2002; hereafter W02). It left a trail of destruction from northwestern France to southern Germany and Switzerland, resulting in the death of 50 people and significant damage to tourist sites such as Versailles and the church of Notre Dame (Ulbrich et al. 2001, W02).

An interesting dynamical feature that was the progenitor of what eventually became 'Lothar' was a prominent small-scale, low-level cyclone of moderate intensity. It propagated from the western Atlantic to the European mainland, where it subsequently intensified rapidly upon interacting with an intense upper-level jet. The incipient cyclone was associated with a low-level PV anomaly, resulting from continued, intense cloud diabatic heating. It was shallow and had no discernible upper-level feature (W02).

ECMWF analysis data were able to capture the structure and characteristics of the cyclone at this early stage (Figure 3.12b in this article – Figure 13 in W02). A comparison with the 2D model results shows the interaction between the wind, PV and PV generation rate fields is qualitatively very similar (note that when comparing the two plots, in the 2D, SG model with quadratic surface drag the $z = 0$ surface corresponds to the top of the boundary layer as opposed to the surface of the ocean). In fact, W02 compare this feature to a diabatic Rossby wave.

It is noteworthy that there are some significant quantitative differences between the model results and 'Lothar'. The observed translation speed (30 $ms^{-1)}$, peak magnitude of diabatic PV production (greater than 8 PV units hr^{-1}) and intensity of the southerly flow (23 ms^{-1}) associated with the low-level feature during 'Lothar' are significantly larger than that predicted by the simplified model. These discrepancies may well be due to the extreme environment in which 'Lothar' formed. W02 noted an upper-level jet flow with maximum wind velocities larger than 80 ms^{-1} (compared to the chosen value of 30 ms^{-1} for the Eady basic state) as well as unusually high sea surface temperatures. It seems logical that characteristics of a diabatic Rossby vortex are linked to the basic state environment in which it forms and amplifies; however, this issue will have to be explored in greater detail using a more 'realistic' model setting before any definite conclusions can be made.

The fact remains, however, that the incipient phase of extreme winter storm 'Lothar' provides an excellent observational example of a case where a diabatic Rossby vortex served as an antecedent lower-level, cyclonic disturbance. While the rapid deepening phase of 'Lothar' involved the interaction of this feature with an intense upper-level jet, the formation and subsequent development of the diabatic Rossby vortex occurred in the absence of any significant upper-level forcing. The simplified model results presented here clarify how this type of growth can occur: all that is necessary is warm air advection in a sufficiently moist, baroclinic environment.

3.6 Conclusions – 2D, SG Results

We have used a simplified, dynamical model with the EFT parameterization of latent heat release to diagnose the moist, exponentially growing modes of the Eady basic state and to investigate the role of short-scale, diabatic features in moist cyclogenesis.

In the model setting employed here, the vertical profile of latent heat release is largely controlled by the moisture parameter (R), essentially a measure of the deviation from moist neutrality along a constant absolute momentum surface. When R is allowed to vary in accordance with the expected temperature dependence of latent heat release, the result is a linearly increasing function of height. In comparison with the small but constant R case, this more realistic approach results in: i) decreased growth rates, ii) a shift to longer scales of the most unstable mode, iii) the absence of a shortwave cutoff, iv) constant growth rates for zonal wavelengths less than approximately 1900 km, and v) a more precipitous decrease of phase speed with decreasing characteristic zonal scale.

Consistent with the idea of a separation of scale of observed disturbances in the middle and high latitudes [e.g. long waves and cyclone waves (Eady 1949)], two growth regimes are identified. Similar to both the dry and small but constant R systems, waves

longer than 1900 km grow due to the mutual interaction of surface and tropopause PT anomalies. In contrast, for waves shorter than 1900 km, no upper boundary disturbance is necessary for growth. Instead, it is the constant production of diabatically-generated PV (through the process of warm air advection, rising motion and latent heat release) that allows for amplification. This disturbance structure and evolution has been identified as a diabatic Rossby wave; however, due to the anticipated vortical nature of these features, we suggest that a more appropriate name would be a diabatic Rossby vortex.

Even in the presence of 'realistic' surface friction, exponential growth is predicted over a large range of zonal wavelengths in the small but finite amplitude regime. As the vortex grows with time and surface wind speeds increase, quadratic surface drag becomes more effective at reducing growth. However, the results indicate that surface friction does not eliminate exponential instability in the modified, moist system (over an ocean surface) and that, once generated, small-scale modes can persist.

The fact that diabatic Rossby vortices have been identified in simplified, balanced systems incorporating a variety of latent heat parameterization schemes and observations suggest that they should be a robust feature of the moist, baroclinic atmosphere. Furthermore, the evolution of 'Lothar' indicates they can play an integral role in the two-stage process of explosive cyclogenesis described by Gyakum et al. (1992) by serving as a low-level, coherent vortex in the antecedent phase.

Based on the foregoing discussion, we can only conclude that better knowledge of the structure and propagation characteristics of diabatic Rossby vortices is vital to the understanding of any atmospheric process that involves instability in a moist, baroclinic environment. In the next section, we will incorporate a more complete model setting to simulate a 'true', three-dimensional diabatic Rossby vortex in an effort to further investigate the intrinsic characteristics of practical importance of these short-scale, diabatic features.

4. DRV Dynamics in a Full-Physics, Mesoscale Model

4.1 Control Simulation

The goal of this section is to document the formation, structure and evolution of a DRV in MM5, and to compare and contrast with previous results.

A snapshot of various model fields two days into the model integration is presented in Fig. 4.1. An isolated surface low pressure center measured at 1009.4 mb is observed at approximately 36N, -23W (Fig. 4.1a). A zonal / vertical cross section through the center of the surface pressure disturbance clearly shows the structure of a DRV: a positive low-level PV anomaly (Fig. 4.1g) is associated with southerly winds on the east side of the disturbance (Fig. 4.1b), rising motion (Fig. 4.1d) and latent heat release (Fig. 4.1e). The structure of the disturbance at this time clearly shows that the use of the term 'vortex' is more appropriate than 'wave': in addition to the absence of the alternating high / low structure that is associated with wave-like disturbances (Fig. 4.1a), a closed circulation is evident at 1000 mb (Fig. 4.1h).

4.1.1 DRV Formation

While the initial vortex is constructed with the basic structure of a DRV in mind, the temporal decay of the initial perturbation in model runs without moisture and environmental baroclinicity (as measure by the minimum surface pressure; see Fig. 4.2), respectively, illustrates that both ingredients are integral to the formation of the DRV.

4.1a)

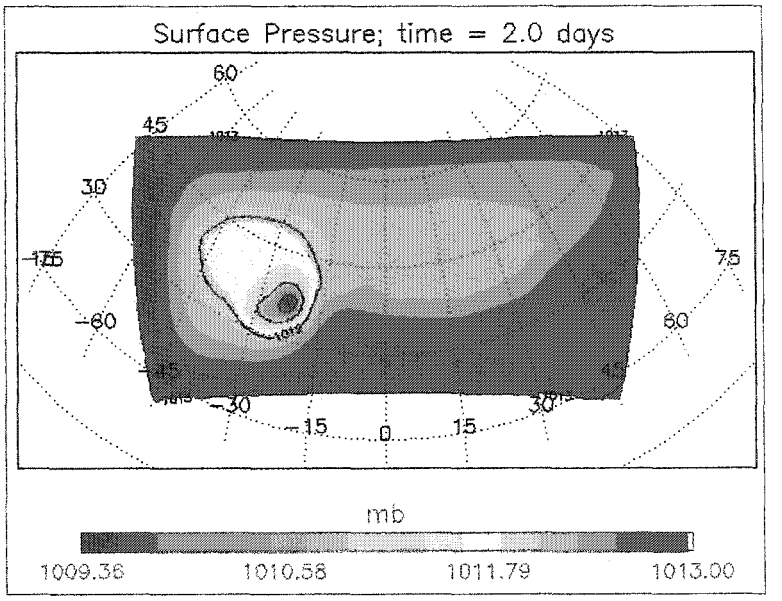

4.1b)

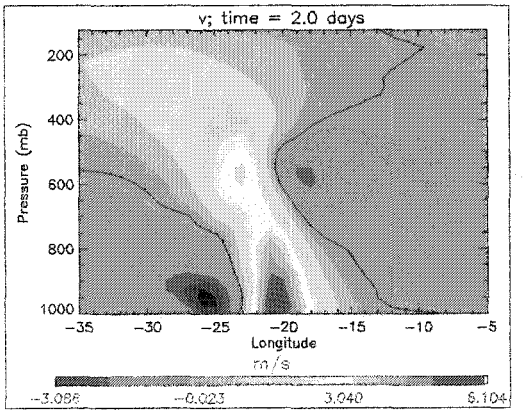

4.1c)

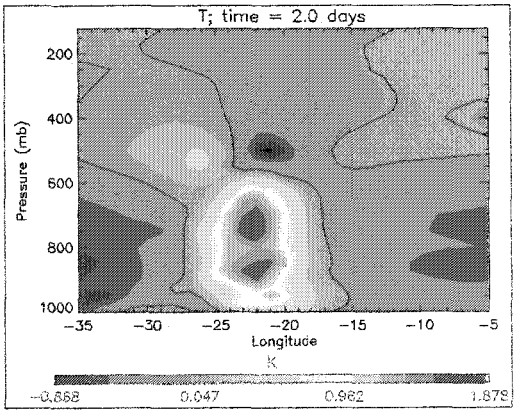

4.1d)

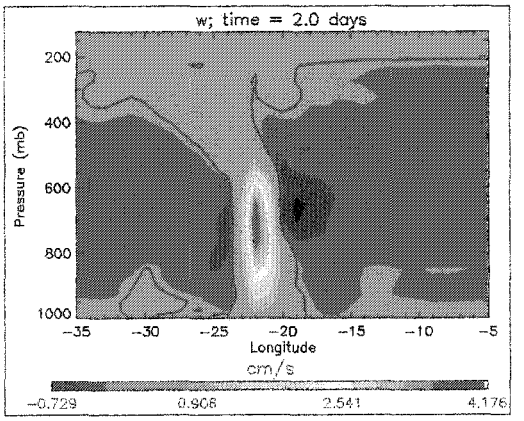

4.1e)

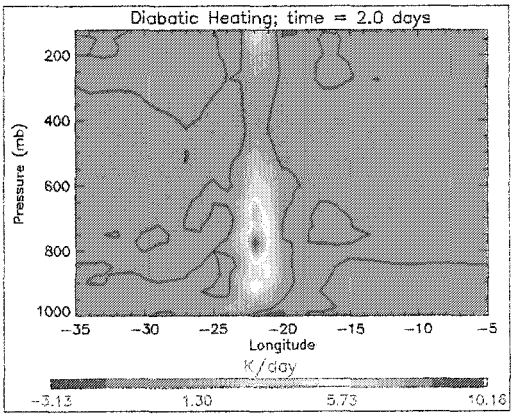

4.1f)

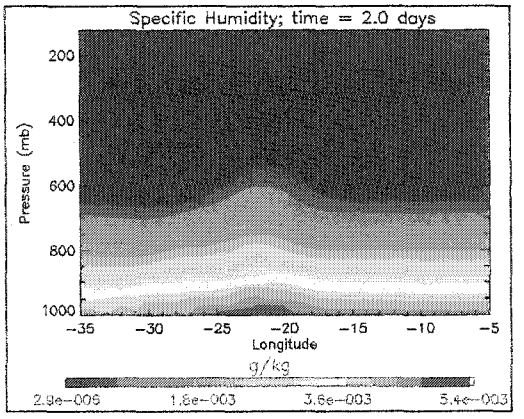

4.1g)

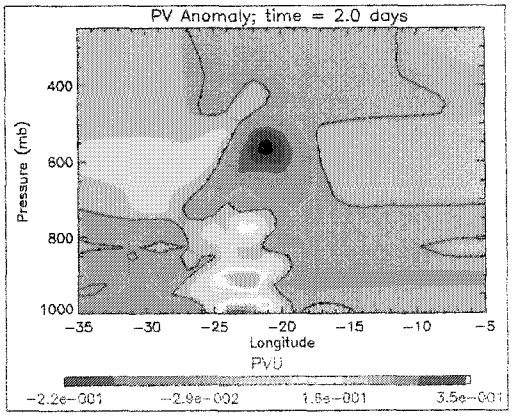

4.1h)

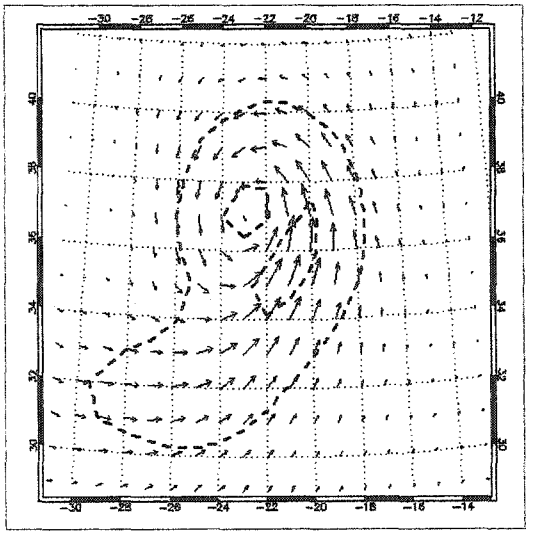

4.1 i)

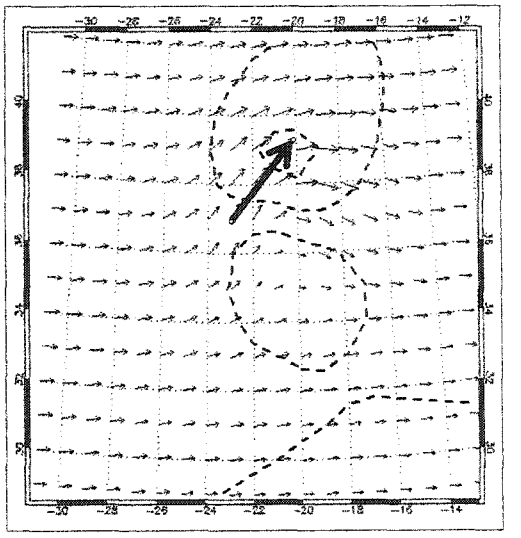

Figure 4.1 – MM5 model fields at 2 days simulation time: a) surface pressure (mb); b) meridional wind (ms^{-1}); c) temperature anomaly (K); d) vertical velocity (cms^{-1}); e) diabatic heating ($Kday^{-1}$); specific humidity; g) potential vorticity anomaly (PVU; 1 PVU = 10^{-6} $m^2s^{-1}K$ kg^{-1}), h) 1000 mb horizontal wind (ms^{-1}; maximum wind vector = 5.58 ms^{-1}; dashed contours every 5 ms^{-1}); and i) 550 mb horizontal wind (ms^{-1}; maximum wind vector = 10.65 ms^{-1}; dashed contours every 5 ms^{-1}; bold arrow represents the direction of the thermal wind vector)). Note: all longitude / pressure cross sections are taken at 36N.

Within three hours of model initialization, forced ascent associated with low-level cyclonic flow and warm air advection has resulted in convection in the northeast

sector of the perturbation vortex. The dynamical effect of the convection (through latent heat release and the evaporation and melting of precipitation) is to create a positive PV anomaly at low-levels and a negative PV anomaly in the mid-troposphere (Raymond and Jiang 1990; see Fig. 4.1g here). The precise level at which these anomalies are generated is dictated by the vertical profile of diabatic heating which, in turn, is a function of environmental parameters that affect the atmospheric stability. In this case, the presence of a nearly saturated layer at low-levels has created a nearly moist-neutral layer of similar depth.

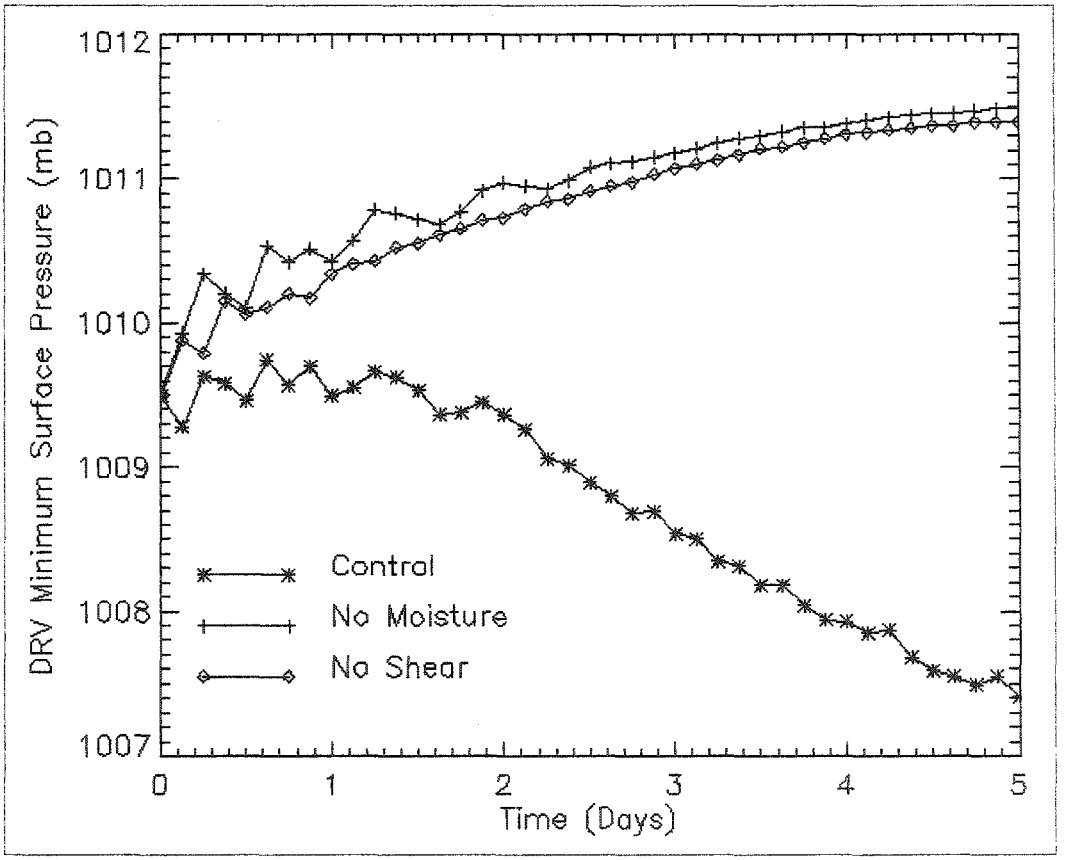

Figure 4.2 – Temporal evolution of the minimum surface pressure for the following MM5 simulations: the control run (*), no moisture (DRY; +) and no shear (NOSHEAR; ◊).

The low values of translation speed and a negative instantaneous growth rate over the first 48 hours (see Fig. 4.3) illustrate that an adjustment period is necessary

4.3a)

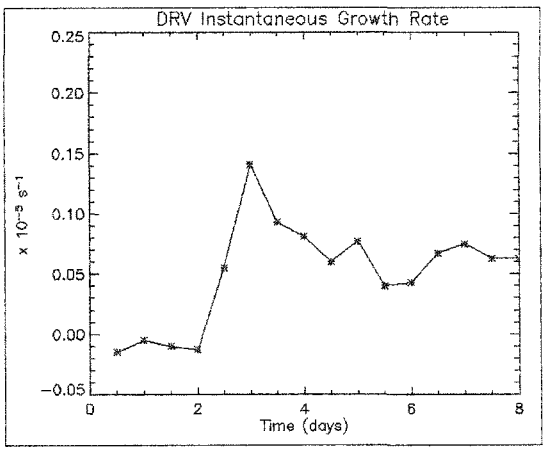

4.3b)

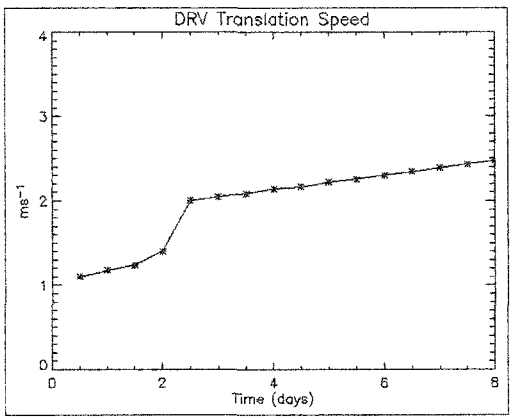

4.3c)

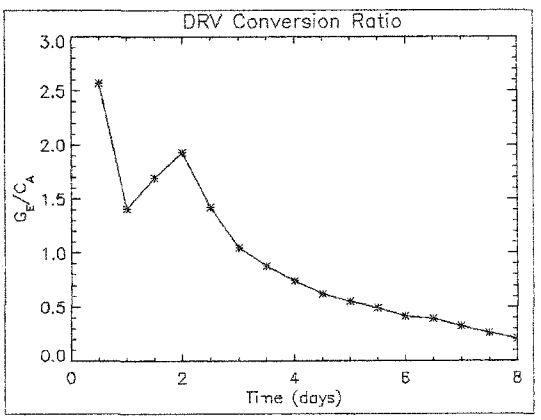

Figure 4.3 – Temporal evolution of the model diagnostics for the control simulation: a) instantaneous growth rate (x 10^{-5} s^{-1}); b) translation speed (ms^{-1}); and the conversion ratio of diabatic (G_E) to baroclinic (C_A) generation of eddy APE defined by Equation 2.1h.

before the DRV growth mechanism begins to operate. Until this time, the disturbance is being passively advected by the local steering level winds. The disturbance begins to amplify once a dipole structure in the anomalous PV field emerges in response to the continuous convection: a DRV is characterized by an approximate phase-locking of a low-level, positive PV anomaly and a mid-tropospheric, negative PV anomaly (see Fig. 4.1g). After DRV formation, the translation speed increases (Fig. 4.3b) to a value that

cannot be explained by simple advection by the steering level wind, a feature that has been noted previously (Parker and Thorpe, 1995; Wernli et al. 2002).

Parker and Thorpe (1995) noted that a DRV translates in the direction of the thermal wind. It is fairly straightforward to qualitatively confirm this result. If we assume the 550 mb wind is nearly geostrophic, the direction of the thermal wind defined by the 1000-550 mb layer at the center of circulation at 1000 mb (37N, -23W) is determined to be within a few degrees of the direction of DRV propagation over the subsequent 12-hour period period (the direction of the thermal wind vector is indicated by the bold arrow in Fig. 4.1i). The direction of the thermal wind and DRV translation is furthermore in good agreement with the location of the convection at day two (to the northeast of the circulation center), as one might intuitively expect given that fact that DRV dynamics are intimately tied to the diabatic generation of PV.

In addition to the purely zonal propagation of a DRV predicted in 2D studies, there is a northerly component to the DRV translation in this more complete model setting. A physical argument for this process can be gleaned from previous work on the motion of tropical cyclones in a baroclinic environment (Wu and Emanuel 1993). One effect of the ambient environmental shear is to displace the upper-level, anticyclonic PV anomaly downshear of the lower-level, cyclonic PV anomaly. In their tropical cyclone study, Wu and Emanuel (1993) found that this process allowed for a mutual interaction between the two PV anomalies that results in a drift of the surface cyclone to the left of the shear vector. In westerly shear, the result is a northerly drift of the disturbance.

This same process is observed here. While the northerly drift may be due in part to the background, surface PV gradient (increasing from south to north), a comparison between the control simulation and a dry simulation clearly shows that the northerly drift is larger in the former. This particular effect of moisture in a baroclinic environment was

also found by Liou and Elsberry (1987) in their study of an explosively deepening maritime cyclone.

4.1.2 Comparison of a 2D and 3D DRV

The DRV structure observed in Fig. 4.1 is strikingly similar to that seen in the 2D study of MM04 (see their Fig. 4): to the east of the vortex center, low-level southerly flow leads into the base of the mesoscale updraft. The ensuing rising motion results in saturation, latent heat release and diabatic PV generation. The DRV is observed to be a warm core system (in the lower to mid-troposphere) in both studies.

The largest discrepancy between the 2D and 3D results is found in the mid-troposphere. The strength of the negative, mid-tropospheric PV anomaly is much stronger in the three dimensional simulation. In two dimensions (x-z), the ratio of the absolute magnitude of the low-level to the mid-tropospheric PV anomaly is relatively large (a ratio of about 5 to 1 is observed at 47.5 hours in MM04's Fig. 4). In contrast, the ratio at day two in the 3D simulation is approximately 1.6. Previous studies (Montgomery and Farrell 1991 and 1992; Whitaker and Davis 1994) have attributed this type of disturbance growth to the interaction and mutual amplification of a surface potential temperature anomaly and an interior, diabatically-generated negative PV anomaly. This mechanism is more clearly observed in the 3D results.

A direct repercussion of the enhanced mid-tropospheric PV anomaly is the presence of a secondary maximum in the meridional wind field at this level. This feature that is only hinted at in the results of MM04 has been observed in previous 2D studies (Fantini and Buzzi 1994 and 1997; Mak 1994 and 1998; Fantini 1995). The degree of distinction appears to be the result of the precise method of incorporating moisture effects. The moisture parameter used in MM04 (essentially a measure of the deviation

from moist neutrality) was smooth in the vertical. In contrast, methods that have incorporated a sharp gradient in either the vertical profile of moisture (Fantini and Buzzi 1994 and 1997; Mak 1994; Fantini 1995) or static stability (Mak 1998) capture the presence of a secondary maximum in the meridional wind field, most likely as a result of focusing the level at which PV generation occurs, thereby increasing the local magnitude of the anticyclonic PV anomaly.

The instantaneous growth rate and translation speed associated with the DRV at day two are approximately 0.1 x 10^{-5} s^{-1} (e-folding time of about 11.5 days) and 2.5 ms^{-1}, respectively. While these numbers are much smaller than for a DRV of equivalent scale in MM04, the results are not inconsistent. The environmental baroclinicity of the control run is significantly weaker than that used in MM04, so one would expect reduced values for the instantaneous growth rate and translation speed. Furthermore, the values obtained in MM04 are artificially high due the two-dimensionality of the problem formulated there.

The conversion ratio of diabatic to baroclinic generation of eddy APE for the control run is about 1.9 at day two (Fig. 4.3c). Although this value is also low compared to the numbers calculated in MM04, it is logical to expect a lower conversion ratio in the more complex model setting used here. As a result of assuming that all downdrafts are dry in MM04, diabatic heating rate is relegated to being either positive or exactly zero. Furthermore, one must also take into account the respective areas of integration in the calculation of the energetic conversion terms. In two dimensions (x-z), the vertical cross-section is a slice through the region of maximum convection. In three dimensions (x-y-z), the volume of integration is dominated by mesoscale downdrafts / synoptic-scale subsidence where the diabatic generation of eddy APE will be either small and / or negative. These effects, taken in combination, result in a significantly reduced value of the conversion ratio in three-dimensional settings. From a more traditional baroclinic

instability simulation, where the ensuing disturbance is characterized solely by the interaction between lower- and upper- boundary anomalies, it is clear that the conversion ratio is much higher for the DRV.

4.1.1 Evolution of a 3D DRV

(i) *Instantaneous Growth Rate, Translation Speed and Local Energetics*

The temporal evolution of the growth rate, translation speed and local energetics are presented in Fig. 4.3. Soon after the DRV begins to deepen, there is a 'burst' of disturbance growth (as indicated by large values of instantaneous growth rate; Fig. 4.3a), a feature that is found for all simulations. An examination of the temporal evolution of the diabatic generation of eddy APE (not shown here) shows that a large increase over a short time period in this parameter coincides with DRV formation, indicating that diabatic processes are mostly responsible for the 'burst' of growth observed at this time.

The magnitude of the instantaneous growth rate during the growth burst is significantly higher than at later times. The observed temporal evolution of the instantaneous growth rate is the result of many factors. Firstly, the characteristic depth of the DRV is smallest immediately after formation and is observed to grow with time (compare Figs. 4.1 and 4.4). In their study of DRV characteristics MM04 found that, at small but finite disturbance amplitude, a disturbance is more efficient at converting diabatic heat sources to eddy APE when the level of maximum heating occurs lower in the atmosphere. Given this fact alone, one might logically expect a larger value of the instantaneous growth rate at earlier times when the DRV is its most shallow.

MM04 also noted that the instantaneous growth rate of a disturbance in the presence of surface quadratic drag decreases with increasing disturbance amplitude (see their Fig. 7). Again, this effect would tend to result in larger growth rates at earlier times. Finally, the decrease in temperature at higher latitudes is associated with a decrease in

moisture content (due to the constant relative humidity profile). As the disturbance translates to the northeast, there is less potential for the generation of kinetic energy through diabatic processes. All of these factors tend to decrease the instantaneous growth rate over time.

A compensating influence, however, is the increase in environmental baroclinicity as the DRV translates northward (up to 45N) which results in an increase in the baroclinic generation of eddy APE. Ultimately, the positive and negative effects on the instantaneous growth rate taken in conjunction tend to average out, and a nearly constant value of instantaneous growth rate emerges.

This shift in the relative effects of diabatic to baroclinic processes is clearly evident in the temporal evolution of the conversion ratio (Fig. 4.3c). The burst of growth is associated with a peak in this diagnostic, again illustrating that the burst is largely due to diabatic processes. Subsequent to the burst of growth, the available environmental moisture decreases at the same time that the environmental baroclinicity increases, leading to a steady decline in the ratio.

(ii) *Disturbance Structure*

To examine the structural evolution of the DRV, selected model fields at day four are presented in Fig. 4.4. In addition to the more organized appearance of the DRV, the most apparent change over this 48-hour period is the increased strength of the mid-tropospheric anticyclonic circulation associated with the negative PV anomaly at this level. The ratio between the magnitude of the lower-level and mid-tropospheric PV anomalies has continued to decrease with time. As a result, the maximum of meridional wind at these two levels are nearly equal.

4.4a)

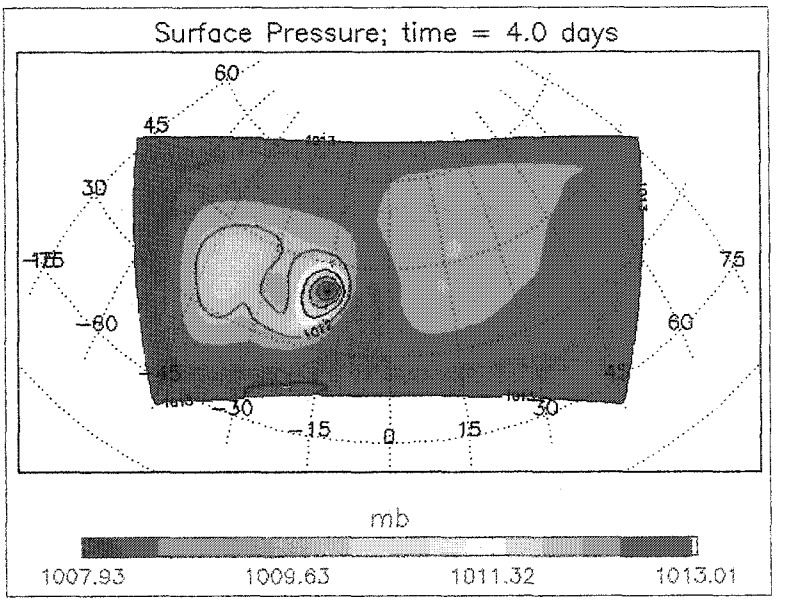

4.4b)

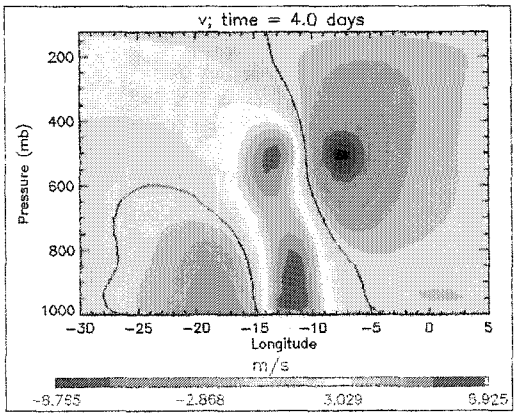

4.4c)

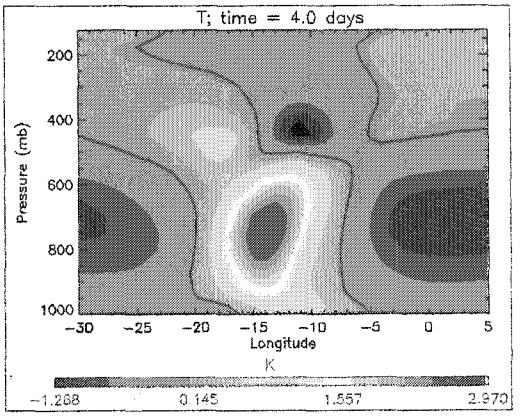

4.4d)

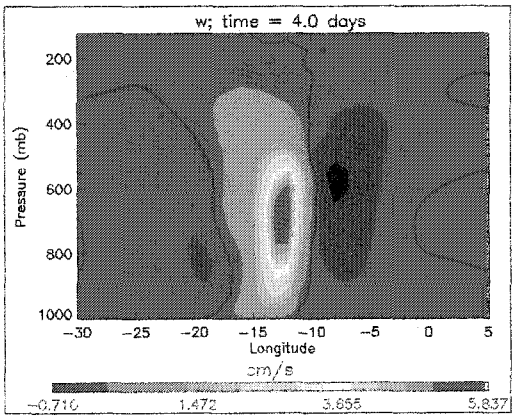

4.4e)

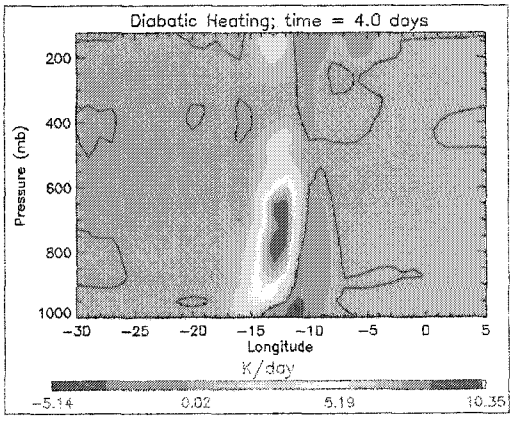

4.4f)

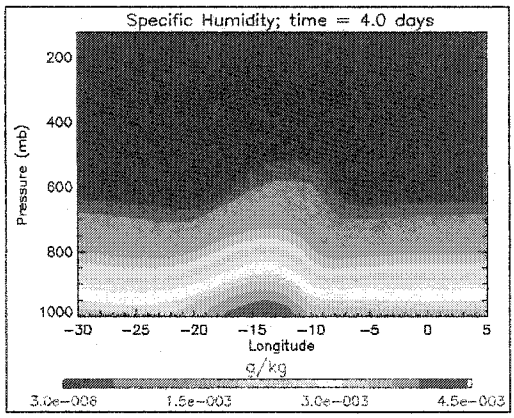

4.4g)

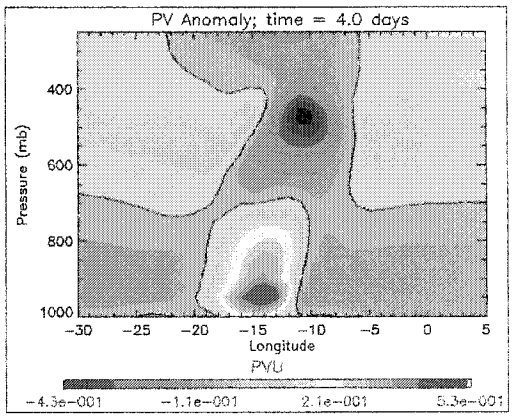

4.4h)

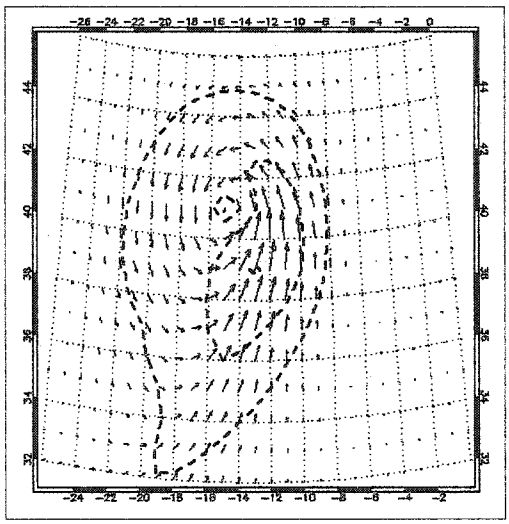

4.4 i)

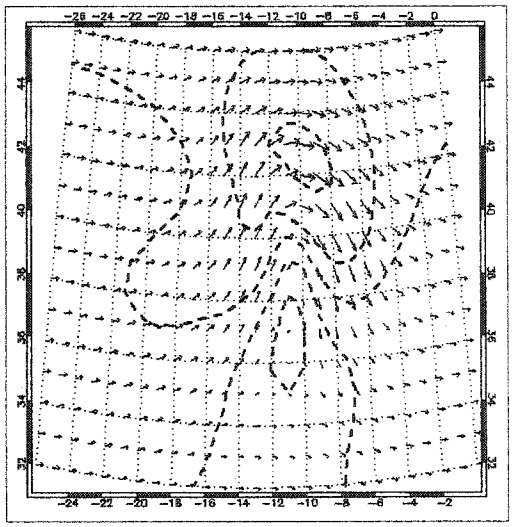

Figure 4.4 – Same as Fig. 4.1 except 4 days simulation time and longitude / pressure cross section at 41N. Note: h) 1000 mb horizontal wind (ms^{-1}; maximum wind vector = 7.63 ms^{-1}); and i) 500 mb horizontal wind (ms^{-1}; maximum wind vector = 16.21 ms^{-1}).

The increased depth of the DRV noted above can be seen in Fig 4.4. The height of the maximum of the negative mid-tropospheric PV anomaly has moved from about 550 mb at day two to 475 mb at day four. This feature of DRV evolution is observed for all model simulations executed here and illustrates how the DRV modifies the initial moisture field. As the DRV intensifies with time, the stronger horizontal and vertical

flow results in increased vertical advection of moisture in ascent regions. In this way, the DRV interacts with the background environment to increase the depth of the nearly saturated layer, thereby leading to a deeper DRV.

By day 7, significant changes in the DRV structure are evident. The DRV is no longer an isolated feature in the surface pressure field (Fig. 4.5a). Rather, a series of alternating anti-cyclonic and cyclonic disturbances are observed on either side of the DRV. This process can be understood from total relative angular momentum considerations (Shapiro and Ooyama 1990). Flierl et al. (1983) noted that a slowly varying and isolated vortex on a beta plane must have zero net angular momentum. Therefore, if the initial perturbation vortex has non-zero total relative angular momentum, it cannot remain isolated indefinitely. To adjust to this constraint, the perturbation vortex radiates Rossby waves (e.g. McWilliams and Flierl 1979; Shapiro and Ooyama 1990). In this context, the radiated Rossby waves are primarily thermal Rossby waves that arise due to the meridional surface gradient of potential temperature, as indicated by the surface concentrated nature of the potential temperature and pressure perturbations associated with these features.

While the DRV remains a robust coherent structure, it is apparent that the DRV is transitioning into a more baroclinic system. Accompanying the clear decrease in the conversion ratio of diabatic to baroclinic conversion to eddy APE (Fig. 4.3c), a more frontal structure is beginning to emerge (see the convergence line in 1000 mb circulation in Fig. 4.5h). Furthermore, a distinct change in the circulation pattern is predicted: the depths of both the low-level cyclonic circulation and mid-tropospheric anti-cyclonic circulation are observed to increase with time (Fig. 4.5b). At subsequent times (not shown here), a cyclonic circulation near the tropopause level is observed upstream of the surface cyclonic circulation, resulting in a disturbance structure more reminiscent of a traditional baroclinic wave.

4.5a)

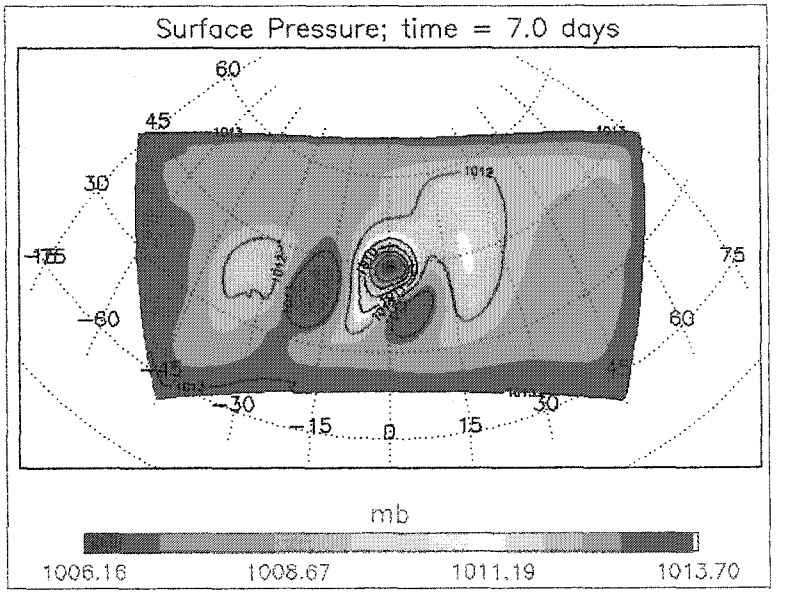

4.5b)

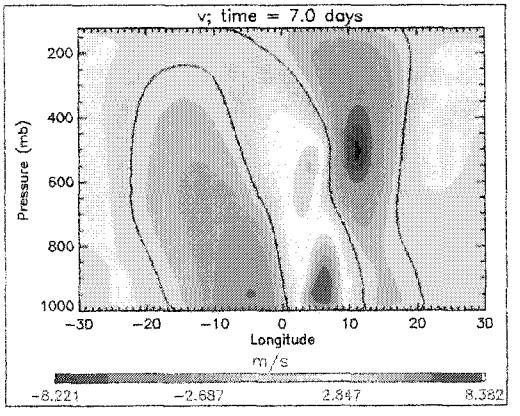

4.5c)

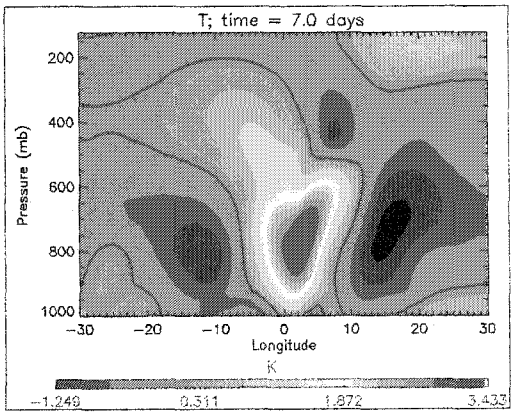

4.5d)

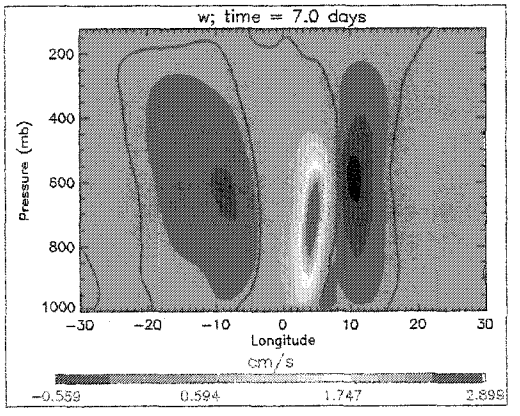

4.5e)

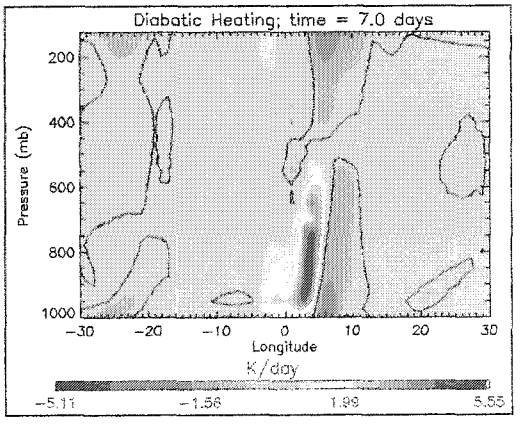

4.5f)

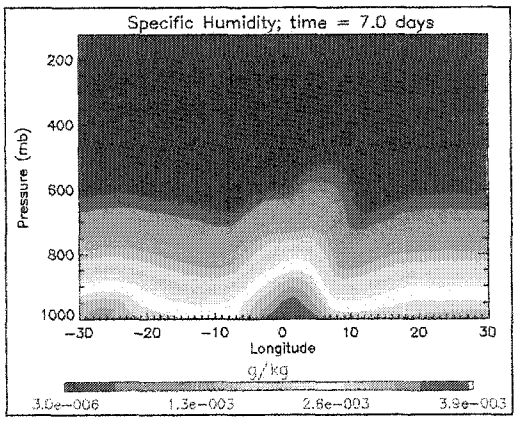

4.5g)

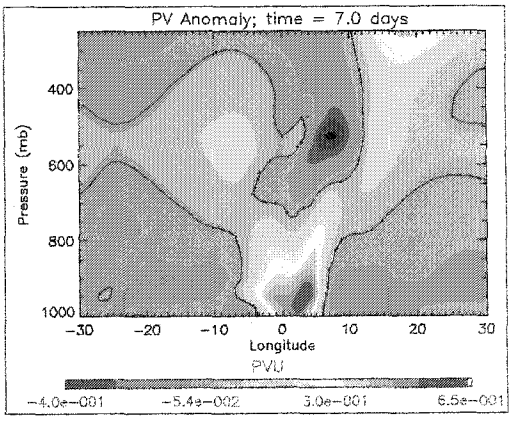

4.5h)

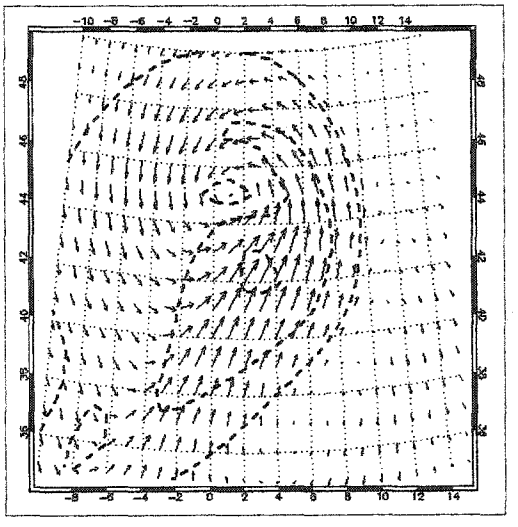

4.5 i)

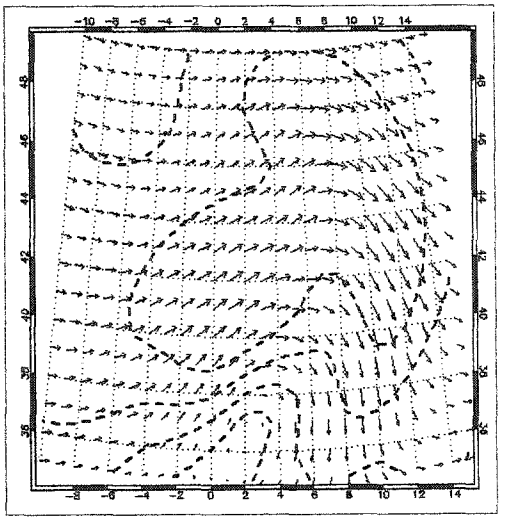

Figure 4.5 – Same as Fig. 4.1 except 7 days simulation time and longitude / pressure cross section at 45N. Note: h) 1000 mb horizontal wind (ms^{-1}; maximum wind vector = 7.84 ms^{-1}); and i) 500 mb horizontal wind (ms^{-1}; maximum wind vector = 14.68 ms^{-1}).

4.2 Results of Sensitivity Experiments

The purpose of this section is to determine and quantify the sensitivity of DRV characteristics to some of the more pertinent environmental and perturbation vortex

parameters. In an effort to emphasize the sensitivity of DRV growth and evolution to said parameters, we will limit or examination to cases where DRV formation does occur.

4.2.1 Environmental Baroclinicity

The effects of a change in the magnitude of the environmental baroclinicity are as dramatic as they are intuitive. The sensitivity of the instantaneous growth rate, translation speed and the conversion ratio of diabatic to baroclinic generation of eddy APE at day four are presented in Fig. 4.6. Qualitatively, the results are simple to interpret: an increase in environmental baroclinicity results in a faster-growing (Fig. 4.6a) and more rapidly-moving DRV (Fig. 4.6b).

In response to a more intense DRV (as measured by the surface pressure perturbation and the strength of the flow field associated with the DRV), the magnitude of both the diabatic and baroclinic generation of eddy APE are significantly larger (not shown here). The fractional increase in the baroclinic generation due to the increased baroclinicity is greater, however, resulting in a decrease of the conversion ratio of diabatic to baroclinic effects with increasing baroclinicity (Fig. 4.6c).

4.6a)

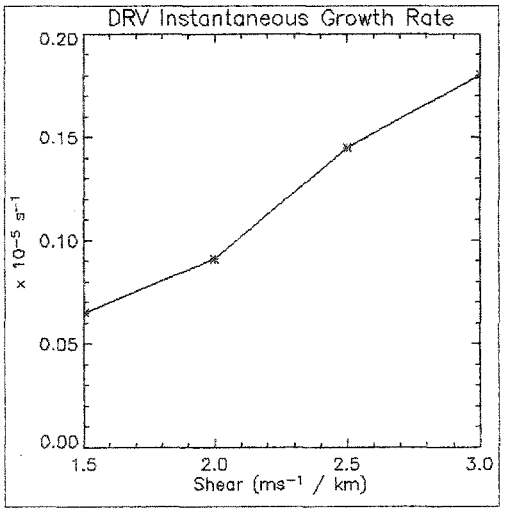

4.6b)

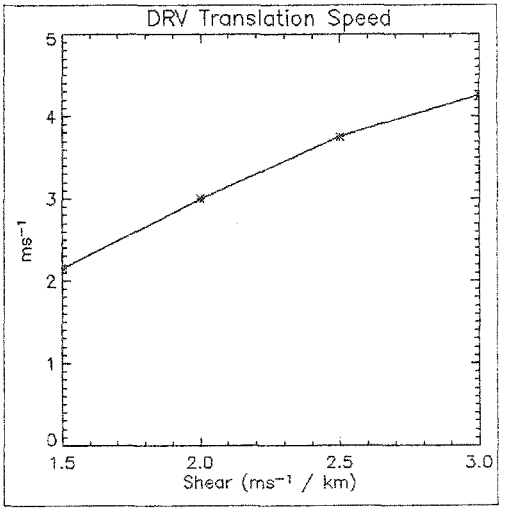

4.6c)

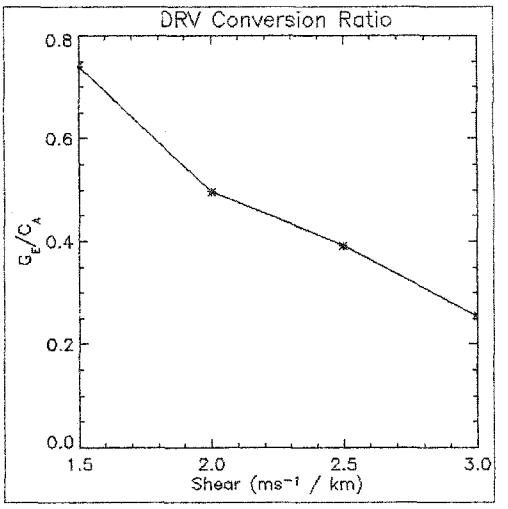

Figure 4.6 – Sensitivity of MM5 model diagnostics to the maximum magnitude of the environmental shear at time = 4 days: a) instantaneous growth rate (x 10^{-5} s^{-1}); b) translation speed (ms^{-1}); and the conversion ratio of diabatic (G_E) to baroclinic (C_A) generation of eddy APE.

4.2.2 Environmental Moisture

The sensitivity of the instantaneous growth rate, translation speed and the conversion ratio of diabatic to baroclinic generation of eddy APE to the depth of the initial moist layer at day 4.5 are presented in Fig. 4.7. The sensitivity of DRV dynamics to environmental moisture is more complex than that to environmental baroclinicity. Both the absolute magnitude of environmental moisture and the vertical structure of the moisture field need to be considered.

The observed sensitivity to the former is straightforward: in agreement with the findings of MM04, an increase in the magnitude of moisture content results in a faster-growing (Fig. 4.7a) and more rapidly-moving DRV (Fig. 4.7b). This point is highlighted by the drastically reduced values of the instantaneous growth rate and translation speed

4.7a)

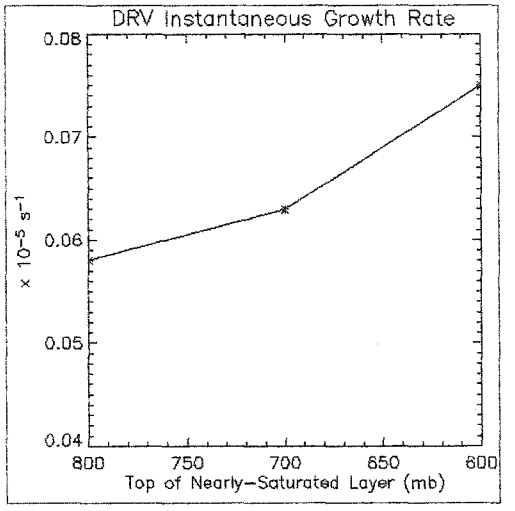

4.7b)

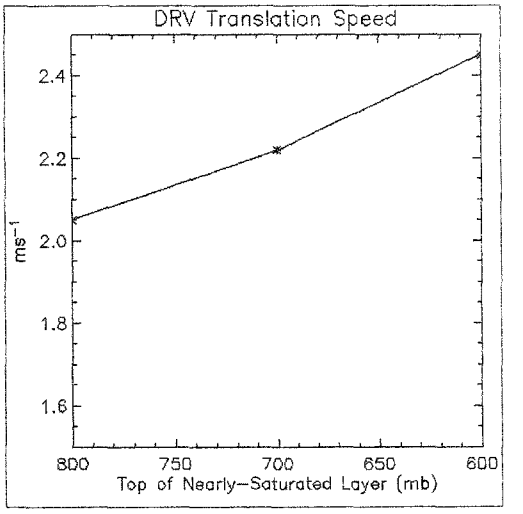

4.7c)

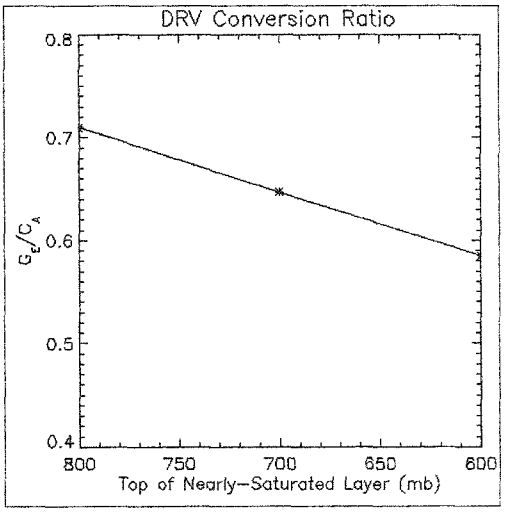

Figure 4.7 – Same as Fig. 4.6 except for sensitivity to environmental moisture (defined by the pressure level at the top of the nearly-saturated layer) and time = 4.5 days.

that are predicted by a model simulation incorporating zonally-averaged, climatological relative humidity data from ECMWF Reanalyses (a case with significantly reduced amounts of total moisture; not shown here). While the above trend is the same as for an increase in environmental baroclinicity, it should be noted that the magnitude of the

increase in instantaneous growth rate and translation speed is significantly smaller in the case of increased moisture content (compare Figs. 4.6 and 4.7).

The vertical structure of the moisture field is also important because it largely defines the characteristic depth of the DRV. The production of interior PV anomalies occurs in regions where a sharp vertical gradient in the heating rate exists (Montgomery and Farrell 1991 and 1992; Mak 1994). The results contained in Figs. 4.3 and 4.4 and previous research (Fantini and Buzzi 1994 and 1997; Mak 1994; Fantini 1995) clearly show that the vertical profile of the vertical velocity and diabatic heating is strongly controlled by the vertical profile of moisture. If all other factors are equivalent, the level of maximum diabatic heating is higher for a deep moist layer than for a shallow moist layer. In this way, the depth of the moist layer determines the levels at which the diabatic production of negative PV occurs and, as a result, the characteristic depth of the DRV.

Previous 2D results have shown the characteristic depth of a DRV has distinct repercussions on the DRV dynamics. In the presence of quadratic surface drag, a deep DRV was found to grow faster, propagate more quickly and exhibit a lower conversion ratio than a shallow DRV (MM04). It is evident that despite the 3D dynamics and complex environment of this model setting, the basic predictions of MM04 are broadly confirmed.

4.2.3 Initial Vortex Structure

In MM04, the characteristic depth of the observed disturbance was found to be directly tied to the zonal scale of the initial disturbance. The authors did hypothesize, however, that in the true atmosphere it is likely that environmental factors, such as moisture or stability stratification, are more important in determining the characteristic scale of any ensuing disturbance. By examining the sensitivity of DRV structure to the 'size' and 'strength' of an initial perturbation vortex (see the Appendix for details), it is

possible to test whether it is the characteristics of the background environment or a perturbation disturbance that primarily determines the structure of a DRV.

4.8a)

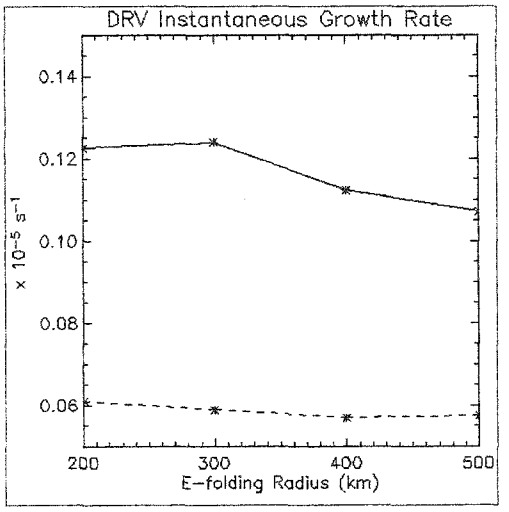

4.8b)

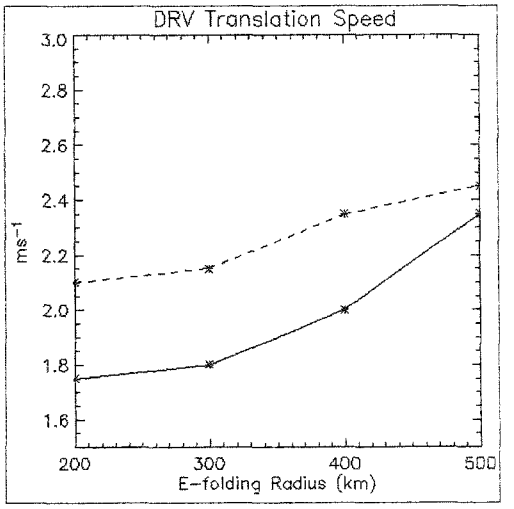

4.8c)

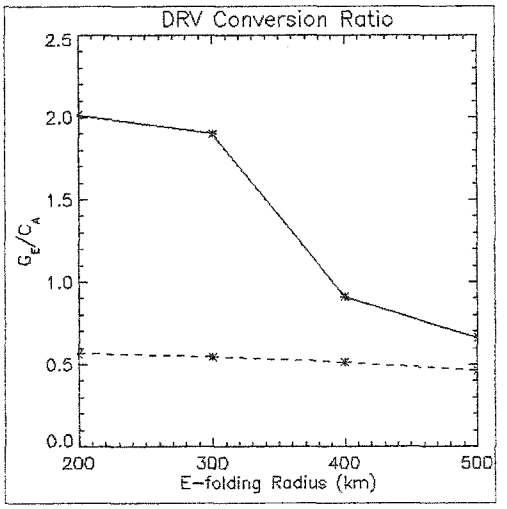

Figure 4.8 – Same as Fig. 4.6 except for sensitivity to the 'size' of the initial perturbation vortex (as measured by the e-folding radius of the potential temperature perturbation at the surface). Two times are presented: time = 2.0 days (solid line) and time = 5 days (dashed line).

4.9a)

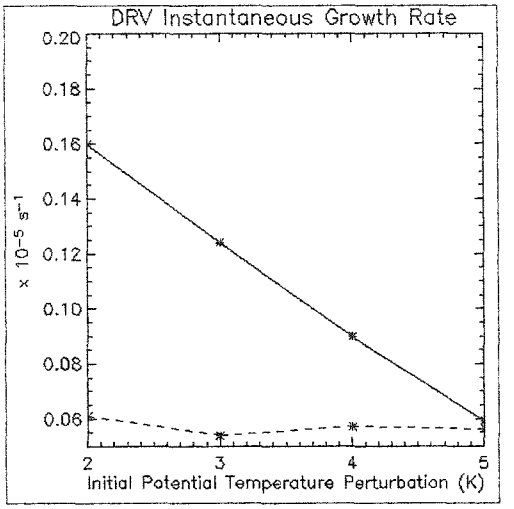

4.9b)

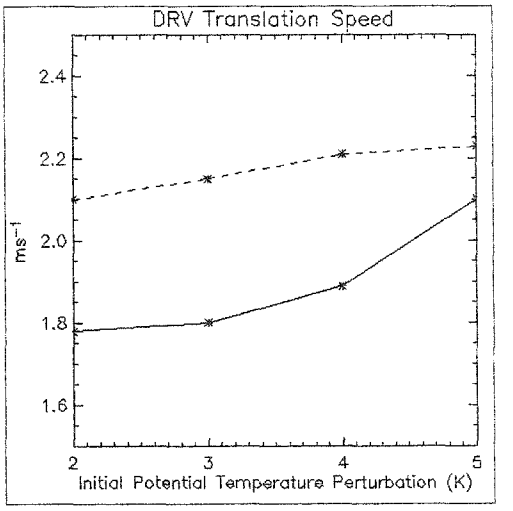

4.9c)

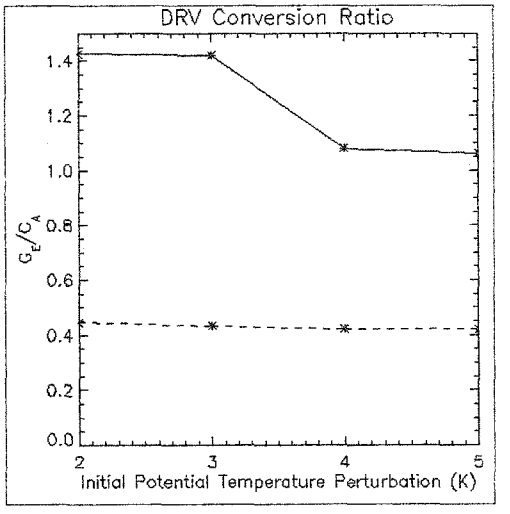

Figure 4.9 – Same as Fig. 4.6 except for sensitivity to the 'strength' of the initial perturbation vortex (as measure by the maximum potential temperature perturbation at the surface). Two times are presented: time = 2.5 days (solid line) and time = 6 days (dashed line).

The sensitivity of the instantaneous growth rate, translation speed and the conversion ratio of diabatic to baroclinic generation of eddy APE to the 'size' and 'strength' of the initial vortex are presented in Figs. 4.8 and 4.9, respectively. The data

are presented at two distinct times to highlight a central point: it is apparent from the lack of sensitivity of DRV characteristics to both the initial vortex 'size' and 'strength' that is observed at later times (see dashed lines in Figs. 4.8 and 4.9) that, to the first order, it is the environmental background state that is the primary determinant of the depth of the DRV and its characteristics.

An examination of DRV structure for these model simulations indicates that, once the initial perturbation vortex has been given sufficient time to adjust to its environment (approximately 4-6 days), the depth of the ensuing DRV and its characteristics are observed to be nearly identical to that of the control run. This result has important implications for the operational forecasting of DRVs: clearly, an accurate portrayal of the initial condition field (in the form of the temperature and moisture structure of the environment) is integral for a proper forecast of DRV formation, growth and evolution.

While the characteristics of the initial vortex are not the principle factor in determining the scale of the ensuing DRV, the significant sensitivity of the translation speed (Figs. 4.8b and 4.9b) and instantaneous growth rate (Figs. 4.8a and 4.9a) to the 'size' and 'strength' of the initial vortex that is observed at early times indicates a proper depiction of the perturbation field is also important from a forecasting perspective. To illustrate this point, the daily-averaged disturbance track for four DRVs (representing strong, weak, large and small initial perturbation vortices; experiments ST3, ST1, SI3, and SI1, respectively, in Table 2.1) are shown in Fig. 4.10.

The predicted discrepancy in disturbance track is due to two effects: the sensitivities of the timing of DRV formation (and the increase in northerly drift associated with this event) and the magnitude of the translation speed to the characteristics of the initial vortex. A larger/stronger initial vortex is found to transition to a DRV more quickly, resulting in a more northerly track. In addition, a larger/stronger

vortex translates more quickly (see Figs. 4.8b and 4.9b). As a result, there is a predicted discrepancy of nearly 600 km by day 6 in the most extreme case. It also should be noted that, at this same time, there is a discrepancy in disturbance intensity of about 3 mb, due to the sensitivity of the instantaneous growth rate to the characteristics of the initial vortex (Figs. 4.8a and 4.9a).

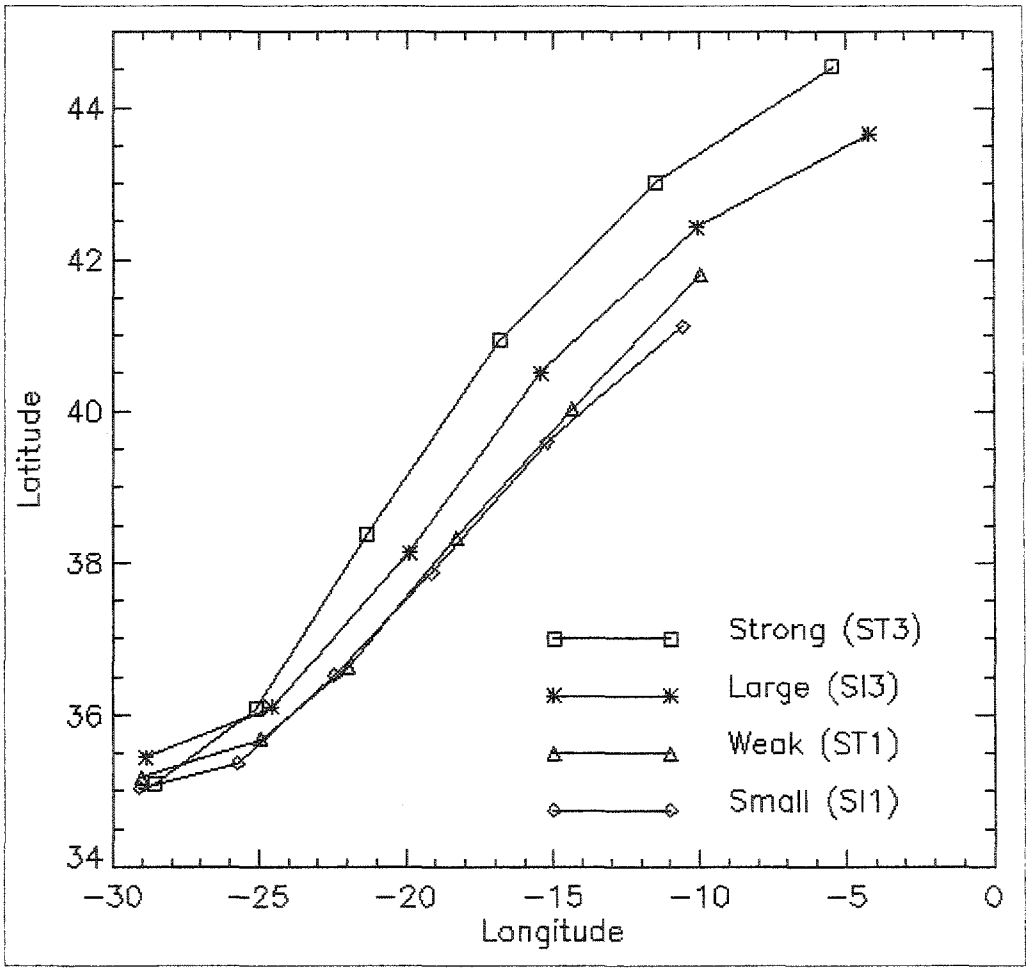

Figure 4.10 – Sensitivity of the disturbance track to the 'size' and 'strength' of the initial vortex for the following MM5 simulations: ST3 (□), SI3 (*), ST1 (Δ), and SI1 (◊). Each grid point represents a daily-average of the instantaneous translation speed. The time range is from 0 to 6 days.

4.2.3 Model-based Parameters

To ascertain if the model results are sensitive to the MM5 physics packages that are employed, the effect of altering certain model-based parameters is now examined.

A comparison of the temporal evolution of the minimum surface pressure for both the Grell (control run) and Kain-Fritsch 2 (Kain 2002) cumulus parameterizations is presented in Fig. 4.11. After 11 days, the minimum surface pressure for the two model simulations differs by only 0.12 mb and the respective locations of the two simulated DRVs are within 50 km of each other.

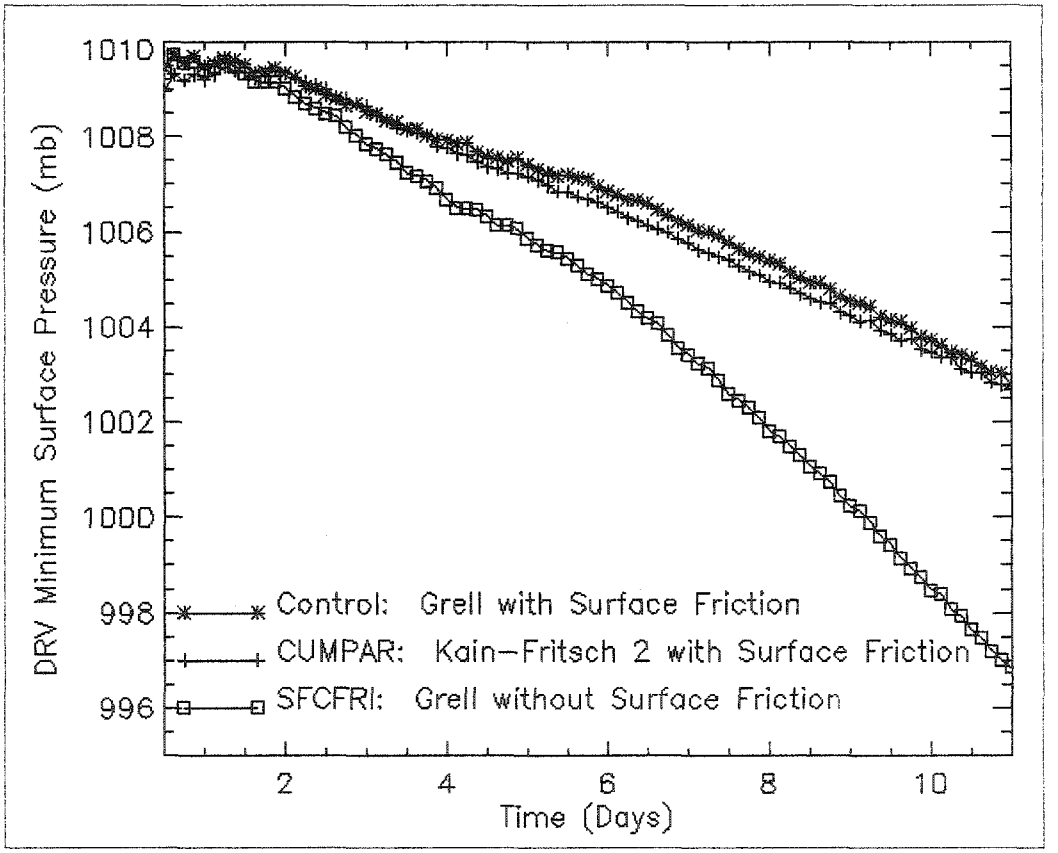

Figure 4.11 – The temporal evolution of the minimum surface pressure for the following model simulations: Control (Grell cumulus parameterization with surface friction; *), CUMPAR (Kain-Fritsch 2 cumulus parameterization; +) and SFCFRIC (Grell cumulus parameterization without surface friction; □).

Also presented in Fig. 4.11 is the result from a simulation of the control run with surface friction turned off (SFCFRIC). As one would expect, a more intense DRV is predicted in the absence of frictional dissipation (MM04). Furthermore, the distance between the two simulated DRVs is approximately 400 km after 11 days.

To investigate the sensitivity of the study results to the MM5 grid spacing, additional simulations with the control run setup were made with increased resolution. The surface pressure field at day five for both the control and a simulation incorporating 30 km grid spacing is presented in Fig. 4.12. The higher resolution DRV exhibits a somewhat lower minimum surface pressure. It is apparent, however, that the qualitative structure of the DRV is similar for both simulations.

a) b)

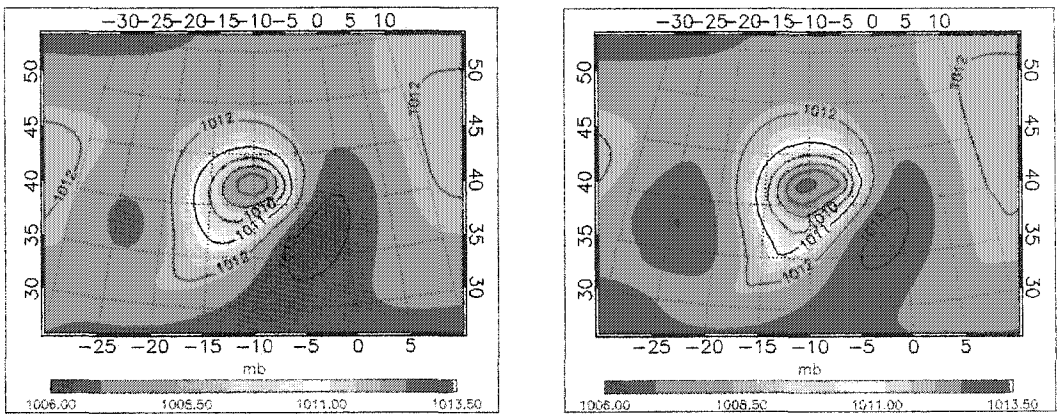

Figure 4.12 – The sensitivity of DRV structure to the horizontal resolution. The surface pressure field at day five for a horizontal resolution of: a) 90 km (control) and b) 30 km (RES).

Finally, one model simulation including latent and sensible heat surface fluxes was carried out. The temporal evolution of the minimum surface pressure (not shown here) illustrates that the inclusion of surface fluxes does further intensify the DRV;

however, this effect is relatively small. At day five, a further deepening of only about 0.4 mb is predicted when surface fluxes are included.

Given these findings, we believe the principal results reported here concerning the DRV are robust.

5. Summary and Conclusions

5.1 Study Results

We have used both a simplified, dynamical model and a full-physics mesoscale model to examine the dynamics of short-scale, diabatic disturbances and explore the role they play in midlatitude, moist cyclogenesis.

In an effort to identify the important physical processes at work in a moist, baroclinic atmosphere, a 2D, SG model with the EFT parameterization of latent heat release was used to diagnose the moist, exponentially growing modes of the Eady basic state. In this model setting, the vertical profile of latent heat release is largely controlled by the moisture parameter (R), essentially a measure of the deviation from moist neutrality along a constant absolute momentum surface. When R is allowed to vary in accordance with the expected temperature dependence of latent heat release, the result is a linearly increasing function of height. In comparison with the small but constant R case, this more realistic approach results in: i) decreased growth rates, ii) a shift to longer scales of the most unstable mode, iii) the absence of a shortwave cutoff, iv) constant growth rates for zonal wavelengths less than approximately 1900 km, and v) a more precipitous decrease of phase speed with decreasing characteristic zonal scale.

Consistent with the idea of a separation of scale of observed disturbances in the middle and high latitudes [e.g. long waves and cyclone waves (Eady 1949)], two growth regimes are identified. Similar to both the dry and small but constant R systems, waves longer than 1900 km grow due to the mutual interaction of surface and tropopause PT anomalies. In contrast, for waves shorter than 1900 km, no upper boundary disturbance

is necessary for growth. Instead, it is the constant production of diabatically-generated PV (through the process of warm air advection, rising motion and latent heat release) that allows for amplification. This disturbance structure and evolution has been identified as a diabatic Rossby wave; however, due to the vortical nature of these features, we suggest that a more appropriate name is a diabatic Rossby vortex (DRV).

Even in the presence of 'realistic' surface friction, exponential growth is predicted over a large range of zonal wavelengths in the small but finite amplitude regime. As the vortex grows with time and surface wind speeds increase, quadratic surface drag becomes more effective at reducing growth. However, the results indicate that surface friction does not eliminate exponential instability in the modified, moist system (over an ocean surface) and that, once generated, small-scale modes can persist and slowly intensify.

The fact that diabatic Rossby vortices have been identified in simplified, balanced systems incorporating a variety of latent heat parameterization schemes and observations suggest that they should be a robust feature of the moist, baroclinic atmosphere. However, to ascertain the characteristics of a 'true' DRV, a more complete model setting is needed. In this light, we used the PSU/NCAR mesoscale model (MM5) to conduct a number of idealized simulations to investigate the formation, growth and evolution of DRVs.

A primary goal of this portion of the study was to confirm the simplified model results that an alternative growth mechanism to that of traditional baroclinic instability theory exists in a moist, baroclinic atmosphere. The disturbance structure that emerges in this model setting agrees very well with the 2D results. Furthermore, it is clear that use of the term 'vortex' is more appropriate than 'wave': in addition to the absence of the alternating high / low structure that is associated with wave-like disturbances, a closed circulation is evident at low-levels.

An equally important objective of the MM5 analysis was to determine and quantify the important factors that affect DRV characteristics. The sensitivity study here demonstrates that DRV formation necessitates the presence of sufficient environmental baroclinicity and moisture. Without either one of these components, convection cannot occur and the DRV growth mechanism, which owes its existence to the diabatic generation of PV, cannot operate. Once formed, the ensuing intensity of a DRV (as measured by the instantaneous growth rate) is intimately tied to these two parameters: increased environmental baroclinicity and / or increased moisture content results in a more intense disturbance.

The 3D structure of moisture is found to be the most important factor in determining the structure of a DRV. The vertical profile of diabatic heating and the level at which PV generation occurs is largely controlled by the vertical profile of moisture. Broadly speaking, the level at which maximum diabatic heating occurs is higher for a deep moist layer than for a shallow moist layer. In this manner, the depth of the moist layer defines the characteristic depth of the DRV. An examination of the sensitivity of DRV dynamics to the depth of a DRV illustrates the important repercussions of a change in this parameter. In accord with the earlier 2D result, a deep DRV grows faster and translates more quickly than a shallow DRV.

While not the dominant factor in defining the characteristic depth of a DRV, knowledge of the 'size' and 'strength' of an initial perturbation vortex is also important from a predictability standpoint. The translation speed and the intensity (as measured by the minimum sea level pressure) of the DRV at any future time are sensitive to these parameters.

5.2 Discussion and Future Work

The main goal of this work was to conduct an in-depth examination into the dynamics and characteristics of the short-scale, diabatic disturbances that emerge in a moist, baroclinic atmosphere. In this light, we have limited the discussion to the basic physical mechanisms at work. However, at this time, we would be remiss if we did not take a step back and look at the larger issues at hand. Two such issues are that of predictability and the applicability of the DRV growth mechanism to varied atmospheric processes.

5.2.1 Predictability

Our findings here illustrate the challenges that DRV formation and evolution pose to the operational forecast community. It is clear that an accurate picture of both the background environment and the perturbation field is integral for an accurate forecast. An erroneous representation of the initial condition field will likely contribute to a poor forecast of DRV evolution or, at worst, lead to the failure of simulating DRV formation entirely. This inherent problem is exacerbated by the remoteness of the preferred regions of DRV genesis: due to their reliance on environmental moisture, DRVs often form and grow over the ocean in regions where there is a distinct lack of observational data.

While the present work has been primarily concerned with the basic physical mechanisms responsible for DRV formation, growth and evolution, the results may lend significant insight into other important areas of meteorological research. A main goal of adaptive observations and singular vector techniques is to ascertain the information content necessary for an accurate forecast. It is likely that disturbances that owe their existence to the DRV growth mechanism will be identified in these types of studies. As a case in point, in their study of the influence of physical processes on extratropical

singular vectors, Coutinho et al. (2004) note that not all singular vectors are the same for both dry and moist model simulations (Fig. 5.1). When moist physics are included, some singular vectors occur in new locations and have particularly confined structures. They state one such singular vector 'clearly depends strongly on the availability of moisture' (Coutinho et al. 2004; see Fig. 5.1c). While a more detailed examination would be necessary to positively associate this feature with DRV dynamics, the result is intriguing.

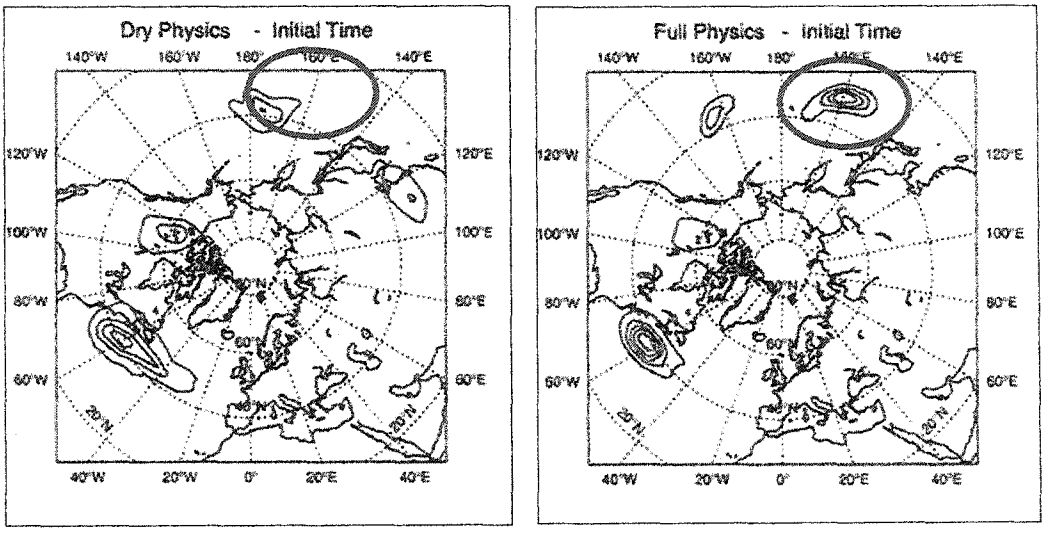

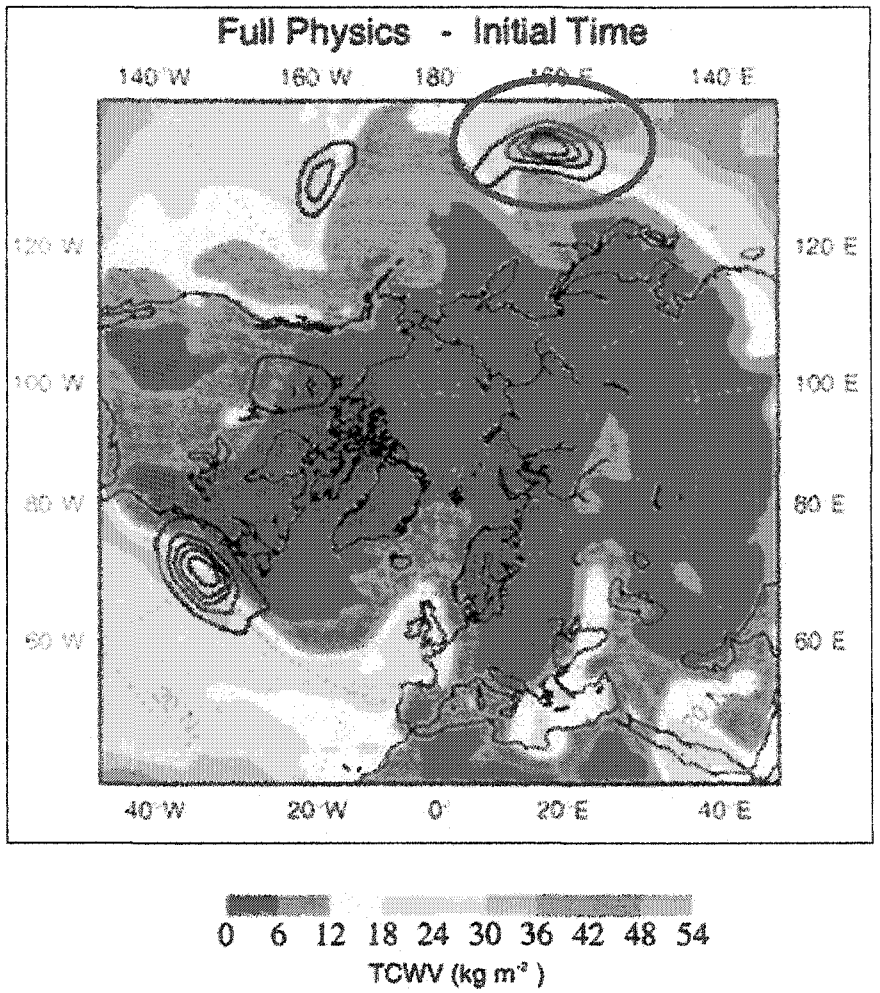

Figure 5.1 – Figs. 4a, 4b and 7, respectively, from Coutinho et al. (2004). Red circle indicates the location of moist, singular vector.

5.2.2 The Possible Role of DRVs in Atmospheric Processes

In the simplest sense, a DRV is a disturbance that owes its existence to the diabatic production of PV. The sole environmental ingredients necessary for DRV formation and growth are sufficient moisture and baroclinicity. As a result, this type of disturbance can and has been related to a myriad of atmospheric processes [explosive cyclones (Gyakum et al. 1992; Wernli et al. 2002), mesoscale convective systems

(Raymond and Jiang 1990), squall lines (Parker and Thorpe 1995), and polar lows (Montgomery and Farrell 1992; Fantini and Buzzi 1993; Mak 1994)]. This fact notwithstanding, there remains a paucity of research into the precise role the DRV growth mechanism plays.

The case of extreme winter storm 'Lothar' provides an excellent example of the role a DRV can play in explosive cyclogenesis (Wernli et al. 2002). Studies have shown that substantial development is often observed before the period of most rapid deepening (Bosart 1981; Gyakum 1983 and 1991; Uccellini 1986), describing a two-stage process of explosive cyclone development (Gyakum et al. 1992). While the latter phase of rapid intensification is typically characterized by a nonlinear interaction between upper- and lower-level cyclonic disturbances, the antecedent phase often involves a surface cyclone that has formed independently from the upper level disturbance in regions of preexisting surface frontogenesis and heavy precipitation (Gyakum et al. 1992). The precursor disturbance of 'Lothar', identified by Wernli et al. as a diabatic Rossby wave, clearly played the role of a low-level, coherent vortex in the antecedent phase of the storm.

Another intriguing possibility is a connection with the extratropical transition of a tropical cyclone. This process is often characterized by an initial weakening of the tropical cyclone followed by a subsequent intensification (e.g. Hart and Evans 2001). We believe the model set-up used in this study provides a useful template for studying extratropical transition. The structure of an initial perturbation vortex with a strong low-level cyclonic circulation, a large warm anomaly and high moisture content is at least qualitatively reminiscent of a transitioning tropical cyclone. The idealized MM5 simulations presented here illustrate how such a perturbation vortex can initially survive and subsequently grow in a moist, baroclinic atmosphere. We hypothesize that it is the DRV growth mechanism that allows for the decaying tropical cyclone to translate from a tropical to a baroclinic environment, where significant re-intensification can occur.

Another possible link between the DRV growth mechanism and tropical processes may be found in the amplification of easterly waves. The main formation mechanism for easterly waves is barotropic instability, however, these disturbances do exist in an environment of ambient baroclinicity and vertical wind shear. While the sign of the temperature gradient and vertical wind shear is reversed in this case, it is entirely plausible that the growth mechanism outlined in this study may play a role in the amplification and westerly propagation of these disturbances.

Furthermore, it should be stated that the importance of the DRV growth mechanism is not limited to oceanic phenomenon. As Raymond and Jiang (1990) illustrated, this growth mechanism likely plays a role in the growth and maintenance of mesoscale convective systems. These systems often occur over the great plains of the United States in conjunction with background baroclinicity and large amounts of moisture whose source is the Gulf of Mexico. Therefore, it can be hypothesized that is the DRV growth mechanism that is, in part, responsible for the longevity of these systems. The recently completed BAMEX field project provides an excellent observational dataset that, in combination with numerical simulations, may provide significant insight into this problem.

In summary, the results of this work build a useful framework for further study. The knowledge gained from this analysis of DRV formation, growth and evolution provides a convenient starting point for studying the varied atmospheric phenomenon involving the DRV growth mechanism.

6. References

Bond, N. A. and R. G. Fleagle, 1985: Structure of a cold front over the ocean. *Quart. J. Roy. Meteor. Soc.*, **111**, 739-759.

Bosart, L. F., 1981: The Presidents' Day snowstorm of 18-19 February 1979: a subsynoptic-scale event. *Mon. Wea. Rev.*, **109**, 1542-1566.

Coutinho, M. M., B. J. Hoskins and R. Buizza, 2004: The influence of physical processes on extratropical singular vectors. *J. Atmos. Sci.*, **61**, 195-209.

Craig, G. C. and H. R. Cho, 1988: Cumulus heating and CISK in the extratropical atmosphere, part I. Polar lows and comma clouds. *J. Atmos. Sci.*, **45**, 2622-2640.

Davis, C. A., D. G. E. D. Grell and M. A. Shapiro, 1996 : The balanced dynamical nature of a rapidly intensifying oceanic cyclone. *Mon. Wea. Rev.*, **45**, 3-26.

Dickinson, M. J., L. F. Bosart, W. Bracken, G. J. Hakim, D. M. Schultz, M. A. Bedrick and K. R. Tyle, 1997: The march 1993 superstorm cyclogenesis: incipient phase synoptic- and convective-scale flow interaction and model performance. *Mon. Wea. Rev.*, **124**, 3041-3072.

Durran, D. R., 1999: Numerical methods for wave equations in geophysical fluid dynamics. Springer-Verlag, 465 pp.

Eady, E. T., 1949: Long waves and cyclone waves. *Tellus*, **1**, 33-52.

Emanuel, K. A., 1985: Frontal circulations in the presence of small moist symmetric stability. *J. Atmos. Sci.*, **42**, 1062-1971.

-----, 1988: Observational evidence of slantwise convective adjustment. *Mon. Wea. Rev.*, 116, 1805-1816.

-----, M. Fantini and A. J. Thorpe, 1987: Baroclinic instability in an environment of small stability to slantwise moist convection. part 1: two-dimensional models. *J. Atmos. Sci.*, **44**, 1559-1573.

-----, and R. Rotunno, 1989: Polar lows as Arctic hurricanes. *Tellus*, **41A**, 1-17.

Fantini, M., 1993: A numerical study of two-dimensional moist baroclinic instability. *J. Atmos. Sci.*, **50**, 1199-1210.

-----, 1995: Moist eady waves in quasigeostrophic three-dimensional model. *J. Atmos. Sci.*, **52**, 2473-2485.

-----, and A. Buzzi, 1993: Numerical experiments on a possible mechanism of cyclogenesis in the Antarctic region. *Tellus*, **45A**, 99-113.

-----, and A. Buzzi, 1994: Short baroclinic waves of small amplitude in a moist environment. *Quart. J. Roy. Meteor. Soc.*, **120**, 1069-1084.

-----, and A. Buzzi, 1997: Baroclinic waves in a shallow saturated layer. *J. Atmos. Sci.*, **54**, 2146-2154.

Farrell, B., 1984: Modal and nonmodal baroclinic waves. *J. Atmos. Sci.*, **41**, 668-673.

-----, 1985: Transient growth on damped baroclinic waves. *J. Atmos. Sci.*, **42**, 2718-2727.

-----, 1989: Unstable baroclinic modes damped by Ekman dissipation. *J. Atmos. Sci.*, **46**, 397-401.

Fleagle, R. G. and W. A. Nuss, 1985: Distribution of surface fluxes and boundary layer divergence in midlatitude ocean storms. *J. Atmos. Sci.*, **42**, 784-799.

Flierl, G. R., M. E. Stern and J. A. Whitehead, Jr., 1983: The application of linear quasi-geostrophic dynamics to Gulf Stream rings. *J. Phys. Oceanogr.*, **7**, 365-379.

Gill, A. E., 1982: *Atmosphere-Ocean Dynamics*. Academic Press, 662 pp.

Gradshtein, I. S., and I. M. Rzyhik, 1980: Tables of integrals, series, and products. Academic Press, 1160 pp.

Grell, G. A., J. Dudhia and D. R. Stauffer, 1994: A description of the fifth-generation Penn State/NCAR mesoscale model (MM5). *NCAR Technical Note*, NCAR/TN-398+STR, 117 pp.

Gyakum, J. R., 1983: Meteorological precursors to the explosive intensification of the QE II storm. *Mon. Wea. Rev.*, **119**, 1105-1131.

-----, 1991: On the evolution of the QE II storm. I: synoptic aspects. *Mon. Wea. Rev.*, **111**, 1137-1155.

-----, P. J. Roebber and T. A. Bullock, 1992: The role of antecedent surface vorticity development as a conditioning process in explosive cyclone intensification. *Mon. Wea. Rev.*, **120**, 1465-1489.

Hack, J. J. and W. H. Schubert, 1986: Nonlinear response of atmospheric vortices to heating by organized cumulus convection. *J. Atmos. Sci.*, **43**, 1559-1573.

Hart, R. E. and J. L. Evans, 2001: A climatology of the extratropical transition of atlantic tropical cyclones. *J. Climate*, **14**, 546-564.

Hong, S. Y. and H. L. Pan, 1996: Nonlocal boundary layer vertical diffusion in a medium-range forecast model. *Mon. Wea. Rev.*, **124**, 2322-2339.

Hoskins, B. J. and F. P. Bretherton, 1972: Atmospheric frontogenesis models: mathematical formulation and solution. *J. Atmos. Sci.*, **29**, 11-37.

Joly, A. and A. J. Thorpe, 1989: Warm and occluded fronts in two-dimensional moist baroclinic instability. *Quart. J. Roy. Meteor. Soc.*, **115**, 513-534.

Jones, S. C., P. A. Haar, J. Abraham, L. F. Bosart, P. J. Bowyer, J. L. Evans, D. E. Hanley, B. N. Hanstrum, R. E. Hart, F. Lalaurette, M. R. Sinclair, R. K. Smith and C. Thorncroft, 2003: The extratropical transition of tropical cyclones: forecast challenges, current understanding, and future directions. *Wea. Forecasting.*, **18**, 1052-1092.

Kain, J. S., 2004: The Kain-Fritsch convective parameterization: an update. *J. Appl. Meteor.*., **43**, 170-181.

Large, W. G. and S. Pond, 1982: Sensible and latent heat flux measurements over the ocean. *J. Phys. Oceanogr.*, **118**, 3-25.

Lin, S. and R. T. Pierrehumbert, 1988: Does Ekman friction suppress baroclinic instability?. *J. Atmos. Sci.*, **45**, 2920-2933.

Liou, C. and R. L. Elsberry, 1987: Heat budgets of analyses and forecasts of an explosively deepening maritime cyclone. *Mon. Wea. Rev.*, **115**, 1809-1824.

Lorenz, E. N., 1995: Available potential energy and the maintenance of the general circulation. *Tellus*, 7, 157-167.

Mak, M., 1994: Cyclogenesis in a conditionally unstable moist baroclinic atmosphere. *Tellus*, **46A**, 14-33.

McWilliams, J. C. and G. R. Flierl, 1979: On the evolution of isolated, nonlinear vortices. *J. Phys. Ocean*, **9**, 1155-1182.

-----, 1998: Influence of surface sensible heat flux on incipient marine cyclogenesis. *J. Atmos. Sci.*, **55**, 820-834.

McWilliams, J. C., 1984: The emergence of isolated coherent vortices in turbulent flow. *J. Fluid Mech.*, **146**, 21-43.

Moore, R. W. and M. T. Montgomery, 2004: Reexamining the dynamics of short-scale, diabatic Rossby waves and their role in midlatitude moist cyclogenesis, *J. Atmos. Sci.*, **61**, 754-768.

Montgomery, M. T. and B. F. Farrell, 1991: Moist surface frontogenesis associated with interior potential vorticity anomalies in a semigeostrophic model. *J. Atmos. Sci.*, **48**, 343-367

-----, and B. F. Farrell, 1992: Polar low dynamics. *J. Atmos. Sci.*, **49**, 2484-2505.

-----, and B. F. Farrell, 1993: Tropical cyclone formation. *J. Atmos. Sci.*, **50**, 285-310.

Muench, H. S., 1965: On the dynamics of the wintertime stratosphere circulation. *J. Atmos. Sci.*, **22**, 349-360.

Norquist, D. C., E. E. Recker and R. J. Reed, 1977: The energetics of African wave disturbances as observed during phase III of GATE. *Mon. Wea. Rev.*, **105**, 334-342.

Ooyama, K., 1969: Numerical simulation of the life cycle of tropical cyclones. *J. Atmos. Sci.*, **26**, 3-40.

Parker, D. J. and A. J. Thorpe, 1995: Conditional convective heating in a baroclinic atmosphere: a model of convective frontogenesis. *Quart. J. Roy. Meteor. Soc.*, **52**, 1699-1711.

Press, W. H., B. P. Flannery, S. A. Teukolsky and W. T. Vetterling, 1986: *Numerical Recipes, The Art of Scientific Computing*, Cambridge University Press, 818 pp.

Raymond, D. J. and H. Jiang, 1990: A theory for long-lived mesoscale convective systems. *J. Atmos. Sci.*, **47**, 3067-3077.

Reed, R. J., A. J. Simmons, M. D. Albright and P Unden, 1988: The role of latent heat release in explosive cyclogenesis: three examples based on ECMWF operational Forecasts. *Wea. Forecasting.*, **3**,217-229.

-----, G. A. Grell, and Y. H. Kuo, 1993: The ERICA IOP 5 storm. Part II: Sensitivity tests and further diagnosis based on model output. *Mon. Wea. Rev.*, **121**, 1595-1612.

Rotunno, R. and Emanuel, K. A., 1987: An air-sea interaction theory for tropical cyclones. Part II: evolutionary study using a nonhydrostatic axisymetric numerical model. *J. Atmos. Sci.*, **44**, 542-561.

-----, and J. Bao, 1996: A case study of cyclogenesis using a model hierarchy. *Mon. Wea. Rev.*, **101**,12495-12514.

Shapiro, L. J. and K. V. Ooyama, 1990: Barotropic vortex evolution on a beta plane. *J. Atmos. Sci.*, **47**, 170-187.

Snyder, C. and R. S. Lindzen, 1991: Quasi-geostrophic wave-CISK in an unbounded baroclinic shear. *J. Atmos. Sci.*, **48**, 76-86.

Thorpe, A. J. and K. A Emanuel, 1985: Frontogenesis in the presence of small stability to slantwise convection. *J. Atmos. Sci.*, **42**, 1809-1824.

Uccellini, L. W., 1986: The possible influence of upstream upper-level baroclinic processes on the development of the QE II storm. *Mon. Wea. Rev.*, **114**, 1019-1027.

Ulbrich, U., A. H. Fink, M. Klawa and J. G. Pinto, 2001: Three extreme storms over europe in December 1999. *Weather*, **56**, 70-80.

Valdes, P. J. and B. J. Hoskins, 1988: Baroclinic instability of the zonally averaged flow with boundary layer damping. *J. Atmos. Sci.*, **45**, 1584-1593.

Wakimoto, R. M. and H. Cai, 2002: Airborne observations of a front near a col during FASTEX. *Mon. Wea. Rev.*, **130**, 1898-1912.

Wernli, H., S. Dirren, M. A. Liniger and M. Zillig, 2002 : Dynamical aspects of the life cycle of the winter storm 'Lothar' (24-26 december 1999). *Quart. J. Roy. Meteor. Soc.*, **128**, 405-429.

Whitaker, J. S. and C. A. Davis, 1994: Cyclogenesis in a saturated environment. *J. Atmos. Sci.*, **51**, 889-907.

Zhang, F., C. Snyder and R. Rotunno, 2002: Mesoscale predictability of the 'surprise' snowstorm of 24-25 january 2000. *Mon. Wea. Rev.*, **130**, 1617-1632.

Zupanski, M., D. Zupanski, D. F. Parrish, E. Rogers and G. DiMego, 2002: Four-dimensional variational data assimilation for the blizzard of 2000. *Mon. Wea. Rev.*, **130**, 1967-1988.